Synchronization and Signal Enhancement in Nonlinear and Stochastic Systems

A Thesis
Presented to
The Academic Faculty

by

Matthew R. Bennett

In Partial Fulfillment
of the Requirements for the Degree
Doctor of Philosophy in the
School of Physics

Georgia Institute of Technology
May 2006

Synchronization and Signal Enhancement in Nonlinear and Stochastic Systems

Approved by:

Dr. Kurt Wiesenfeld, Advisor
School of Physics
Georgia Institute of Technology

Dr. Ron Fox
School of Physics
Georgia Institute of Technology

Dr. Turgay Uzer
School of Physics
Georgia Institute of Technology

Dr. Michael Schatz
School of Physics
Georgia Institute of Technology

Dr. John Lindner
Department of Physics
The College of Wooster

February 9, 2006

I would like to dedicate this dissertation to my family and friends who stuck with me all these years and especially to my wife – without whom my life would be so much more lonely.

ACKNOWLEDGMENTS

There are many people I wish to thank who have helped me over the years. Foremost among them is my advisor, Kurt Wiesenfeld, whose subtle, light-handed style has taught me much more than I realized at the time. I would also like to thank Mike Schatz, who showed me (much to my chagrin) that physics is more than equations. John Lindner was a joy to work with – his numerical grace never ceases to boggle my mind. Stephen Lewis and Kevin Fortier have been invaluable friends to me during my tenure at Georgia Tech, and they were always more than willing to point out that I was not always right. Thanks to Andreas Handel, Denis Tsygankov, Rytis Paskauskas and Yueheng Lan, who helped me (and each other) get through the first few years of "Predrag's vision". Matt Wolf of the Interactive High Performance Computing Lab at Georgia Tech was of immeasurable help with all things parallel. Velera Pate and everyone in the finance office at the School of Physics helped to keep my money situation in order, even when I failed to. I would also like to thank the faculty of the School of Physics at Georgia Tech for being wonderful teachers, and especially Ron Fox, Andy Zangwill and Ray Flannery, who are among the best lecturers I know. Finally, I wish to acknowledge Mafori Moore, who was my mentor while I was still trying to find my way. She encouraged me to look beyond what was taught in the classroom and discover for myself the wonders of mathematics hidden from the casual observer.

TABLE OF CONTENTS

LIST OF FIGURES

SUMMARY

The first part of this dissertation is devoted to synchronization in distributed Josephson junction arrays. Josephson junction arrays have long been the theoretical archetype for uniformly, globally coupled oscillators. However, as experiments push arrays to higher frequencies the old model of Josephson junction arrays no longer captures the dynamics of real arrays. We explore the dynamics of a newer model that is valid even in the high frequency limit. In the second part we explore a variation of stochastic resonance. Typically, stochastic resonance is modelled using a single source of idealized white noise. We examine what happens when multiple sources of noise are present with multiple correlation times. We find that if one noise source is white and the other colored then stochastic resonance may or may not occur as a function of the correlated noise strength. If the correlation time is small, then stochastic resonance still occurs. However, if the correlation time becomes too large then stochastic resonance disappears altogether.

CHAPTER 1

INTRODUCTION

Coherence is an astonishing phenomenon. To illustrate this statement, let's take a simple example: a crowd of people clapping in time with music. At first glance this example might seem trivial. One might think: "of course people can clap together, how hard can that be?" Well, let's think carefully about what it takes for a crowd to behave in such a synchronous manner.

First, each individual must be able to clap rhythmically. Luckily, we, as humans, can force our bodies to oscillate at a (mostly) constant frequency. Most people do this involuntarily when they clap, walk, run, or tap their fingers impatiently. For some reason our bodies tend to do some things rhythmically. In one sense this is not surprising, since our bodies execute many truly involuntary functions periodically (such as breathing and beating of the heart). Though scientists have studied *how* humans perform oscillatory feats, we are more concerned here that they *can* perform them. In other words, humans are oscillators.

Another necessary component of rhythmic clapping is the ability to hear. It is one thing to be able to clap, but it is another to know when to do it. Hearing allows us to understand what is going on around us. That sensory input, in turn, tells us when, and how fast, we should clap. Not every oscillator has the ability to obtain information about the other oscillators around it. For instance, a piano player might set his tempo based on the clicks and clacks of a metronome, but no one would say that the metronome is clicking and clacking based on the music of the pianist. This is called driving – the metronome is driving the pianist, but not the other way around. Likewise, when a crowd claps in time with music, it is the music that is driving the crowd.

Finally, it is important that humans can adapt to the changing environment. If, for instance, one finds that he is clapping too slowly, he can easily change his tempo to fit the music. Or, if in the absence of music, the tempo of a group starts to change, individuals

can change with it, anticipating when the next clap should come. This ability also allows us to ignore people who are clapping incorrectly, since we are more inclined to follow what we perceive as the correct tempo set by the music. Adaptability is not trivial. Imagine trying to program a computer to "clap" in time with humans. It is easy to make the computer clap at a constant rhythm, but it is another thing altogether to get the computer to change its tempo based upon what a less precise human does.

Ironically, it is this last ability, the one that makes us the most flexible, that actually makes it hard to get large crowds to clap in unison. We have all been in audiences that start clapping along to music, but never seem to quite get into unison. What causes this? Typically it is due to several factors. If the crowd is large enough, there is generally a noticeable difference between the times when the front of the audience hears the music and when the back of the audience hears it. This causes a difference in the *drive* between the two groups. The front group is being driven before the rear group. As a result, the two groups clap at different times. In the absence of our ability to adjust the frequency of our claps, this would not cause a problem. However, people in one group can hear the other group and sense that something is wrong. The individual clapper must make a choice between following the music that he hears, and trying to synchronize with other members of the audience. The decision usually depends on which urge is stronger, and probably involves psychological factors beyond the scope of this discussion. Nevertheless, a decision is made, and when every person in an audience makes that decision the result rarely leads to perfect synchronization of the clapping.

Certainly there are ways to improve the synchronization capability of large groups. For instance, if each individual had a personal headset on which to listen to the music, everyone would hear the music at the same time. Visual clues could also be given. Because light travels much faster than sound, these visual clues would reach everyone nearly instantaneously. Both of these solutions fix the problem of disparate driving times for different members of the audience. In other words, these tools make each member of the audience more identical to the other members. Generally, the more similarly each clapper hears and reacts to his surroundings, the more synchronization will be possible. This is because the

choice between following the crowd tempo or following the drive tempo is now a choice between nearly identical options.

This simple example illustrates an important point about the synchronization of coupled oscillators. Typically, in the literature, these oscillators are considered uniformly and globally coupled, meaning that each oscillator hears and senses all of the other oscillators and the response of each to those inputs is also the same. Unfortunately, as in the case of the crowd clapping along to music, oscillators are rarely coupled uniformly and globally.

The first part of this dissertation we address the matter of non-uniformly coupled oscillators. By examining high frequency Josephson junction arrays new light will be shed on an old subject. Josephson junction arrays have long been esteemed as the archetype of synchronizing oscillator arrays. Wiesenfeld et al. realized that, in one limit, Josephson junction arrays can be mapped onto a variant of the mathematical model called the Kuramoto oscillator array [61, 62, 86, 103]. This model treats the junctions as identical oscillators, each of which is uniformly coupled into every other oscillator. The synchronization properties of the Kuramoto model were by then well understood, and its extension onto the Josephson junction array problem worked beautifully.

Unfortunately, one assumption by Wiesenfeld et al. breaks down in the high frequency limit. This assumption, known as the Kirchhoff limit, had treated the current through the junctions as uniform throughout the array. At high frequencies, however, the current is no longer uniform, and varies at each junction depending on its position along the array. As real arrays are pushed to ever higher frequencies, it becomes important that we understand the dynamics of Josephson junction arrays operating outside the Kirchhoff limit.

We will show that the consequence of the breakdown of the Kirchhoff limit assumption is a system that can be mapped onto another variant of the Kuramoto model – one in which the coupling scheme is no longer uniform. In other words, each oscillator in the array senses the other oscillators differently. This non-uniformity in the coupling drastically changes the synchronization properties of the array, and we will explore exactly how this works.

The second part of this dissertation will be dedicated to a different type of coherence phenomenon known as stochastic resonance. Instead of trying to synchronize multiple

oscillators, here we try to maximize the coherence of a single system to a periodic drive. To complicate matters the system is in a noisy environment. This situation is analogous to hearing. Imagine trying to listen to a pure tone, perhaps a middle C played on a violin. However, in addition to the violin there is also some noise, perhaps from a radio that has been tuned to an empty band of the radio spectrum. Normally, the louder the radio is the harder it is to hear the violin, and we hear the violin best when the noise from the radio is at the lowest possible volume. Stochastic resonance, by contrast, is the phenomenon by which the violin is actually heard better when the volume of the noise is turned *up* to some finite level. Unfortunately, real radios cannot take advantage of this phenomenon, because their response to incoming radio waves is approximately linear. Stochastic resonance requires a *nonlinear* response of the system to incoming signals.

Stochastic resonance was first proposed as a mechanism to explain the periodicity of the Earth's ice ages [3]. Since that time stochastic resonance has been found in a myriad of systems and is now well understood in a variety of forms. Systems that exhibit stochastic resonance typically contain three necessary elements. First, the system must contain a nonlinearity. The first models of stochastic resonance consisted of systems in which the dynamics are prescribed by a double well potential function, creating the necessary nonlinearity. The two wells of the potential function generally correspond to two different states of the system, with one state corresponding to one value of the output current, and the other state a different value. As the periodic drive forces the system towards one state and then the other, the system may respond by switching to the corresponding well. The drive, which is the second necessary element of stochastic resonance, is the "signal" which the system is trying to detect. In the case of our simple hearing analogy the drive is the middle C played by the violin. The third and final element is the noise. It provides a random forcing term that usually muddies the clear signal of the drive. In systems that exhibit stochastic resonance, though, we shall see that the noise will actually help the system detect the signal.

It is the noise that will be the central focus of our study of stochastic resonance. In most models, the noise is typically assumed to be Gaussian white noise. This type of noise, which is an idealization of what truly occurs in physical systems, has the advantage

that certain analytic methods for analyzing such systems become tractable. Nevertheless, many systems that exhibit stochastic resonance are not well modelled by white noise, and instead may contain noise that is "colored", or perhaps even have multiple sources of noise with differing characteristics. When this is taken into account the analysis of the resulting equations becomes prohibitively difficult. We will examine two theories that might be able to explain stochastic resonance in systems that contain two sources of noise - one that is fast (i.e. white) and one that is slow (i.e. colored).

At first glance these two phenomena - synchronization and stochastic resonance - are very different. In one, synchronization, we have a deterministic system comprised of numerous interacting parts, while in the other, stochastic resonance, the system is non-deterministic and consists of just a single driven sensor. The two are very different, but they share something fascinating. Both are complex systems that exhibit emergent phenomenon. This means that even though each system is, at its core, a complicated and unorganized entity, the behavior of each can be strikingly (and perhaps unexpectedly) rich and uniform. In other words, the *coherence* of both systems is more than what one would expect given their complex nature.

PART I

DISTRIBUTED JOSEPHSON JUNCTION ARRAYS

CHAPTER 2

JOSEPHSON JUNCTION ARRAYS

2.1 The Josephson Effect

In 1962, Brian Josephson made an astonishing discovery [57]. He correctly predicted that when two superconducting electrodes were brought close to each other a supercurrent would arise between them (see Figure 1). This would happen whenever the gap was small enough and filled with some insulating material. Josephson calculated that the supercurrent would have the magnitude

$$I = I_c \sin(\phi), \tag{1}$$

where I_c is the critical current (the maximum current allowed), and ϕ is the phase difference between the quantum wavefunctions in the two electrodes. As current flows from one electrode into the other a voltage arises between them. Josephson also found that when this occurs the induced voltage is simply related to the phase difference by

$$V = \frac{\hbar\dot{\phi}}{2e}, \tag{2}$$

where e is the magnitude of the charge of the electron, V is the voltage between the two electrodes, $\hbar$ is Planck's constant divided by 2π, and the overdot denotes differentiation with respect to time. Equations (1) and (2) and the physical system they describe are now eponymously known as the Josephson equations and the Josephson junction, respectively. A derivation of Equations (1) and (2) will not be given in this text. For a simple, heuristic derivation see Reference [25], and for a more detailed derivation see Reference [20].

It must be noted that Equations (1) and (2) model ideal junctions only. In practice the actual dynamics of a Josephson junction can behave quite differently. This is because a junction has electrical properties beyond that of the pure Josephson effect. For instance,

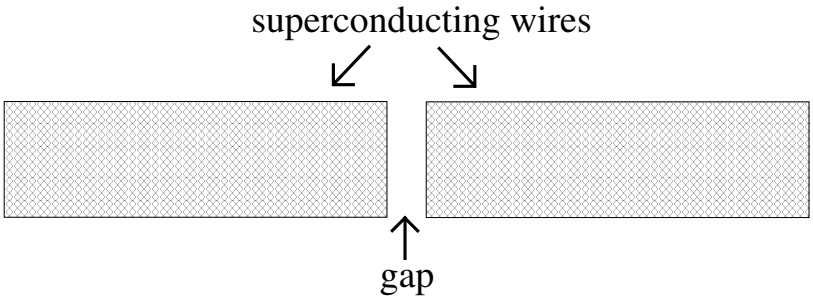

Figure 1: Schematic of a simple Josephson junction. It consists of a superconducting wire with a gap.

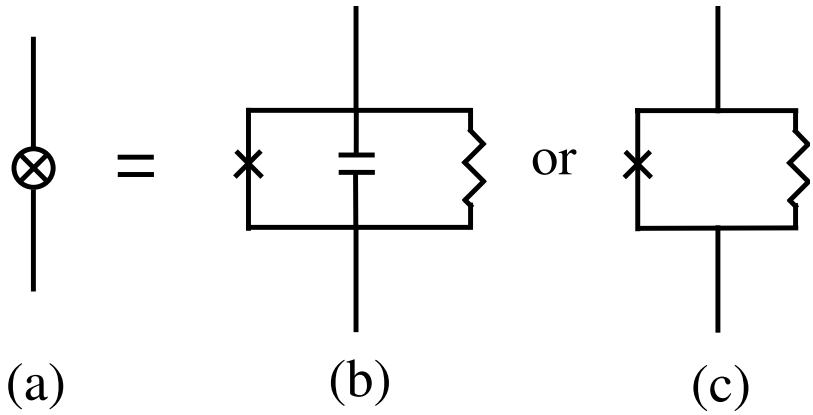

Figure 2: A practical Josephson junction (a) can be modelled either (b) in parallel with both a resistor and a capacitor or (c) with just a resistor. The practical junction is represented by a $\otimes$ while an ideal junction is represented by a $\times$.

the gap can cause significant capacitance in the circuit, and the material inside the gap may not be a pure insulator. These effects are commonly modelled by placing the ideal junction in parallel with a resistor and a capacitor [69], as shown in Figures 2 (a) and (b). The actual values of the resistance and capacitance are determined by the material and geometry of the system.

In practice the capacitance can be made very large, effectively eliminating the need to put a capacitor in the model. The result is the resistively shunted junction (RSJ) model [65], with just the ideal model in parallel with a resistor (see Figure 2 (c)). While other models do exist [17, 65], the RSJ model is of particular interest due to its common use in studies of Josephson junction arrays. These will be discussed later in the text.

The Josephson effect is now known to be quite general, occurring in a variety of systems. The geometry of the system need not be precisely that of Figure 1, and the substantive nature of the gap is not restricted to pure insulators. The only requirement is that two superconducting materials are separated by a thin region of material that is less superconducting. The gap may consist of an insulator, a normal conductive metal, or even be comprised of the same superconductive material as the electrodes, provided its cross sectional area is less than that of the wire [91].

Josephson junctions are now used in a variety of applications. For instance we use them in the present definition of the standard Volt [40]. Josephson junctions have the ability to change DC voltages into AC currents, and we can now measure frequencies with extreme accuracy. From Equation (2) we see that the frequency of oscillation of the junction is given by

$$f = \frac{eV}{\pi\hbar}. \tag{3}$$

The standard Volt is subsequently defined as the voltage needed to drive the junction at a frequency of 483,597.9 GHz.

Josephson junctions are also used to make superconducting quantum interference devices (SQUIDs) [91]. A SQUID is comprised of superconducting material formed into the shape of a circle. Two gaps (Josephson junctions) [1] are then created in the circle directly apart from each other as shown in Figure 3. SQUIDs are extremely sensitive to changes in the magnetic field, and they were used in the discovery and measurement of the magnetic flux quantum

$$\Phi_0 = \frac{\pi\hbar}{e}. \tag{4}$$

[1] We speak here of DC SQUIDs. There also exist single junction (RF) SQUIDs that are used in quantum interference experiments and may be used in quantum computers as memory cells and logic circuits [65].

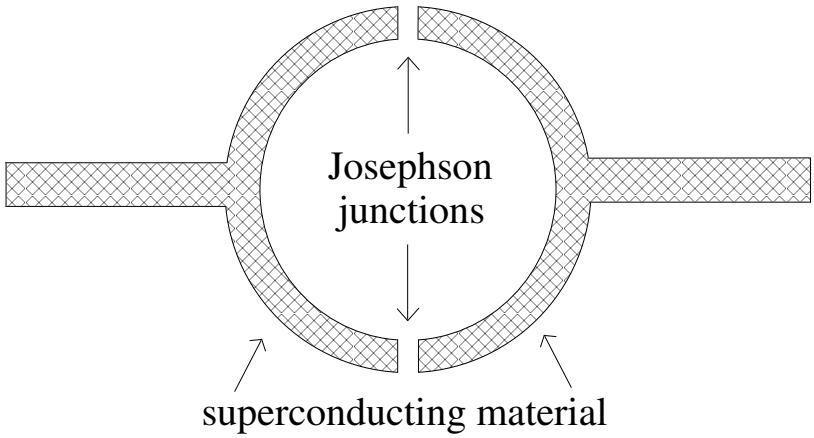

Figure 3: Schematic of a DC SQUID.

2.2 Kirchhoff Limit Josephson Junction Arrays

Soon after the discovery of the Josephson effect, it became clear that Josephson junctions could be used as sources of far infra-red radiation [18]. Unfortunately one junction alone cannot generate enough power to be of much use as a parametric amplifier. To get around this problem one may use many junctions in an array, thereby increasing the power. However, it is necessary to synchronize the junctions so that the emitted radiation is coherent. If the junctions are all at different phases, then so too are the emitted EM waves, which may then cancel each other out. By synchronizing the phases of all of the Josephson junctions in the array, the emitted EM waves all have the same phase, generating larger radiative powers.

As we will soon see, in the Kirchhoff limit each Josephson junction in an array is dynamically independent (uncoupled) from every other junction. In order to synchronize the junctions it becomes necessary to dynamically couple them together in some way. Early studies took advantage of the Josephson junction's reaction to resonant cavity modes set up in the array chamber [18, 90]. Though research into cavity-coupled arrays continues (see, for instance, References [2, 45, 94]), arrays are most commonly coupled by the use of an external load.

In addition to coupling schemes, the geometry of arrays also varies greatly. The array may contain junctions that are simply in series (as in Figure 4) [11, 13, 96] or in more

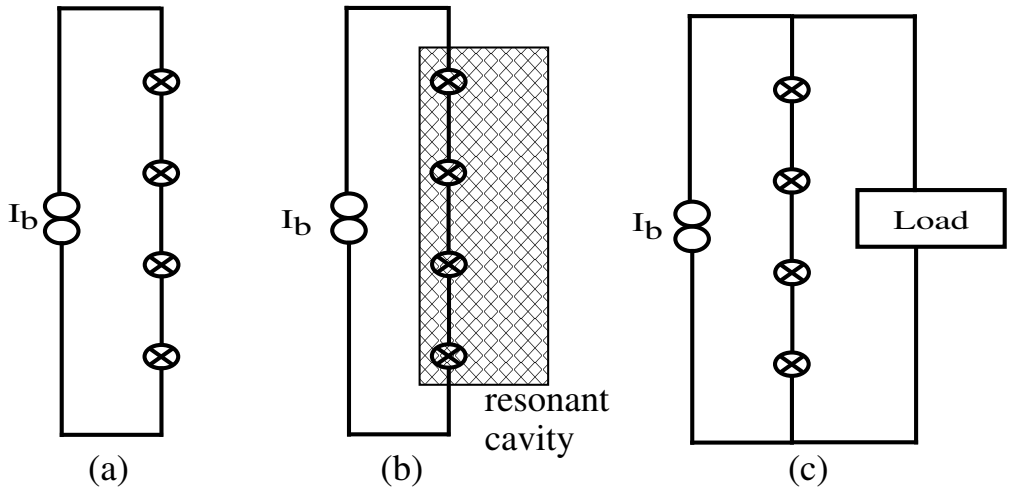

Figure 4: Three types of Josephson junction arrays consisting of four junctions each. Each array is driven by a constant current source, I_b, and can be (a) uncoupled, (b) coupled through a resonant cavity, or (c) coupled through an external load.

complicated arrangements such as two dimensional grids in which the junctions are both in series and parallel [12, 16, 41, 78, 94]. Beginning with work in the late 1980s, series arrays of the type shown in Figure 4(c) became a popular class of systems in nonlinear dynamics, serving as an archetype of spontaneous synchronization in coupled oscillator populations [37, 38, 87, 88].

2.2.1 The Kirchhoff Limit

Circuit analysis typically makes use of two main rules, known as Kirchhoff's laws. The two rules are the node rule[2] and the loop rule, and with their (sometimes repeated) use, the dynamical equations which govern most circuits can be derived. Though they are not always valid, they are a good approximation whenever the length scales of current fluctuations is large compared to the circuit size. This occurs whenever the intrinsic time scales in the circuit are very large (i.e. low frequency).

If we assume that our circuit is operating in the low frequency regime, so that one may use Kirchhoff's laws, then deriving the dynamical equations of linear arrays becomes quite

[2]The node rule is typically called the junction rule. However, we will use the term "node rule" in order to avoid confusion between a circuit junction and a Josephson junction.

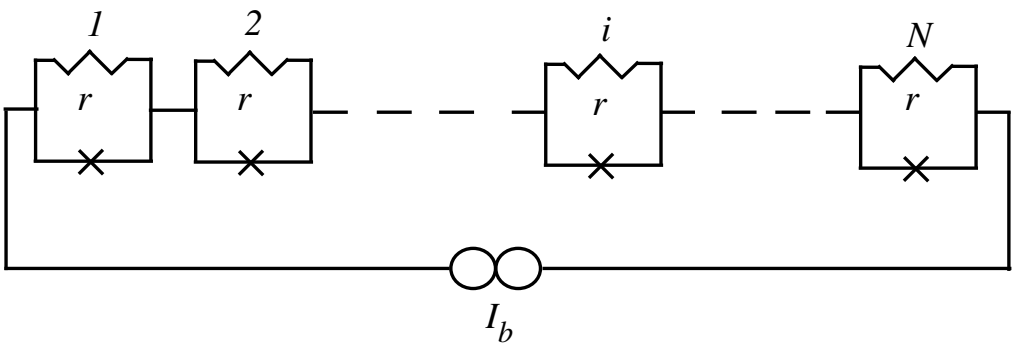

Figure 5: An array of N identical resistively shunted Josephson junctions. They are driven by a constant current source, I_b, and have identical resistances, r.

simple. As a first example consider a linear array of N identical junctions in series (Figure 4(a)) and driven by a constant current source. To perform the circuit analysis we replace each practical junction with a resistively shunted junction model. This gives us the array shown in Figure 5.

Looking at the i^{th} junction and using both of Kirchhoff's laws gives us complete knowledge of the system. First, using the node rule on either of the two nodes at the i^{th} junction tells us that

$$I_b = I_{J,i} + I_{r,i}, \tag{5}$$

where I_b is the bias current, $I_{J,i}$ is the current through the i^{th} ideal Josephson junction, and $I_{r,i}$ is the current through the i^{th} resistor. Using the first Josephson relation (Equation (1)) and Ohm's law turns Equation (5) into

$$I_b = I_c \sin(\phi_i) + \frac{V_{r,i}}{r}, \tag{6}$$

where I_c is the (identical) critical current of the junctions, ϕ_i is the phase difference across the i^{th} Josephson junction, $V_{r,i}$ is the voltage across the i^{th} resistor, and r is the (identical) shunt resistance across each junction.

Next, using Kirchhoff's loop rule on the i^{th} loop tells us that

$$V_{J,i} = V_{r,i}, \tag{7}$$

where $V_{J,i}$ is the voltage across the i^{th} ideal junction. Now, using the second Josephson

relation (Equation (2)) tells us that

$$V_{r,i} = \frac{\hbar \dot{\phi}_i}{2e}. \tag{8}$$

Finally, substituting Equation (8) into Equation (6), and doing some rearranging yields the equation

$$\frac{\hbar}{2er}\dot{\phi}_i + I_c \sin(\phi_i) = I_b. \tag{9}$$

Equation (9) gives a complete dynamical description of the i^{th} junction. Notice that the dynamics of the i^{th} junction are completely independent of the other junctions.

The dynamical independence of junctions in unloaded linear arrays has a profound consequence. It means that even though the junctions are in the same circuit and being driven by the same bias current, they will not be affected by one another. One array of N junctions is then (mathematically) equivalent to N circuits of one junction each. In this case there is no hope that the junctions will synchronize when, and if, they oscillate.

Before we move on, one more point should be made about Equation (9), pertaining to the types of solutions one should expect. In this discussion we will be concerned primarily with the oscillatory nature of the solutions. Notice, though, that stationary solutions can also occur. From Equation (9) we see that the stationary solutions

$$\phi_a = \sin^{-1}\left(\frac{I_b}{I_c}\right) \tag{10}$$

and

$$\phi_b = \pi - \sin^{-1}\left(\frac{I_b}{I_c}\right) \tag{11}$$

exist provided $I_b < I_c$. Both solutions exist for $|I_b| \leq I_c$, and the first solution, ϕ_a, is stable while the other, ϕ_b, is unstable. The stationary solutions disappear when $|I_b| > I_c$, however, and stable periodic solutions then arise. Whenever we discuss periodic solutions we will assume that they are present.

The analysis for an array that contains a load is nearly identical to the analysis of the unloaded array. An array with a general RLC load is shown in Figure 6. The major analytic difference between the loaded and unloaded arrays is the value of the current that flows through the junctions. In the unloaded case, the junction and its associated resistor split a

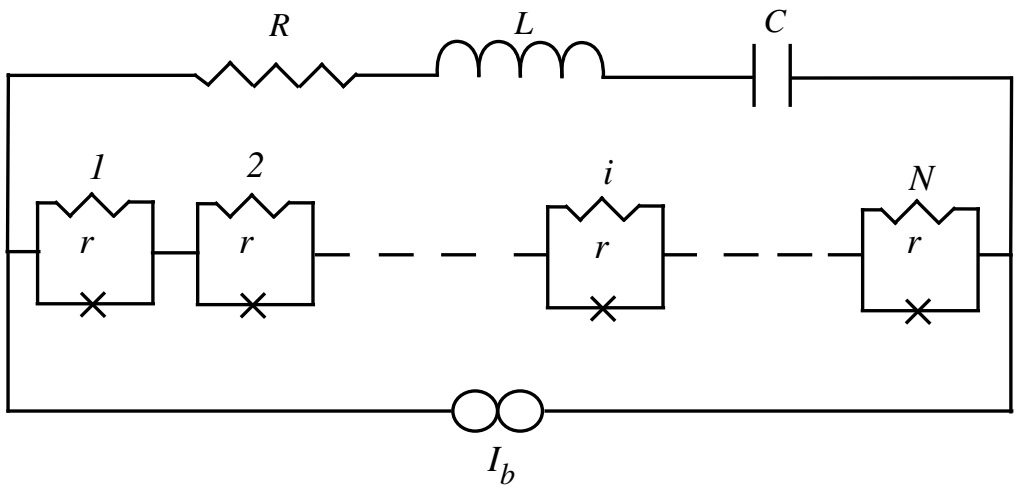

Figure 6: A loaded array of N identical resistively shunted Josephson junctions. They are driven by a constant current source, I_b, and have identical resistances, r. The load has a resistance R, inductance L, and capacitance C.

total current of I_b, due to the bias current. In the loaded case, some of that bias current is redirected through the load, so that the current passing through the junction-resistor loop, I_J, is now less than I_b. The node rule tells us that

$$I_b = I_J + I_L, \tag{12}$$

where I_L is the current passing through the load. Knowing this, we can simply replace the term I_b in Equation (9) with $I_J = I_b - I_L$ to arrive at the differential equation

$$\frac{\hbar}{2er}\dot{\phi}_i + I_c \sin(\phi_i) = I_b - I_L. \tag{13}$$

At first glance Equation (13) also appears to describe uncoupled behavior between the elements in the array, just as in Equation (9). However, notice that we have the extra term I_L on the right hand side. This term, describing the current through the load impedance will evolve with time. We are therefore missing an equation describing $I_L(t)$.

We can derive this equation if we use the loop rule one more time. This time we look at the simple loop containing the load and each of the ideal junctions, giving us

$$L\dot{I}_L + RI_L + \frac{Q}{C} = \frac{\hbar}{2e}\sum_{k=1}^{N}\dot{\phi}_k, \tag{14}$$

where R, L, and C are the load resistance, inductance, and capacitance, respectively, and Q is the charge on the load capacitor.

The left hand side of Equation (14) represents the voltage drop across each of the three load elements, while the right hand side represents the total voltage drop across all of the junctions. Taking the time derivative of Equation (14) and realizing $I_L = \dot{Q}$ leads us to

$$L\ddot{I}_L + R\dot{I}_L + \frac{1}{C}I_L = \frac{\hbar}{2e}\sum_{k=1}^{N}\ddot{\phi}_k. \tag{15}$$

Equations (13) and (15) now provide a complete description of the loaded array problem. Notice that each junction is now dynamically coupled to every other junction. This is because the right hand side of Equation (13) depends on I_L, which in turn depends on all N junctions, as seen in Equation (15).

2.2.2 Synchronization of Kirchoff Limit JJ Arrays

The system of equations that govern loaded Josephson junction arrays represents an exact model in the Kirchoff limit, and fully symmetric (synchronized) solutions exist. However, analysis of such synchronized states quickly becomes unmanageable because even approximate solutions are difficult to find. This difficulty was overcome by Wiesenfeld and Swift [103] who used an averaging technique introduced by Swift et al. [89] to map the $N + 2$ dimensional system (where N is the number of junctions)

$$\frac{\hbar}{2er}\dot{\phi}_i + I_c\sin(\phi_i) = I_b - \dot{Q} \tag{16}$$

$$L\ddot{Q} + R\dot{Q} + \frac{1}{C}Q = \frac{\hbar}{2e}\sum_{k=1}^{N}\dot{\phi}_k \tag{17}$$

onto the N dimensional system

$$\dot{\psi}_k = 1 + \frac{\kappa}{N}\sum_{j=1}^{N}\cos(\psi_j - \psi_k - \delta), \tag{18}$$

where κ and δ are constants comprised of the system parameters and the ψ_k are transformations of the phase angles ϕ_k into a "natural" coordinate system. This natural coordinate system represents one in which the rotation of the phase angles, in the uncoupled limit, are constant in time. Experimentally, I_b is the most directly accessible control parameter. It controls the oscillator frequencies: the larger I_b the higher the frequency.

The loss of two dimensions, corresponding to the two degrees of freedom for the load, is due to the averaging technique, which treats the coupling between the junctions and the load as small. We will not go into the technique in this section, since a detailed derivation, modified for the distributed problem, will be given in the next chapter.

Equation (18) represents a major breakthrough not only in the study of Josephson junction arrays, but also in the more general study of coupled phase oscillators. It was the first time a quantitative connection had been made between a real physical system and the Kuramoto model. The Kuramoto model [62, 86] was derived to model systems that contain numerous oscillators that are coupled in some way. If the dynamics are such that the oscillators are operating near their limit cycles, the amplitudes may be ignored and the phases of each oscillator become the dominant dynamical variables of the problem. The Kuramoto model describes this type of behavior, and makes the further assumption that the coupling depends only on the differences of the phases. Equation (18) is an example of just this type of system. One drawback of the model, however, is the loss of amplitude information. If one is concerned with the output power of the oscillators, it is not enough that they all be synchronized. If the amplitude of oscillation is small, then so, too, is the output power. This difficulty will become apparent in Chapter 3, when we will find regimes in which all of the junctions will be synchronized, yet the output power is small.

Swift and Wiesenfeld were able to analyze Equation (18) and derive a previously known rule for synchronization, namely that stable in-phase solutions exist provided

$$\omega > \omega_0, \tag{19}$$

where $\omega = (\hbar/2eRI_c)\sqrt{I_b/I_c - 1}$ is the frequency of oscillations of the (uncoupled) junctions, and $\omega_0 = \sqrt{1/LC}$ is the angular frequency of the load in the absence of the load resistance. Therefore, for large enough bias currents, in-phase states should be seen. If, however, the bias current is too small (but still larger than the critical current), the in-phase solutions become unstable. This behavior is illustrated in Figure 7. For small bias currents, resulting in $\omega < \omega_0$, the behavior of the system is incoherent (Figure 7(a)). However, whenever the bias current is large enough so that $\omega > \omega_0$ the in-phase state becomes stable, resulting in

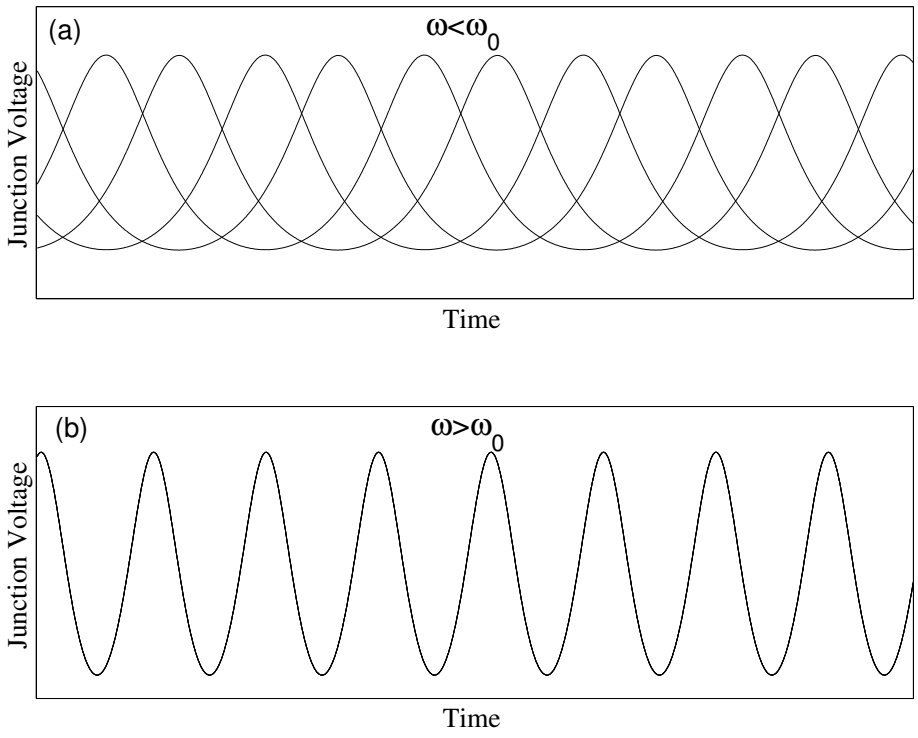

Figure 7: Junction voltage vs. time plots of an array consisting of 4 junctions obtained from direct integration of Equations (13) and (14). In (a) the bias current is such that $\omega < \omega_0$, resulting in an incoherent state. In (b) the bias current has been increased so that $\omega > \omega_0$, leading to stable in-phase oscillations (so that all four traces now coincide).

coherent voltage oscillations (Figure 7(b)).

2.3 Beyond the Kirchhoff Limit

In the previous section the qualifier "Kirchhoff limit" was used repeatedly during the discussion. But what exactly is the Kirchhoff limit, and why is it (seemingly) so important to the analysis? Let us examine each rule (the loop rule and the node rule) to find out exactly when they are valid.

First, let us look at the loop rule. The loop rule states that "[t]he algebraic sum of the changes in potential encountered in a complete traversal of any loop of a circuit must be zero [39]." Mathematically this can be stated in terms of the line integral

$$\oint \mathbf{E} \cdot \mathrm{d}\mathbf{l} = 0, \tag{20}$$

where $\mathbf{E}$ is the electric field. Using Stokes's Theorem, we can change the line integral into

an area integral, giving us

$$\oint \mathbf{E} \cdot \mathrm{d}\mathbf{l} = \int \nabla \times \mathbf{E} \cdot \mathrm{d}\mathbf{a} = 0. \tag{21}$$

Next, we realize that the curl of the electric field is related to the magnetic field through Faraday's law, giving us

$$\int \frac{\partial \mathbf{B}}{\partial t} \cdot \mathrm{d}\mathbf{a} = 0, \tag{22}$$

where $\mathbf{B}$ is the magnetic field. Finally, since it is true for any loop (and therefore any area), it must be that

$$\frac{\partial \mathbf{B}}{\partial t} = 0. \tag{23}$$

Before we get into what it means that the magnetic field is constant in time in the Kirchhoff limit, let us first examine Kirchhoff's other law, the node rule. It states that "[t]he sum of the currents entering any [node] must be equal to the sum of the currents leaving that [node] [39]." This means that the divergence of the current density is zero everywhere within the wire. Mathematically, this becomes

$$\nabla \cdot \mathbf{j} = 0, \tag{24}$$

where $\mathbf{j}$ is the current density in the wire. Using the Ampère-Maxwell relation to substitute for $\mathbf{j}$ gives us

$$\nabla \cdot \left\{ v^2 \nabla \times \mathbf{B} - \frac{\partial \mathbf{E}}{\partial t} \right\} = 0, \tag{25}$$

where v is the speed of light within the wire. The divergence of a curl must be zero, leaving us with

$$\nabla \cdot \frac{\partial \mathbf{E}}{\partial t} = 0. \tag{26}$$

Finally, the use of Gauss's law gives us

$$\frac{\partial}{\partial t} \nabla \cdot \mathbf{E} = \frac{1}{\epsilon_0} \frac{\partial \rho}{\partial t} = 0, \tag{27}$$

where ρ is the charge density within the wire.

So there appear to be two conditions that are necessary in order for Kirchhoff's laws to hold. They are

$$\frac{\partial \mathbf{B}}{\partial t} = 0 \tag{28}$$

and

$$\frac{\partial \rho}{\partial t} = 0. \tag{29}$$

Both are constraints on the constancy of the system. The first requires the magnetic field to be constant, while the second requires the charge density to be constant. The second constraint, Equation (29), is also an incompressibility condition because it constrains us to treat the charge carriers in the wire as an incompressible fluid. In other words, charge cannot accumulate (or be taken away from) any point within the wire. Charges can still move, but whenever they do they are immediately replaced to conserve the charge density. Note that this is a more stringent condition than the current conservation condition given by

$$\nabla \cdot \mathbf{j} + \frac{\partial \rho}{\partial t} = 0, \tag{30}$$

which is always true for any system. For Kirchhoff systems, Equation (30) still holds, but now *each* term must be identically zero.

The constraint on the induced magnetic field, Equation (28), puts a limit on how fast the system changes. If the circuit is oscillating very fast, then so too will the induced magnetic field. This means that the time derivative of the magnetic field can get very large at times. But how large is too large? To answer this we note that the frequency of magnetic field fluctuations is related to the wavelength according to $\lambda = v/f$, where v is the velocity. If the wavelength of the field is much larger than the characteristic length scale of the circuit, then Equation (28), while not precisely true, is a good approximation, and Kirchhoff's laws will hold. If, however, the wavelength is comparable to (or even smaller than) the circuit size, then Kirchhoff's laws will *not* hold, and any dynamical equations derived from them will be invalid.

As it happens, the twin technological goals of generating higher operating frequencies and larger output powers (and thus more junctions) in Josephson junction arrays both work against the Kirchhoff limit. This is illustrated in Figure 8. The oscillator frequency, f, sets the radiation wavelength $\lambda = c/nf$, where c is the speed of light in a vacuum and n is the index of refraction of the wire. Meanwhile, the total length of the system is $l = Nd$, where N is the total number of junctions and d is the average spacing between junctions.

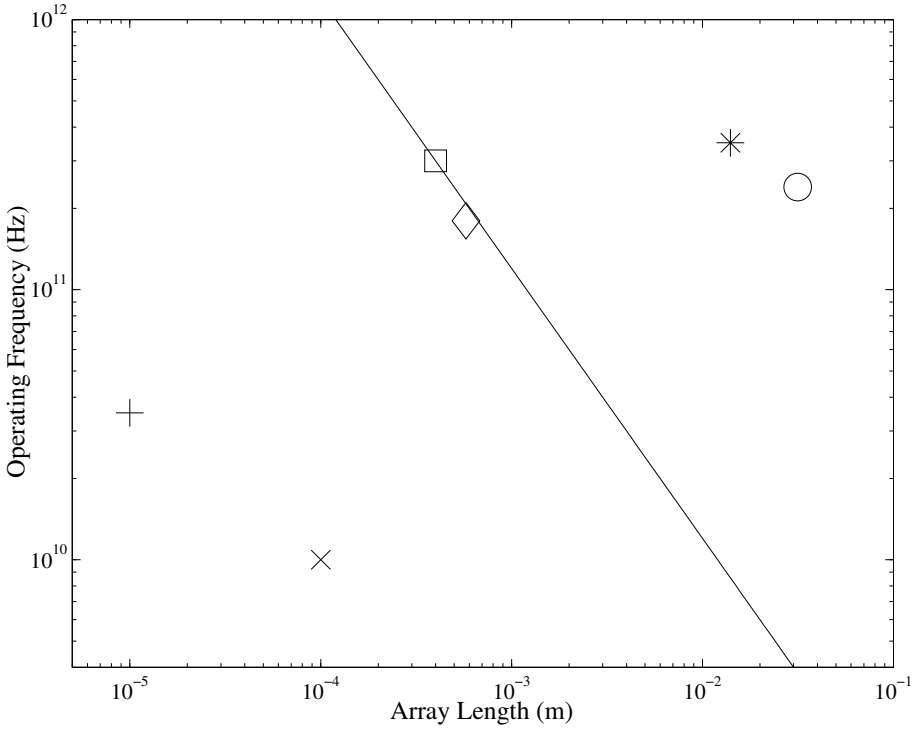

Figure 8: Curve $f = c/nl$ showing where the radiation wavelength equals the spatial extent of the array (here n is taken to be 2.5, which is typical for Josephson arrays). As the length of the array increases, the frequency regime of the Kirchhoff limit decreases. Also indicated are the points at which some experimental arrays operated. (Bi et al. ($\square$) [11]; Booi and Benz ($\circ$) [13]; Jain et al. ($\times$) [53]; Wan et al. ($*$) [96]; Vasilić et al. ($\diamond$) [94]; and Ovsyannikov et al. ($+$) [78].)

(The junctions themselves are typically much smaller than d.) To take an example, an array operating at 300 GHz – not a particularly high frequency for Josephson junctions – corresponds to a wavelength of 0.4 millimeters when the index of refraction is 2.5; for a typical spacing of 10μm, this is about the same size as an array of about 40 junctions – not a particularly large number for Josephson arrays (arrays consisting of millions of junctions are now being built [15]).

Since Josephson junction arrays are being pushed past the Kirchhoff limit experimentally, we must go beyond Kirchhoff's laws analytically. It therefore becomes necessary to treat the wire as a dynamical entity by allowing current to be non-uniform along its length. To this end we use a model derived by Cawthorne et al. [16] which treats the wire as a transmission line. This model adds to the wire a capacitance and an inductance per unit

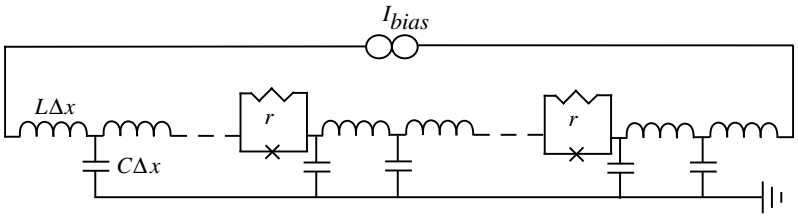

Figure 9: Schematic of a distributed series array with constant current source I_{bias}. The junctions have resistance r and zero capacitance (the ideal part of a junction is denoted by a cross). The wire has an inductance per unit length L and capacitance per unit length C.

length. Since Josephson junction arrays use superconducting wires in their circuitry, the resistance per unit length of the wire is ignored. A schematic of this situation is given in Figure 9. Notice that there is no load present in the array. As we will soon see, the transmission line nature of the wire is enough to couple the junctions to one another, so that no load is required. The case when both the transmission line and the load are present was studied numerically by Cawthorne et al. [16, 17]. However, in an attempt to make analytic progress we will restrict ourselves to this simpler, loadless model.

Paradoxically, this new model, which is necessary because of the breakdown of Kirchhoff's laws, must be analyzed using those same laws. However, since each use of Kirchhoff's laws will be on loops of some arbitrarily small linear size Δx, they will be valid provided the length scales of current variation are large compared to Δx. In the limit $\Delta x \to 0$ this will necessarily be true.

We can now derive a new system of equations for the array by examining a section of the transmission line containing one junction, as shown in Figure 10. Looking at the node between the two inductors tells us that

$$I_{i-1} = I_i + \dot{q}_i. \tag{31}$$

Next, using the loop rule on the loop *not* containing the junction gives us

$$\frac{q_{i-1}}{C\Delta x} = L\Delta x \frac{\mathrm{d}I_{i-1}}{\mathrm{d}t} + \frac{q_i}{C\Delta x}. \tag{32}$$

Taking the time derivative of Equation (32) and substituting Equation (31) into it yields

$$\frac{\mathrm{d}^2 I_{i-1}}{\mathrm{d}t^2} - v^2 \left\{ \frac{I_i - 2I_{i-1} + i_{i-2}}{\Delta x^2} \right\} = 0, \tag{33}$$

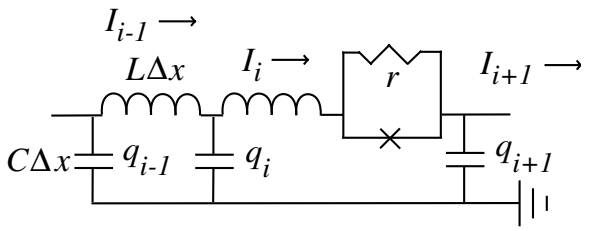

Figure 10: A close up of a section of a transmission wire containing a Josephson junction. The current through the i^{th} inductor is I_i, while the charge on the i^{th} capacitor is q_i.

where $v = \sqrt{1/LC}$ is the wave speed within the wire. In the limit $\Delta x \to 0$, and equating $I_i(t) = I(x,t)$, this becomes

$$\frac{\partial^2 I}{\partial t^2} - v^2 \frac{\partial^2 I}{\partial x^2} = 0. \tag{34}$$

Equation (34) is true throughout the lossless transmission wire, provided there are no Josephson junctions. We can glean the effect of the junctions when we examine the other loop in Figure 10. The junction gives us another voltage drop, turning Equation (32) into

$$\frac{q_i}{C\Delta x} = L\Delta x \frac{\mathrm{d}I_i}{\mathrm{d}t} + \frac{q_{i+1}}{C\Delta x} + \frac{\hbar}{2e}\dot{\phi}. \tag{35}$$

If we again take the time derivative and use Equation (31) we arrive at

$$\frac{\mathrm{d}^2 I_i}{\mathrm{d}t^2} - v^2 \left\{ \frac{I_{i+1} - 2I_i + i_{i-1}}{\Delta x^2} \right\} = -\frac{\hbar}{2eL\Delta x}\ddot{\phi}. \tag{36}$$

We must now be careful when we take the limit $\Delta x \to 0$. The term on the right-hand side of the equation will go to infinity in that limit. We realize, however that this happens only at the i^{th} segment. If the junction is at a position $x = x_J$ then we may equate $I_i(t) = I(x,t)$ provided

$$\lim_{\Delta x \to 0} \frac{\hbar}{2eL\Delta x}\ddot{\phi} = \frac{\hbar}{2eL}\ddot{\phi}\delta(x - x_J). \tag{37}$$

If there are N junctions such that the j^{th} junction is at $x = x_j$ then we may write

$$\frac{\partial^2 I}{\partial t^2} - v^2 \frac{\partial^2 I}{\partial x^2} = -\sum_{j=1}^{N} \frac{\hbar}{2eL}\ddot{\phi}_j \delta(x - x_j). \tag{38}$$

Since the wire in question begins and ends at the constant current source, we must add the boundary conditions

$$I(0,t) = I(l,t) = I_{\text{bias}}, \tag{39}$$

where l is the total length of the wire.

The dynamical equation governing the junctions is very similar to that derived for the Kirchhoff limit array. Recall that Equation (9) described the dynamics of a single junction driven by a constant current source. If we look at Figure 10 we see that the junction is in a very similar situation, except that instead of a constant current source, we now have a time dependent and spatially local current driving the junction. We therefore can modify Equation (9) by replacing I_b with the correct value of the local current. This gives us, for the phase of the j^{th} junction,

$$\frac{\hbar}{2er}\dot{\phi}_j + I_{\text{c}} \sin \phi_j = I(x_j, t). \tag{40}$$

Equations (38) and (40), along with the boundary condition, Equation (39) now give a complete description of the dynamics of high frequency Josephson junction arrays of the type shown in Figure 9. Because the positions of each of the junctions is now important, this model is called the Distributed Josephson Junction Array model. The analysis of this system will be the topic of the next chapter.

CHAPTER 3

DISTRIBUTED JOSEPHSON JUNCTION ARRAYS

To date, theorists have paid relatively little attention to the dynamics of Josephson arrays at high frequencies. The problem was first taken up in 1999 by Cawthorne et al., who did numerical studies of series arrays with a load [16], and in 2002 by Almaas and Stroud, who studied the effects of high frequency operation in a resonant cavity [2]. The problem is considerably more complicated than its low frequency counterpart and we will confine ourselves to the simplest version of the problem, namely where the load is absent. As demonstrated in Section 2.2.1, this case is trivial in the Kirchhoff limit: without a load the junctions are uncoupled and there is no hope of synchronization. But at higher frequencies the current in the wire is not necessarily spatially uniform, so the wire becomes a significant dynamical entity which couples the junctions along its length. Tsygankov and Wiesenfeld were able to show that this can provide sufficient coupling to induce synchronization in uniform arrays [92].

As we saw in the previous chapter, the governing dynamical equations are

$$\frac{\hbar}{2er}\dot{\phi}_j + I_c \sin\phi_j = I(x_j,t) \qquad j = 1,2,\ldots,N \tag{41}$$

$$\frac{\partial^2 I}{\partial t^2} - v^2\frac{\partial^2 I}{\partial x^2} = -\sum_{j=1}^{N}\frac{\hbar}{2eL}\ddot{\phi}_j\delta(x-x_j), \tag{42}$$

where $I(x,t)$ is the current in the wire at position x and time t; v and L are the wave speed and inductance per unit length of the wire, respectively. The first equation is the statement of current conservation for each (point) junction. The second is the evolution equation for a lossless transmission line with each junction acting as a spatially localized, time dependent voltage source. The boundary conditions are

$$I(0,t) = I(l,t) = I_{\text{bias}} \tag{43}$$

where l is the length of the wire and I_{bias} is the bias current. As in Chapter 2, the bias current

is again the most accessible parameter experimentally, as it sets the oscillator frequency.

The goal is to have an attracting in-phase state, so that the junction voltages (proportional to $\dot{\phi}_j$) all oscillate with the same frequency and phase. It is also desirable that the amplitude of the oscillations be as large as possible. It is debatable whether the in-phase state has ever been achieved in any real Josephson junction array; estimates suggest [98, 99] that existing arrays need to use junctions which are matched to within one or two percent, which is just barely attainable with existing technology [21].[1] What is certain is that the best reported results for total output power at high frequencies used spatially non-uniform arrays built with a periodic structure. The idea behind the "resonant architecture" used in these experiments is as follows. Since, in the absence of any junctions, the equation governing the current distribution, Equation (42), is a wave equation, the solutions will be standing waves (normal modes) with nodes at each end of the wire, each with its own resonant frequency. Imagine that the junctions oscillate at a frequency close to the resonant frequency of one of the normal modes of the transmission line. Then one expects a large amplitude response of this particular mode; if the junctions are placed at "equivalent positions" relative to this mode, they will all feel the same (large) AC drive, which presumably is beneficial for generating in-phase oscillations. Moreover, one expects the most effective scheme would be to place the junctions at antinodes of the resonant mode.

The situation is depicted in Figures 11 and 12. In Figure 11 each of the six junctions is placed at an antinode (of the same polarity) of the normal mode. If the current is dominated by that particular mode, then the junctions will each experience the same AC current. If, on the other hand, the junctions are placed in a different manner, as in Figure 12, then each junction will experience a different driving current than the rest. It is reasonable to assume that the first case, where the junctions are commensurate with the current mode, will be more likely to synchronize than the second. But what about a situation as the one depicted in Figure 13? Here the junctions are placed commensurate with the mode, but are bunched about the antinodes. There will now be differences in the currents that each

[1] We refer here to arrays of capacitanceless junctions. The situation is predicted to be better for junctions with an optimized capacitance

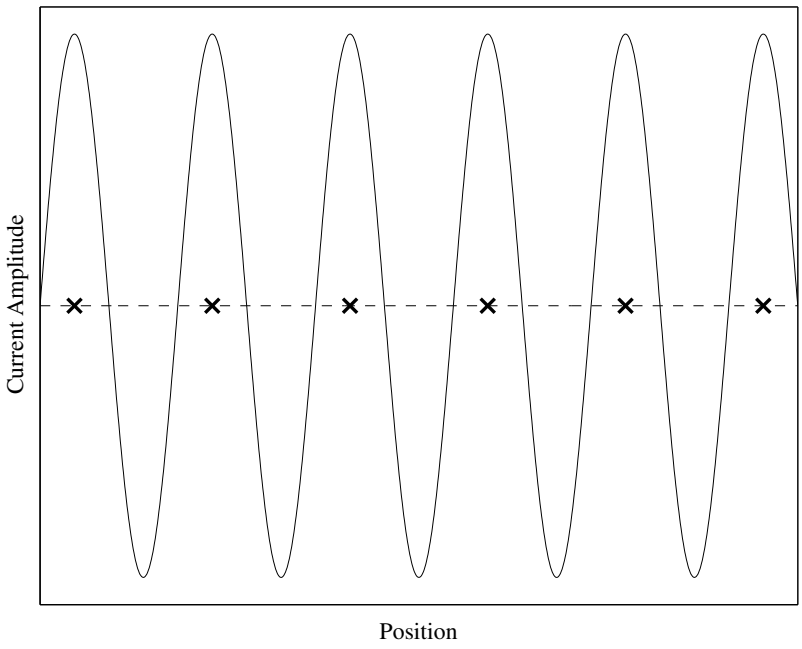

Figure 11: A depiction of a configuration of junctions (denoted by crosses) that is commensurate with a particular normal mode. Here, each of the junctions is placed at an antinode so that the local current is the same for each.

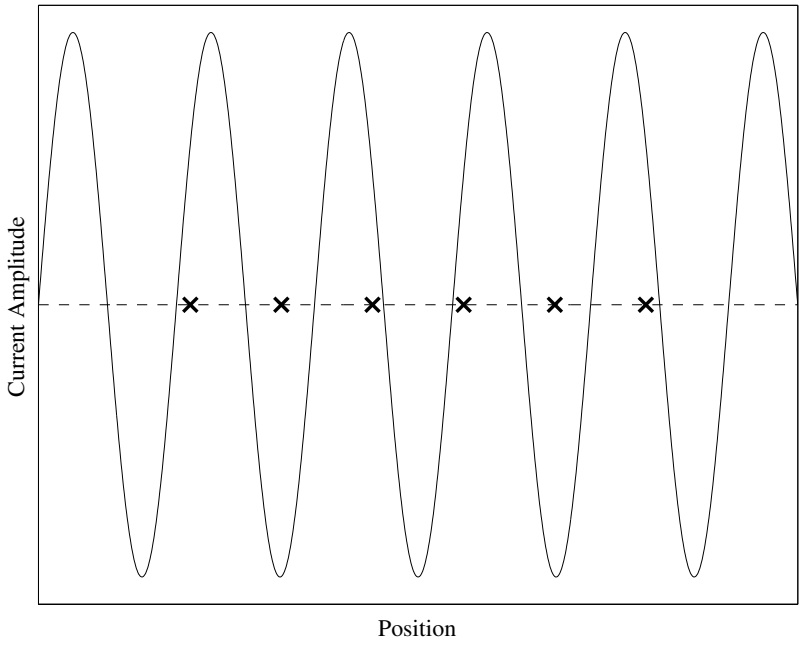

Figure 12: A depiction of a configuration of junctions (denoted by crosses) that is *not* commensurate with a particular normal mode. Here, the junctions are placed such that there are differences in the local current.

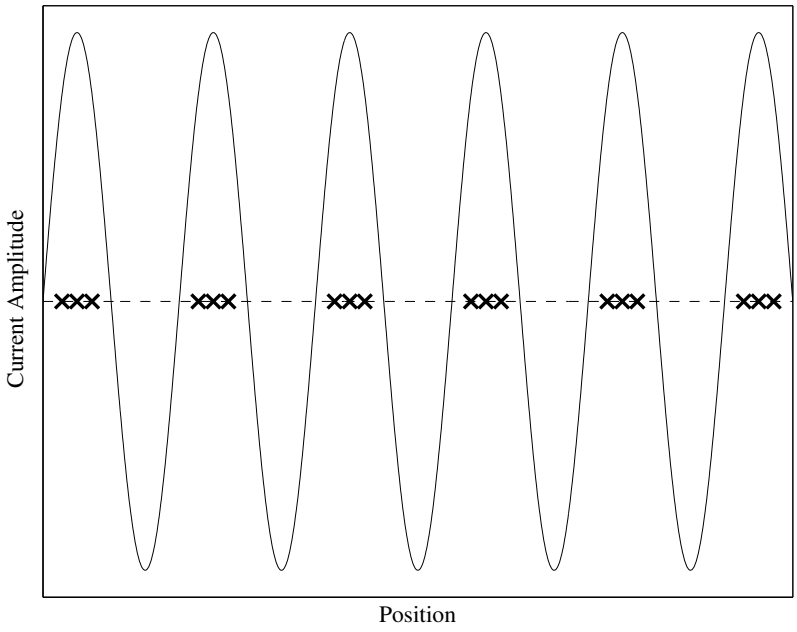

Figure 13: A depiction of a configuration of junctions (denoted by crosses) that is commensurate with a particular normal mode, but bunched around the antinodes. Differences in the currents seen by the junctions will be small.

junction sees, but these differences should be small. It is also not out of the question that this configuration would also synchronize.

This picture has a strong physical appeal, and experimentalists have tried to take advantage of the fact that spatial positioning of the junctions is important in the high frequency regime. Han et al. [11, 41] and Booi and Benz [13] demonstrated that clustering junctions at strategic locations along the wire connecting them can increase the emitted power. There is almost no theoretical work, however, to justify this strategy [65, 84]. Naturally, it would be desirable to put the basic idea on a firm quantitative footing (assuming that it is correct). Beyond this, the picture leaves open certain rather important practical questions. For example, to maximize the total power it is desirable to maximize the number of in-phase junctions. If one places a group of junctions near each equivalent site, how large (relative to the mode wavelength) can this group be? Similarly, is it acceptable to place junctions (or groups of junctions) at each half-wavelength [11, 13] rather than at each wavelength [41]? It has been argued that although neighboring antinodes represent local current flow of opposite polarity, this is irrelevant for the purposes of synchronization [11, 13].

In the first part of our analysis we will apply an averaging scheme similar to that used by Swift and Wiesenfeld [89], who studied the lumped (Kirchhoff limit) version of the problem. The averaging scheme will give us a reduced model for the phase dynamics of the junctions similar to Equation (18). This particular technique has played a central role in a number of advances in the study of lumped Josephson arrays – in understanding the massive neutral stability of splay phase states [97]; in establishing the connection with the Kuramoto model [98, 99]; and in deriving the frequency matching condition for stability of the in-phase state [89].

After deriving the averaged equations, we will investigate whether spatially clustered arrays have better synchronization properties than uniform arrays. We find that, when driven near resonance, tightly clustered arrays tend to phase lock better than non-clustered arrays. However, we also find that increasing the number of junctions within a cluster can diminish synchronization and even wipe it out entirely. Our analysis of a few well-chosen cases leads us to a clear understanding of these effects.

3.1 Derivation of Averaged Equations

We begin by putting Equations (41) and (42) into dimensionless form. We make the following rescalings

$$\frac{2erI_{\rm c}}{\hbar}t \to t \quad , \quad \frac{I}{I_{\rm c}} \to I \quad , \quad \frac{x}{l} \to x, \tag{44}$$

and introduce spatial Fourier decompositions

$$I(x,t) = I_{\rm b} + \sum_{k=1}^{\infty} A_k(t)\sin(\pi k x), \tag{45}$$

$$\delta(x - x_j) = \sum_{k=1}^{\infty} 2\sin(\pi k x_j)\sin(\pi k x). \tag{46}$$

With these Equations (41) and (42) become

$$\dot{\phi}_j + \sin\phi_j = I_{\rm b} + \sum_{k=1}^{\infty} a_{jk}A_k \qquad j = 1, 2, \ldots, N \tag{47}$$

$$\ddot{A}_k + \omega_k^2 A_k = -2\alpha \sum_{j=1}^{N} a_{jk}\ddot{\phi}_j \qquad k = 1, 2, \ldots \infty \tag{48}$$

where the overdot now denotes differentiation with respect to the dimensionless time and

$$\alpha = \frac{\hbar}{2eI_{\rm c}Ll}, \tag{49}$$

$$\omega_k = \frac{\pi\hbar kv}{2erlI_{\rm c}}, \tag{50}$$

$$I_{\rm b} = \frac{I_{\rm bias}}{I_{\rm c}}, \tag{51}$$

$$a_{jk} = \sin(\pi k x_j). \tag{52}$$

We now follow the averaging procedure of References [89, 103]. First, we transform the phases ϕ_j into the natural angles ψ_j given by

$$\psi_j(\phi_j) = 2\tan^{-1}\left[\sqrt{\frac{I_{\rm b}-1}{I_{\rm b}+1}}\tan\left(\frac{\phi_j}{2}+\frac{\pi}{4}\right)\right] \tag{53}$$

$$\phi_j(\psi_j) = 2\tan^{-1}\left[\sqrt{\frac{I_{\rm b}+1}{I_{\rm b}-1}}\tan\left(\frac{\psi_j}{2}\right)\right] - \frac{\pi}{2}. \tag{54}$$

The ψ_j variables are "natural" in the sense that the angular velocities $\dot{\psi}_j$ are constant in the uncoupled limit, whereas the corresponding $\dot{\phi}_j$ are not. Differentiating Equation (47) and substituting the resulting expression for $\ddot{\phi}$ into Equation (48) yields

$$\dot{\psi}_j = 1 + \sum_{k=1}^{\infty}\frac{a_{jk}A_k}{I_{\rm b}-\sin\phi_j} \tag{55}$$

$$\omega^2\ddot{A}_k + \omega_k^2 A_k = -2\alpha\sum_{j=1}^{N} a_{jk}\Big\{\sin\phi_j\cos\phi_j - I_{\rm b}\cos\phi_j + \sum_{l=1}^{\infty} a_{jl}(\omega\dot{A}_l - A_l\cos\phi_j)\Big\}. \tag{56}$$

where $\omega = \sqrt{I_{\rm b}^2-1}$ and we have rescaled time once again: $\omega t \rightarrow t$.

The sum over l is a significant complication since it couples together all of the modes. Our simulations show that we cannot summarily drop these terms. On the other hand, our simulations also show that the relevant contribution of the $A_l\cos\phi_j$ term is smaller than the $\omega\dot{A}_l$ term by a factor of approximately $I_{\rm b}^2$, and that neglecting only the $A_l\cos\phi_j$ term yields accurate results. In what follows, we make this (uncontrolled) approximation since it substantially simplifies the ensuing analysis.

We also use the trigonometric identities

$$\cos\phi = \frac{\omega\sin\psi}{I_{\rm b}-\cos\psi} \quad , \quad \sin\phi = I_{\rm b} - \frac{I_{\rm b}^2-1}{I_{\rm b}-cos\psi} = \frac{1-I_{\rm b}\cos\psi}{I_{\rm b}-\cos\psi} \tag{57}$$

to write

$$\sin\phi_j\cos\phi_j - I_\mathrm{b}\cos\phi_j = \frac{C_0}{2} + \sum_{p=1}^{\infty}(B_p\sin(p\psi_j) + C_p\cos(p\psi_j)). \tag{58}$$

where, in particular, $C_0 = C_1 = 0$ and

$$B_1 = 2\omega^2(\omega - I_\mathrm{b}). \tag{59}$$

We will see later that in the sum over p in Equation (58) only the term involving $\sin\psi$ survives the averaging procedure, so we can safely ignore all terms with $p > 1$. Dropping these, Equation (56) becomes

$$\omega^2\ddot{A}_k + \omega_k^2 A_k = -2\alpha\sum_{j=1}^{N} a_{jk}B_1\sin\psi_j - 2\alpha\omega\sum_{l=1}^{\infty}\sum_{j=1}^{N} a_{jk}a_{jl}\dot{A}_l. \tag{60}$$

The averaging scheme treats the coupling term in Equation (55) as small, so that in the uncoupled limit $\psi_j(t) = t + \gamma_j$, where γ_j is the initial value of ψ_j. Substituting this into Equation (60) leads to a steady state solution

$$A_k = M_k\sin t + N_k\cos t. \tag{61}$$

where the M_k and N_k are determined by the linear system

$$(\omega_k^2 - \omega^2)M_k - \sum_{l=1}^{\infty}\eta_{kl}N_l = f_k \tag{62}$$

$$(\omega_k^2 - \omega^2)N_k + \sum_{l=1}^{\infty}\eta_{kl}M_l = g_k, \tag{63}$$

with

$$f_k = -2\alpha\sum_{j=1}^{N} a_{jk}B_1\cos(\gamma_j) \quad , \quad g_k = -2\alpha\sum_{j=1}^{N} a_{jk}B_1\sin(\gamma_j)$$

and

$$\eta_{kl} = 2\alpha\omega\sum_{j=1}^{N} a_{jk}a_{jl}. \tag{64}$$

Our task is now to find the coefficients M_k and N_k in Equations (62) and (63). To accomplish this, we first introduce an integer cut-off parameter k_max, truncating the infinite sums. In practice, k_max should be large, but not so large that the actual physical size of the junctions is comparable to the wavelength $2\pi/k_\mathrm{max}$ of the cutoff mode. (Recall that the

transmission line model Equation (42) treats the junctions as spatially point-like.) With this truncation the system (62) and (63) can be written as:

$$\begin{pmatrix} \boldsymbol{a} & -\boldsymbol{\eta} \\ \boldsymbol{\eta} & \boldsymbol{a} \end{pmatrix} \begin{pmatrix} \vec{M} \\ \vec{N} \end{pmatrix} = \begin{pmatrix} \vec{f} \\ \vec{g} \end{pmatrix} \tag{65}$$

where the matrix $\boldsymbol{\eta}$ is defined in Equation (64), $a_{kl} = (\omega_k^2 - \omega^2)\delta_{kl}$, and the vectors $\vec{M}$, $\vec{N}$, $\vec{f}$, and $\vec{g}$ are the $k_{\max}$-dimensional column vectors defined above.

The linear system (65) allows us to solve for M_k and N_k (numerically, in the general case). These, in turn, give us the solutions for the A_k's such that (cf. Equation (61)):

$$A_k = \sum_{j=1}^{N} \{[P_{jk}\cos\gamma_j + Q_{jk}\sin\gamma_j]\sin t + [R_{jk}\cos\gamma_j + S_{jk}\sin\gamma_j]\cos t\} \tag{66}$$

where:

$$P_{jk} = -2\alpha B^{(1)} \sum_{l=1}^{k_{\max}} a_{jl} T_{kl} \tag{67}$$

$$Q_{jk} = -2\alpha B^{(1)} \sum_{l=k_{\max}+1}^{2k_{\max}} a_{jl} T_{kl} \tag{68}$$

$$R_{jk} = -2\alpha B^{(1)} \sum_{l=1}^{k_{\max}} a_{jl} T_{(k+k_{\max})l} \tag{69}$$

$$S_{jk} = -2\alpha B^{(1)} \sum_{l=k_{\max}+1}^{2k_{\max}} a_{jl} T_{(k+k_{\max})l} \tag{70}$$

and

$$\mathbf{T} = \begin{pmatrix} \boldsymbol{a} & -\boldsymbol{\eta} \\ \boldsymbol{\eta} & \boldsymbol{a} \end{pmatrix}^{-\mathbf{1}} \tag{71}$$

is the $2k_{\max} \times 2k_{\max}$ solution matrix to system (65).

It is evident from Equation (71) that the matrix $\mathbf{T}$ will have the same block form as its inverse, provided it has one. In other words,

$$\mathbf{T} = \begin{pmatrix} \boldsymbol{U} & -\boldsymbol{V} \\ \boldsymbol{V} & \boldsymbol{U} \end{pmatrix}, \tag{72}$$

for some $k_{max} \times k_{max}$ dimensional matrices $\boldsymbol{U}$ and $\boldsymbol{V}$. If we examine the definitions of $\mathbf{P}$ and $\mathbf{S}$, above, we see that both contain the same sum over the matrix $\mathbf{U}$. Similarly, the

definitions of $\mathbf{Q}$ and $\mathbf{R}$ both contain the same sum over the matrix $\mathbf{V}$. This tells us that $\mathbf{P} = \mathbf{S}$ and $\mathbf{Q} = -\mathbf{R}$, allowing us to reduce Equation (66) to

$$A_k = \sum_{j=1}^{N} \Big\{ P_{jk} \sin(t + \gamma_j) - Q_{jk} \cos(t + \gamma_j) \Big\}. \tag{73}$$

Substitution of (73) into Equation (55) and using Equation (57) yields

$$\dot{\psi}_j = 1 + \sum_{k=1}^{k_{\max}} \frac{1}{\omega^2} a_{jk} A_k(t) (I_{\mathrm{b}} - \cos\psi_j). \tag{74}$$

We are now ready for the averaging step. We replace ψ_j on the right-hand side with its approximation $\psi_j = t + \gamma_j$ and average the resulting equation over one period:

$$\langle \dot{\psi}_j \rangle = 1 + \frac{1}{2\pi\omega^2} \sum_{k=1}^{k_{\max}} a_{jk} \int_0^{2\pi} A_k(t) (I_{\mathrm{b}} - \cos(t + \gamma_j)) dt \tag{75}$$

This last equation makes it apparent why only the first harmonics of A_k were needed: upon averaging, all higher harmonics integrate to zero.

The final step is to drop the angular brackets and replace the initial values γ_j by the slowly evolving ψ_j. This yields the final averaged equations

$$\dot{\psi}_j = 1 + \frac{1}{2\omega^2} \sum_{i=1}^{N} \sum_{k=1}^{k_{\max}} a_{jk} W_{ik} \sin(\psi_i - \psi_j + \Theta_{ik}) \tag{76}$$

where

$$W_{ik} = \sqrt{P_{ik}^2 + Q_{ik}^2} \quad \text{and} \quad \Theta_{ik} = \tan^{-1}\Big(\frac{Q_{ik}}{-P_{ik}}\Big). \tag{77}$$

Equation (76) can be further simplified to:

$$\dot{\psi}_j = 1 + \frac{1}{2\omega^2} \sum_{i=1}^{N} M_{ji} \sin(\psi_i - \psi_j + \Omega_{ji}), \tag{78}$$

with

$$M_{ji} = \sqrt{\Big(\sum_{k=1}^{k_{\max}} a_{jk} P_{ik} \Big)^2 + \Big(\sum_{k=1}^{k_{\max}} a_{jk} Q_{ik} \Big)^2} \quad \text{and} \quad \Omega_{ji} = \tan^{-1}\left[\frac{\sum_{k=1}^{k_{\max}} a_{jk} Q_{ik}}{-\sum_{k=1}^{k_{\max}} a_{jk} P_{ik}} \right]. \tag{79}$$

Equation (78) is our main result. In form it is very similar to the averaged equation for the loaded lumped circuit problem, Equation (18). When suitably rearranged that equation has the form [103]

$$\dot{\psi}_k = 1 + \rho \sum_{j=1}^{N} \sin(\psi_j - \psi_k - \delta), \tag{80}$$

where ρ and δ are constants. Equation (78) differs from (80) in two ways. First, the coupling constants M_{ji} and phase shifts Ω_{ji} are pair dependent. Second, although one has simple closed form expressions for ρ and δ, M_{ji} and Ω_{ji} must, in general, be computed numerically by solving the linear system Equation (65). On the other hand, we have derived Equation (78) without placing any restrictions on the placement of the junctions, so it is a useful starting point for studying various spatial configurations.

It should be noted here that both Equation (78) and Equation (80) are variations of the well-known Kuramoto model [61, 86]. That model, used to describe collections of N coupled phase oscillators typically has the form

$$\dot{\psi}_i = \omega_i + \frac{\kappa}{N}\sum_{j=1}^{N}\sin(\psi_j - \psi_i + \delta), \tag{81}$$

where κ and δ are some constants, and $i = 1 \ldots N$. Notice that in the Kuramoto model each oscillator has its own natural frequency, but the coupling is global and uniform. This type of asymmetry has been studied much more extensively than the coupling asymmetry present in our version, Equation (78). For the Kuramoto model it was found that synchronized solutions can exist provided the distribution of the natural frequencies, ω_i, was sufficiently narrow[2]. In other words, coherent behavior can still be observed provided the asymmetry is not too strong. This type of argument is the basis behind resonant architectures. If the asymmetry in the coupling in Equation (78) is made small enough, can coherent solutions exist? Answering this question will be the goal of the following sections.

3.2 Existence and Stability of In-phase States

In the usual terminology, an in-phase state is fully symmetric, i.e. $\phi_j(t) = \phi_1(t)$ for all j. While such solutions always exist for the lumped circuit problem Equations (13) and (15), they typically don't exist for the distributed problem, Equations (41) and (42). The same distinction holds for the corresponding averaged versions, Equations (18) and (78), respectively. This is because of the asymmetry inherent in the problem. A solution to the equations must either have the symmetry of the equations, or lower. This means that there

[2]For a wonderful review of this topic, please refer to the article by Strogatz [86].

is no hope of finding purely symmetric solutions unless we can find parameter regimes for which

$$\dot{\psi}_j = 1 + \frac{1}{2\omega^2} \sum_{i=1}^{N} M_{ji} \sin(\Omega_{ji}) \tag{82}$$

is independent of j. This corresponds to a symmetric solution ($\psi_j = \psi_i$) to Equation (78) in which each oscillator has a constant angular velocity. The oscillators will not stay in the symmetric state unless each angular velocity is constant, which can only happen if $\sum_{i=1}^{N} M_{ji} \sin \Omega_{ji}$ is independent of j. Note that this condition depends on both the junction positions and the operating frequency. This point is illustrated in Figure 14. This plot shows the normalized standard deviation of the sequence $\{\lambda_j\} = \{\sum_{i=1}^{N} M_{ji} \sin \Omega_{ji}\}$ as a function of ω. The dash-dot curve represents a configuration of ten junctions evenly spaced along the wire. As can be seen, an in-phase solution does not exist for any frequency $0 < \omega < 6$. The solid curve represents a configuration in which the ten junctions have been rearranged such that they are clustered about the points $x = 1/3$ and $x = 2/3$. The standard deviation has nearly gone to zero, so there are in-phase solutions except in a small range of operating frequencies near $\omega = 3$.

Interestingly, the transition between the uniformly distributed and clustered cases shown in Figure 14 is not uniform. This fact is illustrated in Figure 15. These three curves represent two clusters of 5 junctions each, centered about the points $x = 1/3$ and $x = 2/3$. As the total width of each cluster decreases there is no discernible pattern that arises. Only when the width of the clusters becomes extremely small does the standard deviation also become very small, as is seen in Figure 16. Even when the width of the clusters has gone to zero (Figure 17) there are still peaks in the standard deviation near some frequencies, even though the standard deviation is approximately zero for most frequencies. Interestingly, the peaks that appear in the standard deviation that appear for small values of ϵ have complicated structure. This is illustrated in Figure 18. This figure shows a close up of Figure 16 near $\omega = 3$. The existence and explanation of the complexity of these peaks is still poorly understood. It is most likely related to the node structure of the resonant mode corresponding to $\omega = 3$. The nodes of the third mode are at precisely $x = 1/3$ and $x = 2/3$, which are also the centers of the junction clusters. Why this would cause such a wide peak,

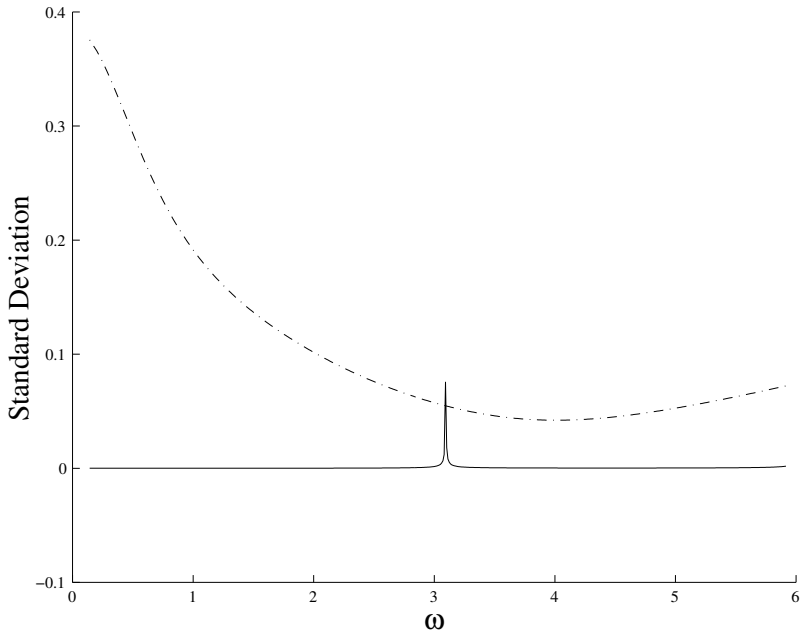

Figure 14: Normalized standard deviation of $\{\lambda_j\}$ versus ω. The two curves represent ten junctions placed evenly along the wire (dash-dot curve); and clustered about the points $x = 1/3$ and $x = 2/3$ (solid curve). A standard deviation near zero represents j-independence of λ_j and hence existence of in-phase solutions.

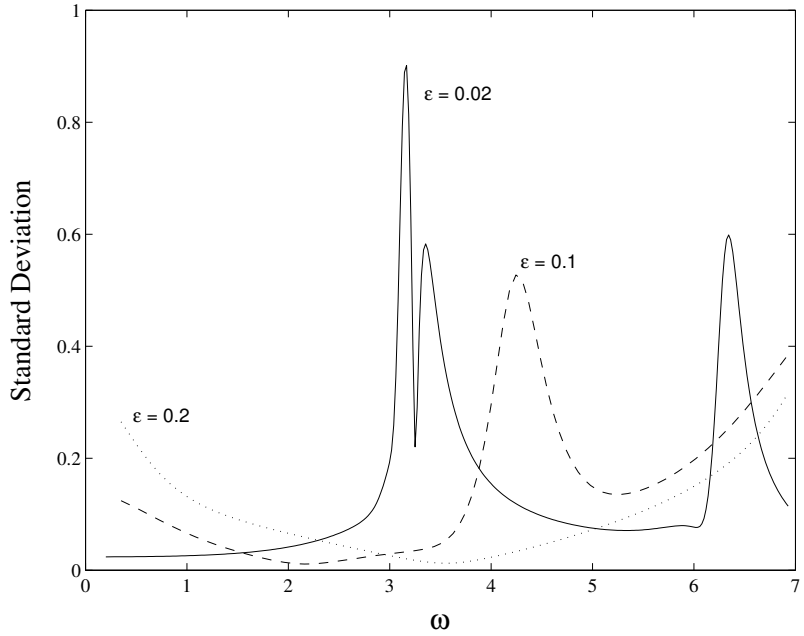

Figure 15: Normalized standard deviation of $\{\lambda_j\}$ versus ω. Here there are two clusters of 5 junctions each centered about the points $x = 1/3$ and $x = 2/3$. The total width of each cluster is 2ϵ. The three curves represent $\epsilon = 0.2$ (dotted curve), $\epsilon = 0.1$ (dashed curve) and $\epsilon = 0.02$ (solid curve).

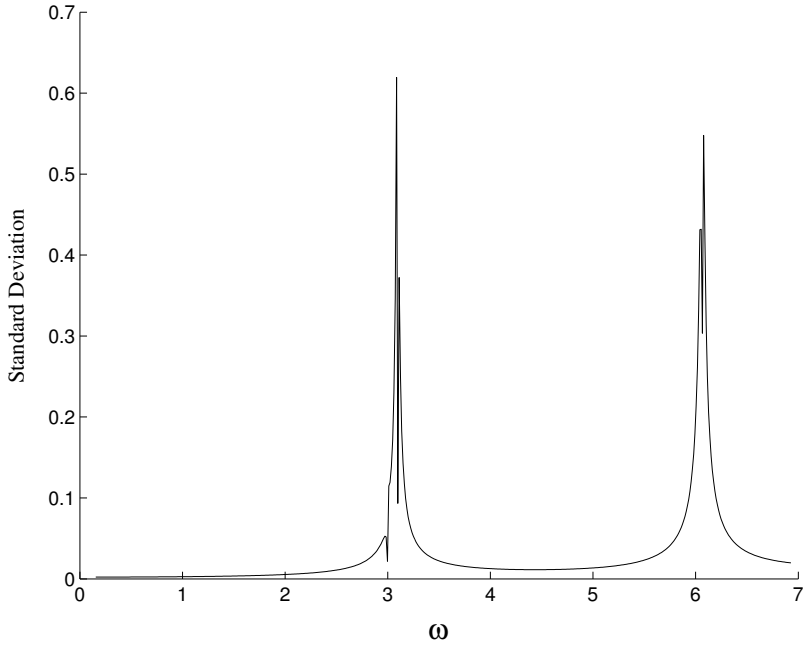

Figure 16: Normalized standard deviation of $\{\lambda_j\}$ versus ω. Here there are two clusters of 5 junctions each centered about the points $x = 1/3$ and $x = 2/3$. The half width of these clusters is $\epsilon = 0.002$.

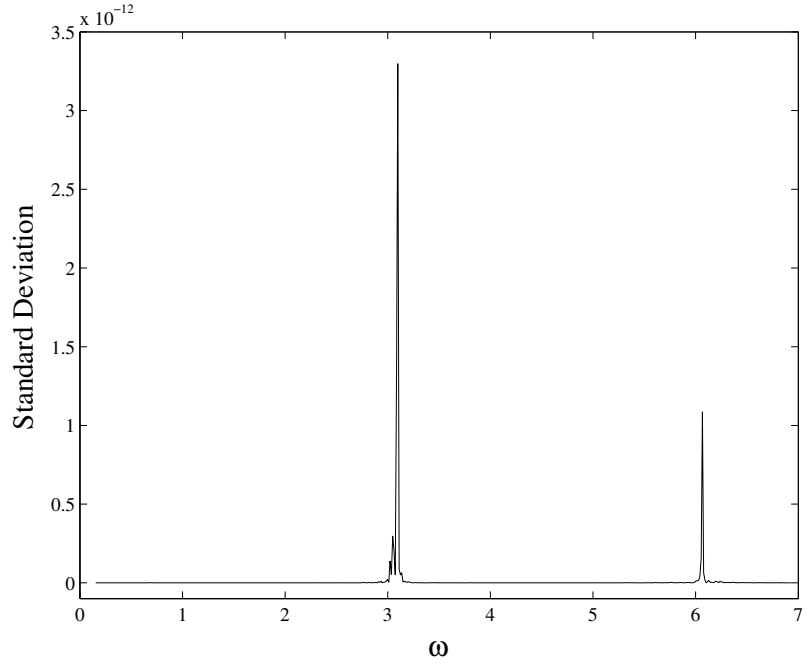

Figure 17: Normalized standard deviation of $\{\lambda_j\}$ versus ω. Here there are two clusters of 5 junctions each centered about the points $x = 1/3$ and $x = 2/3$. The half width of these clusters is $\epsilon = 0$.

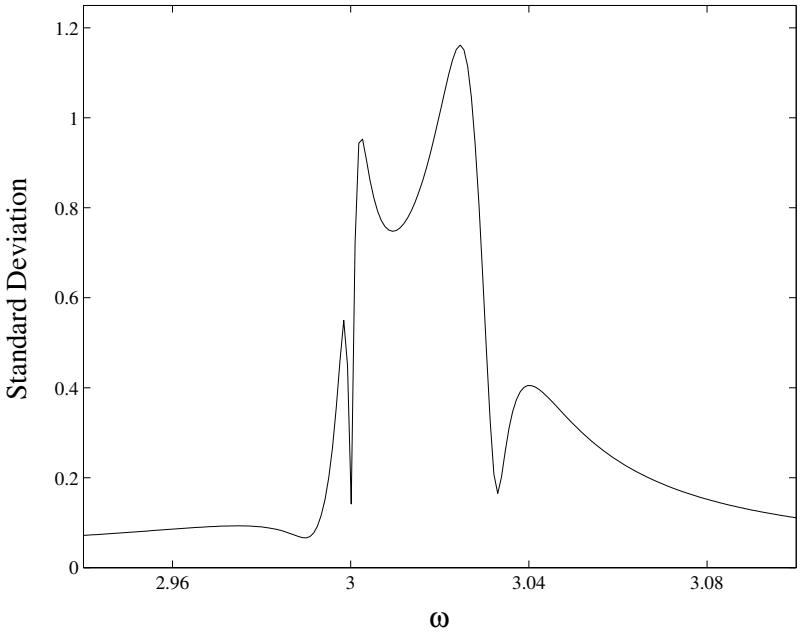

Figure 18: A closeup view of the normalized standard deviation of $\{\lambda_j\}$ versus ω. Here there are two clusters of 5 junctions each centered about the points $x = 1/3$ and $x = 2/3$. The half width of these clusters is $\epsilon = 0.002$.

though, is still a mystery.

Figure 19 shows a similar situation, but now with the ten junctions clustered about the points $x = 1/6$ and $x = 5/6$, corresponding to the two antinodes of the third mode that have the same parity. For $\epsilon = 0.1$ the standard deviation can be quite large, meaning that fully symmetric solutions do not exist. When $\epsilon = 0.02$, however, the standard deviation dips quite low near $\omega = 3$, the resonant frequency of the third mode. Plots of the standard deviation for even smaller values of ϵ are shown in Figure 20. For $\epsilon = 0.002$ the standard deviation has nearly gone to zero, except for peaks near $\omega = 1.5$ and $\omega = 4.5$. The smaller cluster size, $\epsilon = 0.0002$ does even better, but the two peaks still remain. Again, the existence of these peaks is a mystery, especially now since these do not correspond to resonant mode frequencies, but are in fact exactly in between them.

As a final example, let us examine the behavior of a grouping of junctions that puts clusters at every half wavelength of a desired mode. Imagine nine junctions in three clusters of three junctions each, centered about the points $x = 1/6$, $x = 1/2$ and $x = 5/6$, corresponding to all three of the antinodes of the third mode. The standard deviation for

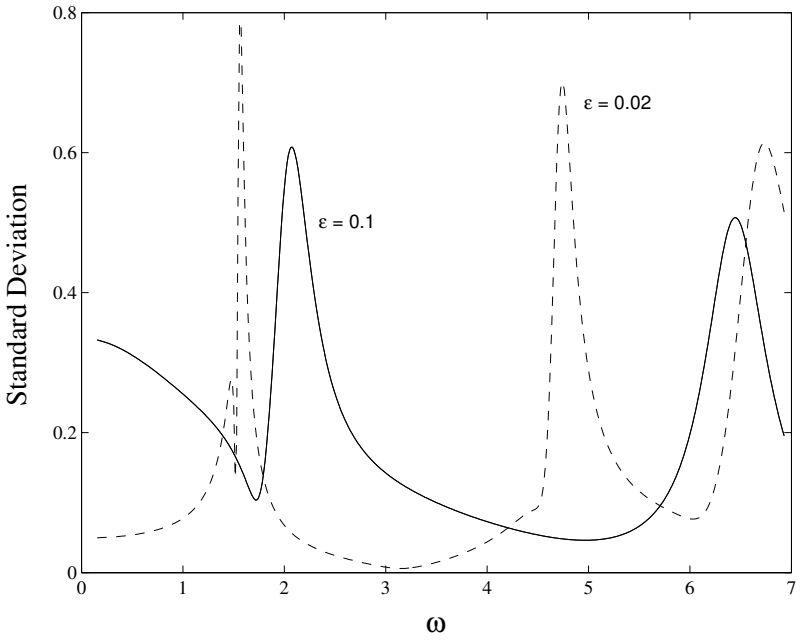

Figure 19: Normalized standard deviation of $\{\lambda_j\}$ versus ω. Here there are two clusters of 5 junctions each centered about the points $x = 1/6$ and $x = 5/6$. The total width of each cluster is 2ϵ. The two curves represent $\epsilon = 0.1$ (solid curve) and $\epsilon = 0.02$ (dashed curve).

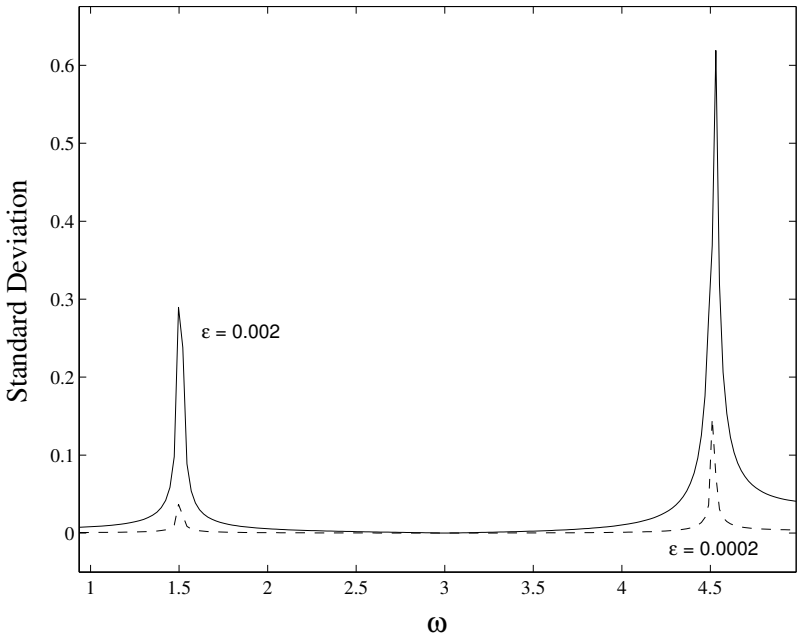

Figure 20: Normalized standard deviation of $\{\lambda_j\}$ versus ω. Here there are two clusters of 5 junctions each centered about the points $x = 1/6$ and $x = 5/6$. The total width of each cluster is 2ϵ. The two curves represent $\epsilon = 0.002$ (solid curve) and $\epsilon = 0.0002$ (dashed curve).

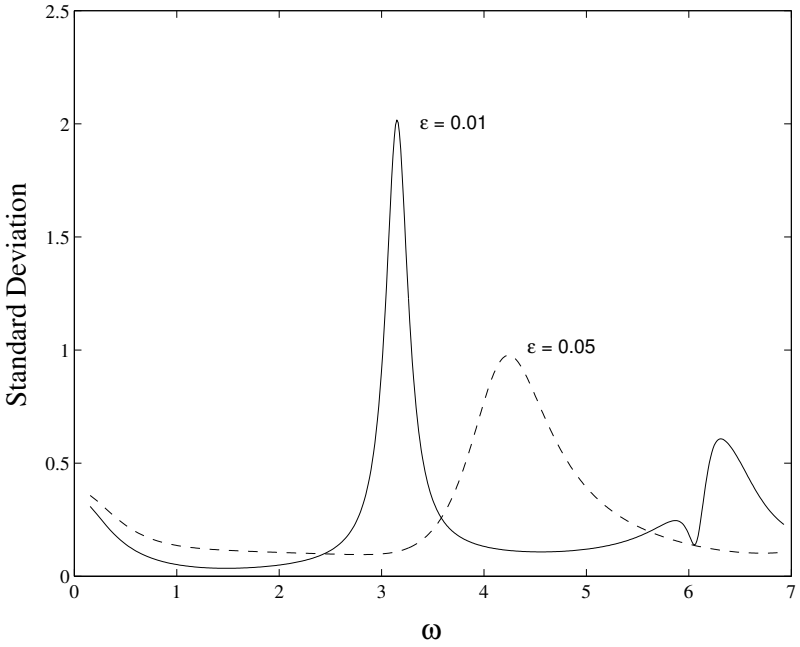

Figure 21: Normalized standard deviation of $\{\lambda_j\}$ versus ω. Here there are three clusters of 3 junctions each centered about the points $x = 1/6$, $x = 1/2$ and $x = 5/6$. The total width of each cluster is 2ϵ. The two curves represent $\epsilon = 0.01$ (solid curve) and $\epsilon = 0.05$ (dashed curve).

this configuration is shown in Figure 21. For $\epsilon = 0.05$ the standard deviation remains high, with a peak near $\omega \approx 4.5$. When the width decreases to $\epsilon = 0.01$ the peak shifts to $\omega = 3$. Figure 22 shows the same configuration with an extremely tight cluster, with $\epsilon = 10^{-7}$. This smaller cluster now shows a standard deviation near zero for most values of the frequency, yet the peak near $\omega = 3$ (the resonant frequency of our "preferred" mode) persists.

While the standard deviation calculations cannot tell us whether or not in-phase states are stable, they can at least tell us when they exist – and when they do exist it is straightforward to check their stability. Setting $\psi_j(t) = \psi_0(t) + \xi_j(t)$, we linearize Equation (78) for small ξ_j, with result

$$\dot{\xi}_j = \frac{1}{2\omega^2} \sum_{i=1}^{N} \left[\sum_{k=1}^{k_{\max}} a_{jk} P_{ik} \right] (\xi_j - \xi_i) \tag{83}$$

From here it is an easy matter to solve the linear system Equation (65) numerically, and hence find the stability matrix for Equation (83). The eigenvalues of the stability matrix determine the stability of the in-phase state. One eigenvalue is constrained to be zero (since

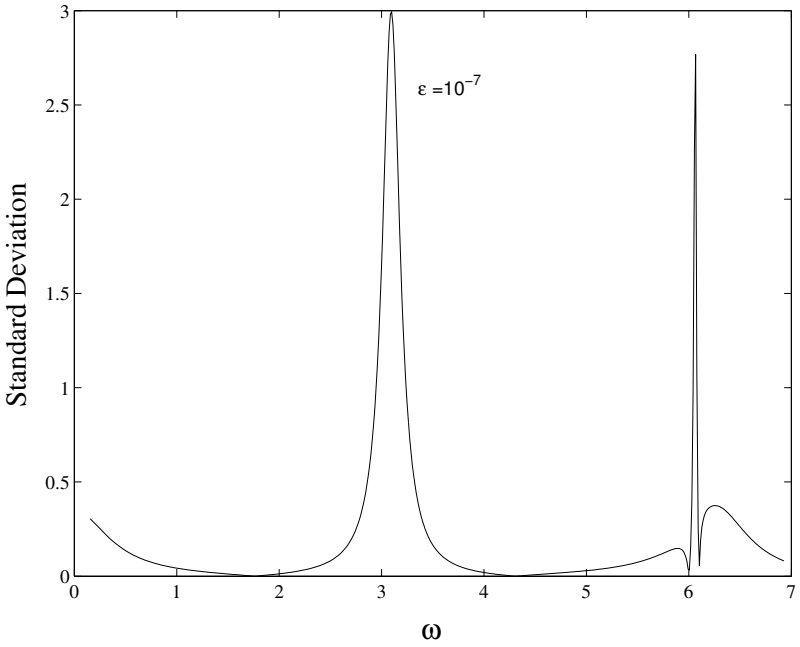

Figure 22: Normalized standard deviation of $\{\lambda_j\}$ versus ω. Here there are three clusters of 3 junctions each centered about the points $x = 1/6$, $x = 1/2$ and $x = 5/6$. The total width of each cluster is 2ϵ. This curve represent $\epsilon = 10^{-7}$.

the orbit is neutrally stable to perturbations tangent to it); if all other eigenvalues have negative real part then the in-phase state is linearly stable.

We have investigated the stability of the in-phase state for several array configurations that exhibit the necessary symmetry for in-phase solutions. There is good agreement between the eigenvalue analysis based on the averaged equations and direct numerical simulations of the differential Equations (47) and (48), especially when α is of the order of unity or smaller. For larger α the approximations made in the averaging derivation break down. We assumed that the coupling between the current modes A_k and the junctions ϕ_k was small. From Equation (48) it is clear that the larger α, the larger A_k; from Equation (47) we see that this increases the coupling to the junctions, in turn.

Figures 23 and 24 show plots of the largest non-zero eigenvalue determined from Equation (83) along with the total emitted power obtained by direct integration of Equations (47) and (48). The emitted power is calculated by time averaging the AC part of $\sum_{i=1}^{N} \dot{\phi}_i^2$ (since $\dot{\phi}$ is proportional to the voltage). Prominent in Figure 23 is the window around

$I_b \approx 3.5$ where the leading eigenvalue dips below zero (indicating stable in-phase solutions) and the emitted power is maximized. Above and below the narrow window the emitted power is low because the junction oscillations are incoherent. There is a much wider window of stable in-phase states for lower values of I_b; here the emitted power is relatively low because the voltage oscillation amplitude of the individual junctions is small. This is an important point. Simply because the junctions are all oscillating with the same phase does *not* mean that the output power will be large. Additionally, the amplitude of the voltage oscillations needs to be large in order to get an appreciable amount of power out of the system.

The dependence of the power on both the amplitudes and phases of the junctions is also illustrated in our next example, as shown in Figure 24. In this figure there are now 4 junctions, two each at the points $x = 1/6$ and $x = 5/6$. Just as in the first example, the emitted power is low whenever the leading eigenvalue is positive; conversely, the emitted power can be quite large when the in-phase state is stable. We show in Figure 25 examples of the coherence properties of phase locked junctions. Figure 25(a) shows incoherent behavior, while Figures 25(b) and (c) show coherent behavior with low and high amplitudes, respectively. The example shown in Figure 25(b) emits very little power compared to that shown in Figure 25(c) because of its relatively low amplitude. Again, just because points (b) and (c) in Figure 24 are in the same region of in-phase stability does not mean that their emitted powers will be comparable.

Unfortunately examples of configurations that exhibit perfectly in-phase solutions are few and far between. We can achieve these solutions easily numerically, especially if we allow the junctions to be placed on top of each other (as they were in the example shown in Figure 24). By placing the junctions on top of each other we reduce the asymmetry in the problem. Of course, real world arrays cannot be produced in this manner, but the idea behind near resonant architectures follows the same principle. When the junctions are placed in clusters about the anti-nodes, the asymmetry of the system is (hopefully) reduced. This may allow nearly in-phase solutions to arise that, though not perfect, may still phase lock closely enough as to emit coherent power. It is just these types of architectures that

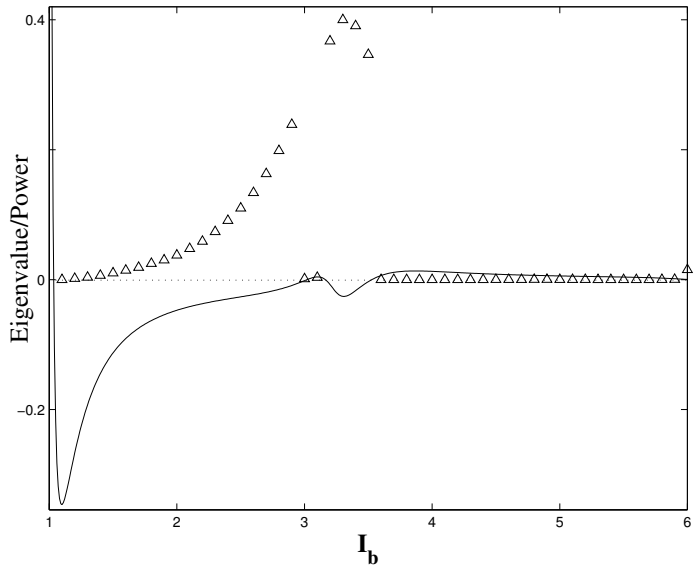

Figure 23: Plot of the largest non-zero eigenvalue (solid line) of Equation (83) and the emitted power (triangles) computed by direct integration (arbitrary units). Here there are two junctions at $x_j \in \{1/3, 2/3\}$, $k_{\max} = 15$, $\alpha = 2$ and $v = 1/\pi$.

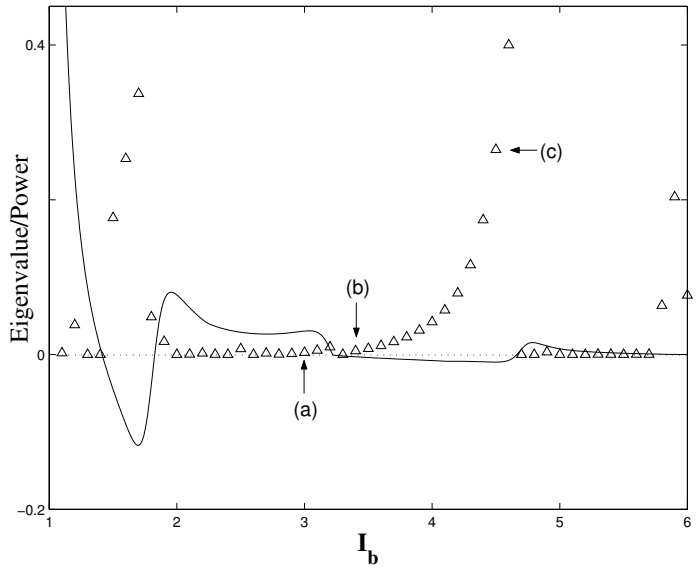

Figure 24: Plot of the largest non-zero eigenvalue (solid line) of Equation (83) and the emitted power (triangles) computed by direct integration (arbitrary units). Here there are four junctions, two each at $x_j \in \{1/6, 5/6\}$, $k_{\max} = 15$, $\alpha = 1$ and $v = 1/\pi$. Also shown (arrows) are the three trials plotted in Figure 25.

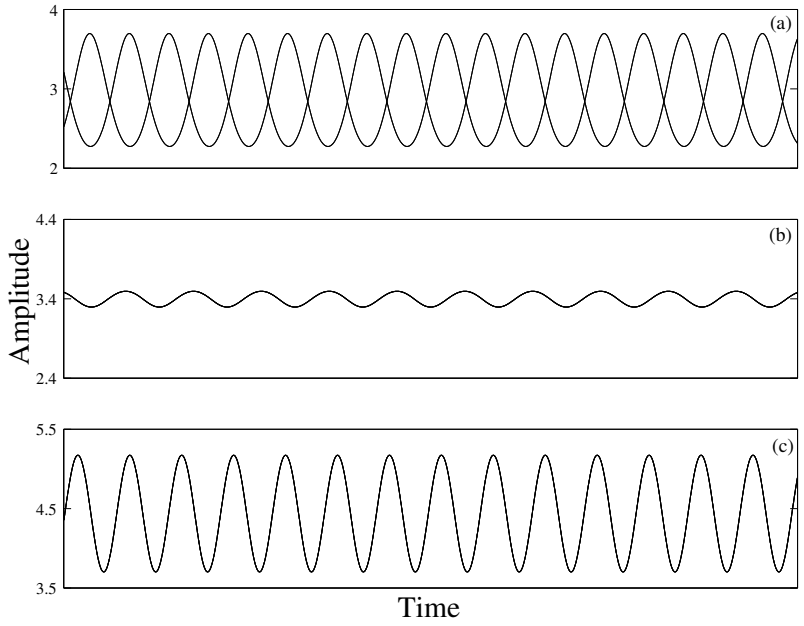

Figure 25: Comparison of the coherence and amplitude properties of phase locked junctions. Plotted are the three trials indicated in Figure 24. These trials are examples of (a) incoherent phase locking, (b) low and (c) high amplitude coherent phase locking.

we turn to next.

3.3 Near Resonant Behavior

We now take a look at the case of near resonant behavior and the dynamical consequences of spatially clustering the junctions, such as the configuration shown in Figure 13. We take for inspiration experiments [13, 41, 96] which use arrays intended to operate at a normal mode frequency of the transmission line. (By this we mean the modes in the absence of the junctions, corresponding to a particular Fourier index $k = k^\star$.) Numerically this situation is easily achieved. Figure 26 shows a plot of numerically obtained mode amplitudes of a configuration designed to select the fifth mode. This is done by placing six junctions in pairs centered on the three antinodes of similar parity of the fifth mode (i.e. at $x = 1/10$, $x = 1/2$ and $x = 9/10$, as shown in Figure 27). The system is then driven by a bias current that produces an operating frequency (recall $\omega = \sqrt{I_b^2 - 1}$) very close to the resonant frequency of the fifth mode. Clearly the fifth mode is dominant, as is also seen in the RMS current profile shown in Figure 27. In practice we have found that configurations that operate with

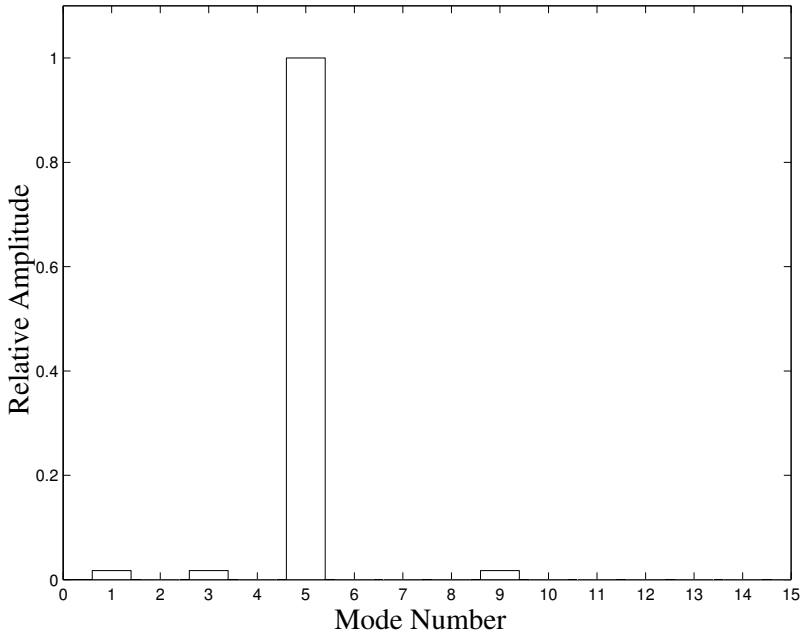

Figure 26: Histogram of the mode amplitudes (relative to the fifth) of a configuration designed to select the fifth mode. Here there are six junctions at $x_j \in \{1/10 \pm .01, 1/2 \pm .01, 9/10 \pm .01\}$. The bias current was chosen such that $\omega/\omega_5 \approx 1.01$, with $\alpha = 0.01$ and $k_{\max} = 15$. The values of the mode amplitudes were obtained from direct simulation of Equations (41) and (42).

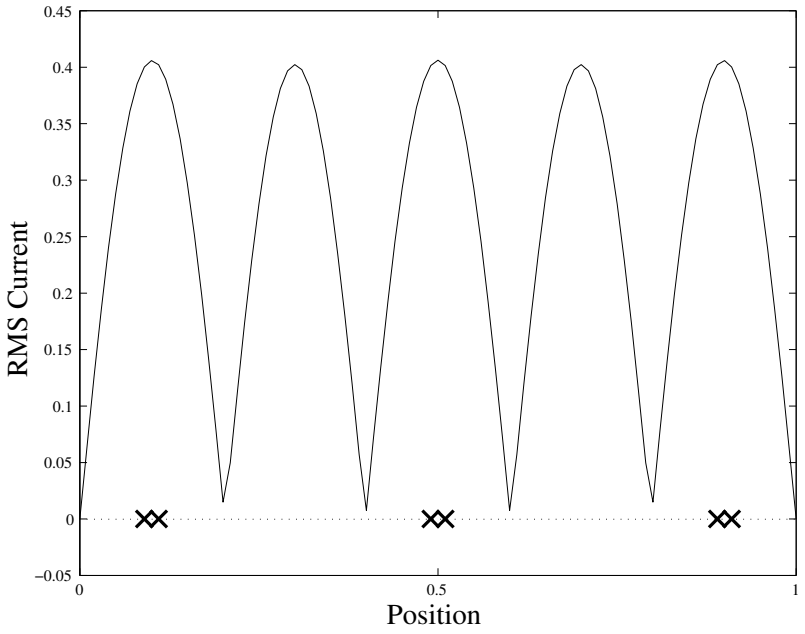

Figure 27: Plot of the RMS current profile of the example given in Figure 26. Also shown (crosses) are the positions of the six junctions.

a dominant mode are easy to construct provided the bias current is chosen properly and the junction configuration is commensurate with the desired mode profile.

We now wish to examine these near resonant architectures and their synchronization properties. Let's first see what we can conclude without specifying the junction positions $\{x_i\}$. Assume that the system is operating in a near resonant manner, such that the resonant mode is clearly dominant over the other modes. In this case we will approximate all sums over the current modes with just the term involving the resonant mode. In other words,

$$\sum_{k=1}^{k_{max}} f_k A_k \approx f_{k^\star} A_{k^\star}, \tag{84}$$

for any f_k, and where $k^\star$ is the Fourier index of the resonant current mode. Using this approximation, and writing $a_j = a_{jk^\star} = \sin(\pi k^\star x_j)$, Equation (78) reduces to:

$$\dot{\psi}_j = 1 + K \sum_{i=1}^{N} a_j a_i \sin(\psi_i - \psi_j + \theta), \tag{85}$$

where

$$K = \frac{2\alpha(I_\mathrm{b} - \omega)}{\sqrt{\left(\omega_{k^\star}^2 - \omega^2\right)^2 + \left(2\alpha\omega \sum_{q=1}^{N} a_q^2\right)^2}} \tag{86}$$

and

$$\theta = \tan^{-1}\left[\frac{2\alpha\omega \sum_{q=1}^{N} a_q^2}{\omega^2 - \omega_{k^\star}^2}\right]. \tag{87}$$

Equation (85) is significantly simpler than Equation (78). We now have explicit expressions for both the coupling constants and the phase shift. Also the phase shift matrix, Ω_{ji}, reduces to a constant phase shift θ. This last reduction is important because it makes the ensuing analysis tractable. It is still difficult to make analytic progress for arbitrary junction placements, but significant insight can be obtained from examining two simple cases.

First consider the case where the junctions are in one "group". By this we mean that the junctions have the property $a_j = a$ for all j. This condition is most obviously met when all of the (point-like) junctions are at the same spot, but also includes any arrangement where they occupy similar places along the waveform of the mode. In other words, the junctions can be at any position x that satisfies the equation $\sin(\pi k^\star x) = a$ for $x \in [0, 1]$. Figure 28 illustrates a possible configuration which satisfies this condition.

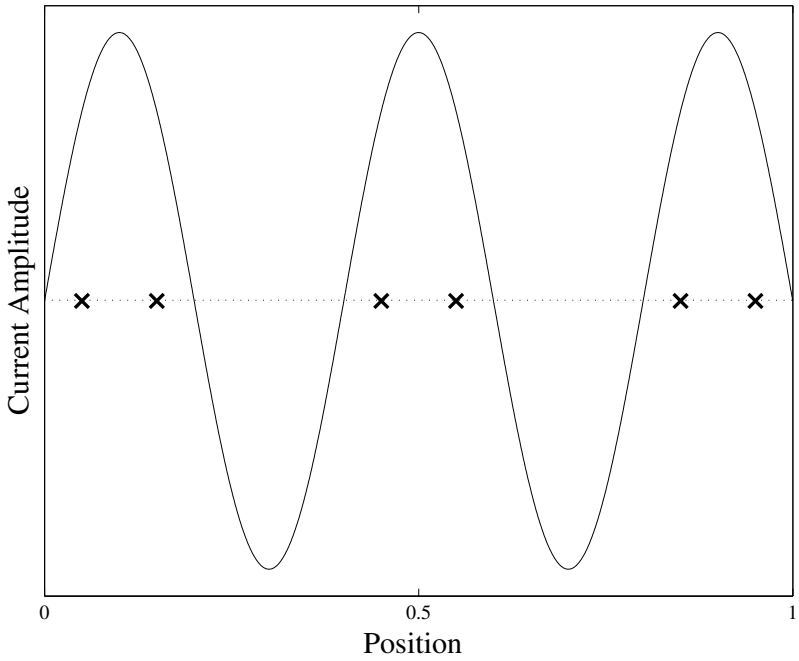

Figure 28: A configuration of junctions (denoted by crosses) which satisfies the "one group" condition. This is because the local current amplitude at each junction is the same.

Wan et al. [96] proposed a design which falls within this category. They used a so-called "quasilumped" circuit which places junctions uniformly along the wire such that the spacing between them was exactly one wavelength of the desired operating frequency. In this manner each junction was thought to see the same amplitude and phase of the AC current provided that the chosen mode is dominant.

When such a one group situation exists, Equation (85) becomes

$$\dot{\psi}_j = 1 + a^2 K \sum_{i=1}^{N} \sin(\psi_i - \psi_j + \theta). \tag{88}$$

This admits an in-phase state $\psi_j = \psi_0$ for all j. Introducing small perturbations $\psi_j = \psi_0 + \xi_j$, the linearized equations are diagonalized by switching to the coordinates $\sigma = \sum_{i=1}^{N} \xi_i$ and $\delta_j = \xi_{j+1} - \xi_j$, with result:

$$\dot{\sigma} = 0 \tag{89}$$

$$\dot{\delta}_j = -Na^2 K \cos(\theta)\delta_j. \tag{90}$$

So, there is one zero eigenvalue and $N-1$ degenerate eigenvalues given by:

$$\lambda = -Na^2 K \cos\theta. \tag{91}$$

Because I_b is strictly greater than ω, we see from Equation (86) that K is positive and the condition for linear stability reduces to

$$\cos\theta = \frac{\omega^2 - \omega_{k^\star}^2}{\sqrt{(\omega_{k^\star}^2 - \omega^2)^2 + (2\alpha\omega N a^2)^2}} > 0, \tag{92}$$

or, rather,

$$\omega > \omega_{k^\star}. \tag{93}$$

This result is nearly identical to the one for the RLC-loaded array studied in the lumped limit [53, 103]. There, the condition for in-phase stability is $\omega > \omega_0$ where $\omega = \sqrt{I_{\rm b}^2 - 1}$ and ω_0 is the natural frequency of the RLC load. We see that the resonant mode frequency $\omega_{k^\star}$ in the transmission line model (without load) plays the role of the load frequency ω_0 in the lumped model.

As a second example, consider the case of two groups. By this we mean that there are $n_1 + n_2 = N$ junctions such that n_1 junctions have the property $a_{jk^\star} = a_1$ and n_2 junctions have the property $a_{jk^\star} = a_2$. The clustered array depicted in Figure 13 is an example of a two group array. Provided the resonant mode is dominant, the local current amplitude seen by the junctions in Figure 13 will take on one of two values. The junctions placed at the anti-nodes will have a larger value of the local current amplitude than the junctions placed at their sides. Another possible configuration which satisfies the two group condition is the case when the junctions are placed at every anti-node of the resonant mode (so that they are 1/2 wavelength apart). The junctions at one parity of anti-node will experience a local current that is exactly opposite that of the junctions placed at the anti-nodes of the opposite parity.

To make the analysis cleaner, we rename the phase variables so that $\psi_j^{(p)}$ is the phase of the $j^{\rm th}$ junction in group p and $j \in [1, n_p]$. With this notation Equation (85) becomes

$$\dot{\psi}_j^{(p)} = 1 + K a_p \Big\{ a_1 \sum_{i=1}^{n_1} \sin(\psi_i^{(1)} - \psi_j^{(p)} + \theta) + a_2 \sum_{i=1}^{n_2} \sin(\psi_i^{(2)} - \psi_j^{(p)} + \theta) \Big\}. \tag{94}$$

Equation (94) admits solutions in which junctions within each group are in-phase and junctions between groups have a constant phase difference $\delta = \psi_j^{(1)} - \psi_i^{(2)}$. It is easy to show that when such a solution exists the phase difference between groups is given by

$$\delta = \sin^{-1}\left[\frac{n_1 a_1^2 - n_2 a_2^2}{a_1 a_2 K'}\sin\theta\right] - \Phi \tag{95}$$

where

$$K'\cos\Phi = N\cos\theta \qquad \text{and} \qquad \mathrm{K}'\sin\Phi = (\mathrm{n}_1 - \mathrm{n}_2)\sin\theta. \tag{96}$$

Note that there are phase locked solutions if and only if

$$\left|\frac{(n_1 a_1^2 - n_2 a_2^2)}{a_1 a_2 K'}\sin\theta\right| \leq 1 \tag{97}$$

or, in terms of the original parameters,

$$\left|\frac{2\alpha\omega(n_1^2 a_1^4 - n_2^2 a_2^4)}{a_1 a_2\sqrt{N^2(\omega_{k^\star}^2 - \omega^2)^2 + 4\alpha^2\omega^2(n_1 - n_2)^2(n_1 a_1^2 + n_2 a_2^2)^2}}\right| \leq 1. \tag{98}$$

With the knowledge that phase locked solutions exist and an explicit expression for the phase difference between the two groups, we can now examine the stability of such solutions. We let $\psi_i^{(1)} = \psi_0^{(1)} + x_i$ and $\psi_i^{(2)} = \psi_0^{(2)} + y_i$ where both x_i and y_i are small. Then, to first order, Equation (94) becomes

$$\dot{x}_j = K a_1^2\cos\theta\sum_{i=1}^{n_1}(x_i - x_j) + K a_1 a_2\cos(-\delta+\theta)\sum_{i=1}^{n_2}(y_i - x_j) \tag{99}$$

$$\dot{y}_j = K a_1 a_2\cos(\delta+\theta)\sum_{i=1}^{n_1}(x_i - y_j) + K a_2^2\cos\theta\sum_{i=1}^{n_2}(y_i - y_j). \tag{100}$$

This system is diagonalized by the coordinate transformations

$$\Gamma = \cos(\delta+\theta)\sum_{i=1}^{n_1} x_i + \cos(-\delta+\theta)\sum_{i=1}^{n_2} y_i \tag{101}$$

$$\Lambda = n_2\sum_{i=1}^{n_1} x_i - n_1\sum_{i=1}^{n_2} y_i \tag{102}$$

$$\delta_i^{(x)} = x_{i+1} - x_i \qquad i = 1,\ldots,n_1 - 1, \tag{103}$$

$$\delta_i^{(y)} = y_{i+1} - y_i \qquad i = 1,\ldots,n_2 - 1, \tag{104}$$

giving us

$$\dot{\Gamma} = 0 \tag{105}$$

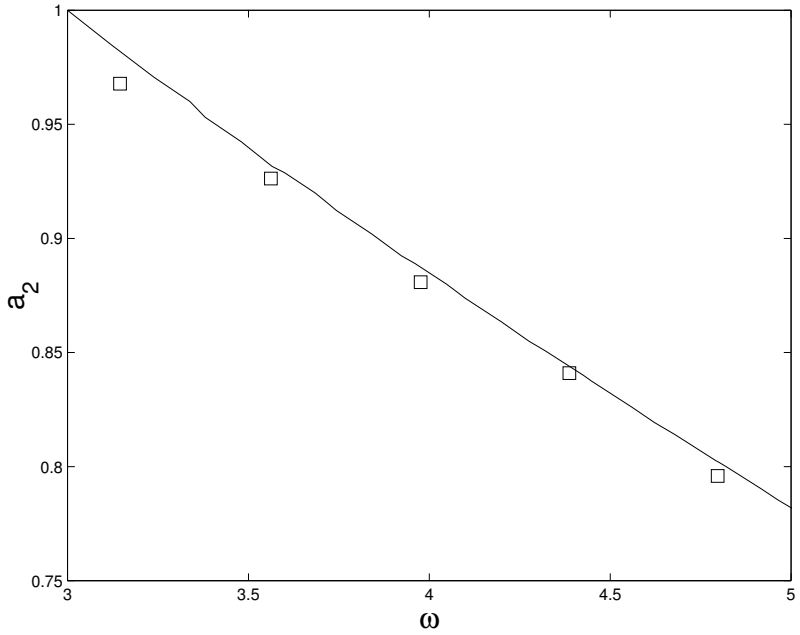

Figure 29: A plot of the critical value of a_2 above which phase locking becomes possible for the situation described in the text. The solid line is the theoretical prediction based on Equation (98). The squares are data taken from direct simulation of Equations (47) and (48), while constraining all Fourier modes to be zero except the resonant mode.

$$\dot{\Lambda} = -Ka_1a_2\Big[n_2\cos(-\delta+\theta)+n_1\cos(\delta+\theta)\Big]\Lambda \tag{106}$$

$$\dot{\delta}_i^{(x)} = -Ka_1\Big[n_1a_1\cos\theta+n_2a_2\cos(-\delta+\theta)\Big]\delta_i^{(x)} \tag{107}$$

$$\dot{\delta}_i^{(y)} = -Ka_2\Big[n_1a_1\cos(\delta+\theta)+n_2a_2\cos\theta)\Big]\delta_i^{(y)}. \tag{108}$$

Figure 29 shows a typical example of the accuracy of Equation (98). With $\alpha = 1$, $\omega_{k^\star} = 3$, $n_1 = n_2 = 4$ and $a_1 = 1$ we plot the critical value of a_2 above which phase locking becomes possible. This configuration consists of four junctions placed at (arbitrarily) positive anti-nodes, and four junctions placed at equivalent positions along the wave form of the resonant mode. Equation (98) predicts, and direct simulation of Equations (47) and (48) (keeping only the resonant mode) confirms, that if a_2 is smaller than the critical value then phase locked solutions will not exist. If, however, a_2 is larger than some critical value a_{2c}, then the phase locked solution will be stable for $\omega > \omega_{k^\star}$.

The physical principles involved in the locking condition can be better elucidated by taking a more concrete example. Consider the situation depicted in Figure 30. Here there

are nine junctions placed along the wire in three groups centered about the positive anti-nodes of the fifth mode. If we drive the system close to the resonant frequency of the fifth mode we expect that mode to dominate. But how big can each cluster of junctions be? In other words, if the positions of the junctions are given by $x_j \in \{.1, .1 \pm \delta x, .5, .5 \pm \delta x, .9, .9 \pm \delta x\}$, how big can δx be before phase locking is lost? A close up view of one of the three groups showing the spacing is given in Figure 31. This configuration falls into our "two group" classification because the three junctions at the anti-nodes are at equivalent positions along the mode, while the six at the sides are also at equivalent positions. Equation (98) predicts that if δx is small enough then phase locked solutions will exist, provided $\omega > \omega_5$. Figure 32 verifies that this is reasonably accurate. The sold line is the theoretical prediction of Equation (98) while the square are data obtained from direct simulation of Equations (47) and (48). Above the line δx is too large for phase locked solutions, while below the line stable phase locked solutions exist. Note that the simulation data given in Figure 32 was obtained while keeping the first 50 modes, not just the resonant mode. This shows that while Equation (98) was derived by keeping just the resonant mode, it still does a decent job in predicting the behavior of the full transmission line problem.

Several concepts can be gleaned from these examples, and from Equation (98). First, it is apparent from Equation (98) that the closer the groups are in both number and placement (with respect to the resonant mode) the better the chances are of locking. This follows from the fact that as $n_1 \to n_2$ and $a_1 \to a_2$ the numerator in Equation (98) vanishes. This may not be the only way to create phase locked solutions but it does have a physical appeal that mirrors experimental attempts to create high power arrays. Han et al. [41] proposed that arrays with clusters of junctions separated by whole wavelengths near the anti-nodes of the resonant mode should exhibit better phase locking properties than other configurations. They believed that since the junctions would see similar currents they would more easily phase lock. Our theory confirms this expectation, and Equation (98) can then tell us something about how large these clusters can be before phase locking becomes impossible.

Second, Equation (98) also implies that the closer the system is to resonance, the *harder* it is to achieve phase locking. This becomes easier to see if one considers the case where

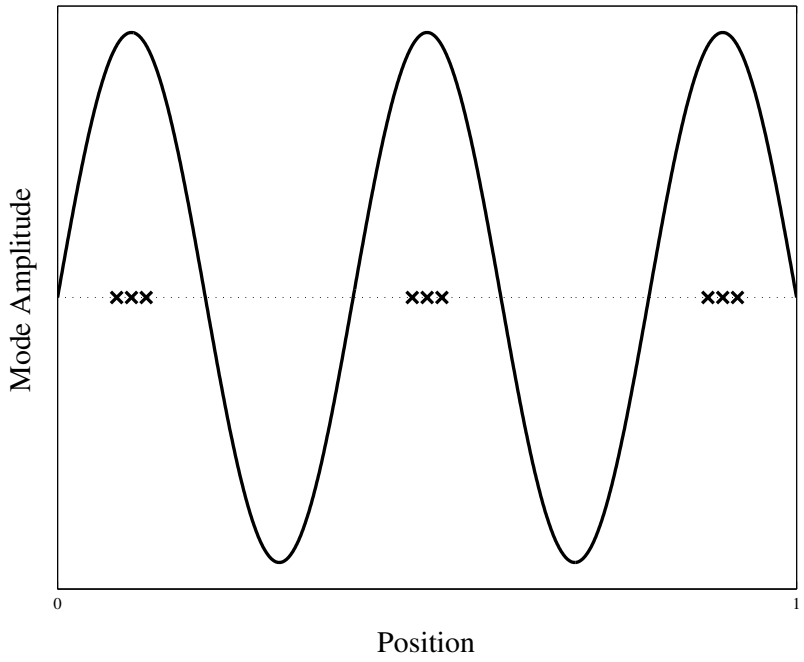

Figure 30: A configuration of junctions (denoted by crosses) designed to select the fifth current mode. Here there are nine junction. Three junctions are placed at the positive anti-nodes, while the remaining six are placed at to sides of the the first three. Also shown is the profile of the desired resonant mode.

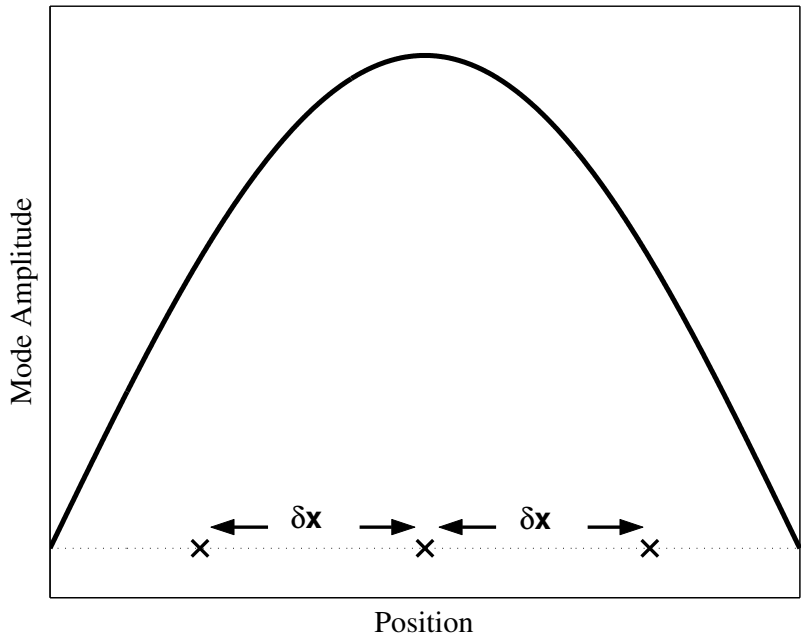

Figure 31: A close-up view of one of the groups shown in Figure 30. The total width of the group is $2\delta x$.

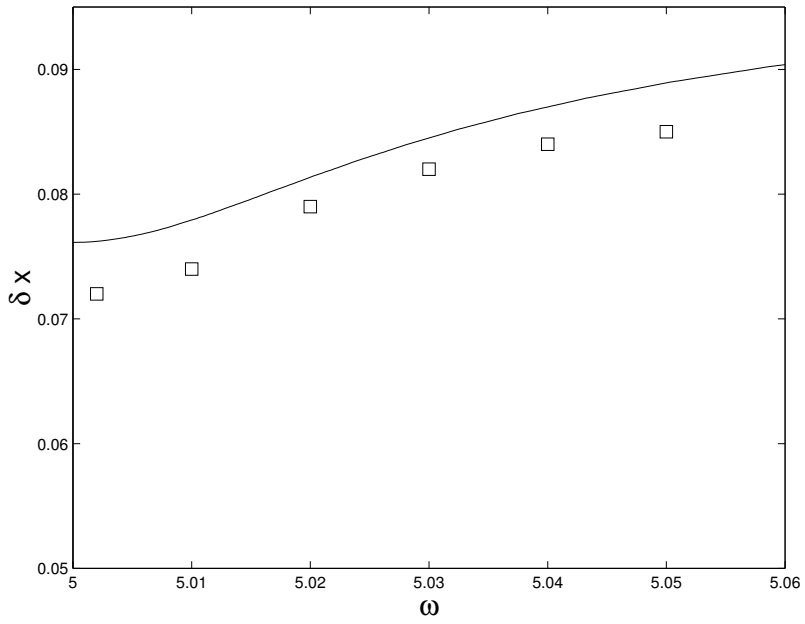

Figure 32: Comparison of the theoretical (solid line) and numerical (squares) values of the critical value of δx. Here there are nine junctions placed at $x_j \in \{.1, .1 \pm \delta x, .5, .5 \pm \delta x, .9, .9 \pm \delta x\}$, $\alpha = 0.01$, $v = 1/\pi$, and $k_{max} = 10$. Phase locked solutions are stable below the curve.

$n_1 = n_2$. Then Equation (98) becomes:

$$\left| \frac{\alpha\omega N(a_1^4 - a_2^4)}{2a_1 a_2(\omega_{k^\star}^2 - \omega^2)} \right| \leq 1. \tag{109}$$

The resonant denominator is now clearly seen in Equation (109). Note, also, that the total number of junctions affects the stability, but in a surprising way: the higher N, the lower the chance of locking. This puts a limit on the total number of junctions since δx must be finite. Consequently, arbitrarily large arrays designed with resonant architectures in mind will *not* be able to phase lock.

We can get a physical understanding of these conclusions, as follows. Consider the resonant mode as it is being driven by the junctions. Since it is a driven harmonic oscillator, the amplitude response of the mode is directly proportional to the number of junctions driving it, and inversely proportional to the difference of the squares of the driving frequency and the mode frequency. Next consider the junctions as they are being driven by the mode. Equation (47) tells us that near resonance each junction is driven by both the dc component (I_b) and a scaled oscillatory part, $I_{osc} \approx a_{ik^\star} A_{k^\star}(t)$). The difference in the driving for the

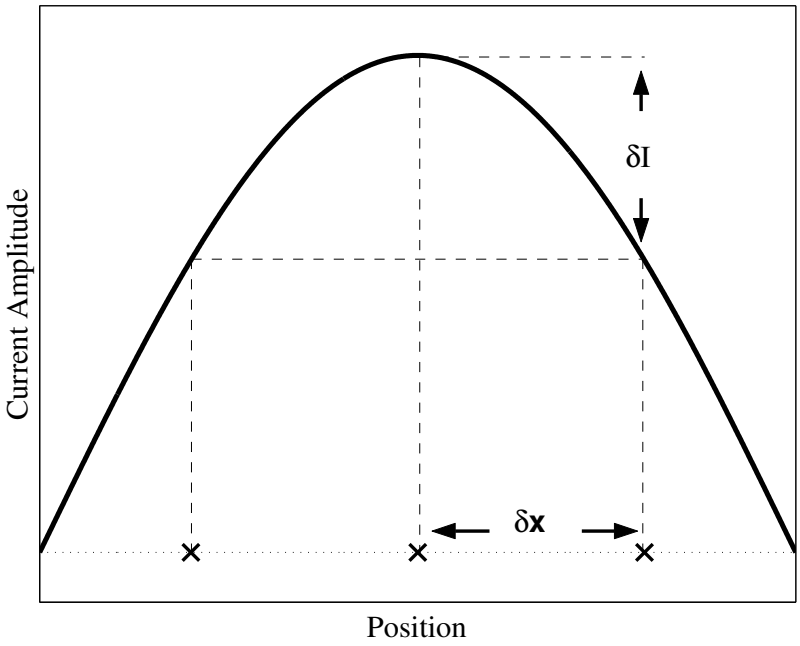

Figure 33: A close-up view of one of the groups shown in Figure 30. The spacing within the cluster causes a difference in the local current, δI, seen by the junctions

two groups is then determined by the difference in the local current, $\delta I \approx (a_1 - a_2)A_{k^\star}(t)$. Figure 33 illustrates this point. For phase locking to occur the amplitude of the driving difference cannot be too large. Therefore, the larger the amplitude of the mode the smaller the chance of phase locking. This is also the reason that tightly clustering the junctions increases the chance of phase locking: as $a_1 \to a_2$ the difference in the local current goes to zero.

Another configuration inspired by experiment [11, 41] that falls within the "two group" case consists of one junction placed at every anti-node of the resonant mode (so that they are separated by one half of a wavelength). First consider the case where $n_1 = n_2 = 1$ and $a_1 = -a_2 = 1$. This represents just two junctions – one placed at one anti-node, and the other placed at an anti-node of opposite polarity. An in-phase solution exists for this configuration and is stable for $\omega < \omega_{k^\star}$. This is the exact opposite of the stability condition found in the one group case and is due to the polarity reversal between the coupling constants of the two junctions. This would seem to suggest that placing junctions at every half wavelength instead of every wavelength is a plausible alternative to achieve

phase locking. However, if we allow for more than just two junctions things become more complicated.

Let $n_1 = n_2 > 1$ and $a_1 = -a_2 = 1$. Again this corresponds to the junctions placed at anti-nodes of opposing polarity, but now we allow for more than one of each kind. Equation (98) implies that a phase locked solution still exists, but from Equations (105-108) one finds that there are $N - 1$ zero eigenvalues and just a single non-zero eigenvalue. This implies neutral stability of these solutions, so that small perturbations away from them will not decay. Our simulations of Equations (47) and (48) confirm these predictions. We have found that phase locked solutions do indeed exist for $\omega < \omega_{k^\star}$ but are not stable to perturbations. Furthermore, when perturbed, phase locked solutions will remain phase locked but with a new value for the phase difference between the two groups. This situation is reminiscent of the the lumped circuit problem, where incoherent periodic solutions appear not individually but rather in continuous families [75, 97]; more generally such indeterminacy of relative phase between locked groups is typical of clustering behavior in lumped arrays [85]. This example casts serious doubt on the legitimacy of architectures that rely on half wavelength spacings. We do expect that such configurations will phase lock, but the indeterminacy of the phase difference means that output powers can be quite low.

Two experiments back up these conclusions. Bi et al. tried a configuration that consisted of two groups of junctions centered about two antinodes of opposite polarity [11]. They found that the output power was consist with their predictions. On the other hand, Booi and Benz tried a configuration that grouped multiple junctions about more than one antinode of each polarity [13]. They found that the output power was only about 12% of their theoretically predicted value. Note the difference between the two. Bi et al. placed the junctions about just two antinodes, which we found to have stable coherent solutions, while Booi and Benz placed the groups about many antinodes, which we found to have phase indeterminant solutions. Of course, we were able to do the analysis for just a single junction at each node, while both of these experiments were done with groups of junctions at each node. Booi and Benz attributed their discrepancy to the presence of a large impedance mismatch, but it is possible that a form of phase indeterminacy (similar to that described

above) also played a role.

3.4 Summary

At sufficiently high frequencies, the wire connecting the elements of any electronic oscillator array becomes an essential dynamical entity. But for Josephson arrays especially, this new wrinkle is an important consideration. The twin technological pressures of higher powers and higher frequencies inevitably push the design of the arrays out of the lumped-circuit limit. At the same time, new experimental strategies become available through manipulation of the spatial distribution of the junctions.

In this discussion, we considered perhaps the simplest non-trivial distributed architecture. The averaging scheme that we used led us to a set of equations structurally similar to those of a loaded lumped array with external load. These equations are valid for any spatial arrangement of the junctions, and thus serve as a natural springboard for investigations that compare and contrast various spatial distribution schemes. Unfortunately, the coupling constants in the averaged equations are pair dependent, and this is a major hurdle for further analysis. Nevertheless, we were able to make good progress for certain judiciously chosen examples.

In the case of near-resonant architectures we made a further reduction of the problem. The resonant case is especially revealing, and leads to significant physical insight into achieving attracting synchronized dynamics. The tighter the clusters, the more likely it is that phase locked solutions appear. Surprisingly, however, increasing the number of junctions within a cluster can be detrimental. The interplay between these two – which are the most fundamental properties of distributed architectures used in past experiments – is captured by the two-group model.

Further development of the theory of transmission line coupled arrays may have a broader significance than the problem we treated. For example, new schemes for power combining in nonlinear antenna arrays rely on transmission line coupling of semiconductor oscillators, as do related methods for beam scanning and beam shaping [104, 79, 46]. There are also hints that distributed arrays exhibit fundamentally different phenomena than their

lumped counterparts. For instance, Tsygankov and Wiesenfeld have found a novel type of synchronization in systems of nonlinear oscillators coupled through a transmission line [93]. In a phenomenon they call "dynamical dimerization", they have shown that in such systems pairs of oscillators can spontaneously synchronize and become dynamically independent of the other oscillators. This can happen when a pair of oscillators is separated by a half wavelength of a normal mode (not necessarily a resonant mode) of the transmission line. The work of Tsygankov and Wiesenfeld serves to underscore the complexity of the transmission line coupling scheme. The interplay among driving frequency, mode frequencies, and spatial positioning of the oscillators is just now beginning to be understood.

PART II

STOCHASTIC RESONANCE WITH WHITE AND COLORED NOISE

CHAPTER 4

STOCHASTIC RESONANCE

The reception of weak periodic signals is of utmost importance to today's communication and sensor technologies. In most cases the presence of background noise is a major problem because it degrades the quality of the signal reception. In some cases, however, the presence of background noise can actually improve the quality, and even allow the reception of signals that are undetectable in the absence of noise. One such phenomenon, known as stochastic resonance (SR), has been widely studied and is known to be present in a variety of systems.

4.1 A History of SR

The theory of SR was first proposed by Benzi et al. and independently by Nicolis to describe observed behavior in the Earth's climate over the past 700,000 years [3, 4, 5, 6, 76, 77]. Scientists noted that the amount of ice covering the Earth's surface was roughly periodic during this time span and had an average period of approximately 100,000 years. The only known planetary phenomenon that has that same period is the oscillation of the eccentricity of the Earth's orbit about the Sun caused by extra-planetary perturbations. Because these oscillations cause differences in the total amount of solar energy flux incident on the Earth's surface it is possible that they are the cause of the periodicity of ice coverage. When the flux is at a minimum, the ice coverage should be at a maximum, and vice-a-versa. However, the total variation in the incident flux is extremely small [4], while the corresponding changes in the ice coverage are drastic.

Though the Earth's climate is exceedingly complicated, Benzi et al. considered a very simple one-dimensional model they hoped could explain the phenomenon. They imagined the climate as a particle existing on a "climate potential" landscape and driven by external parameters such as the solar energy flux. An accurate climate potential function would have

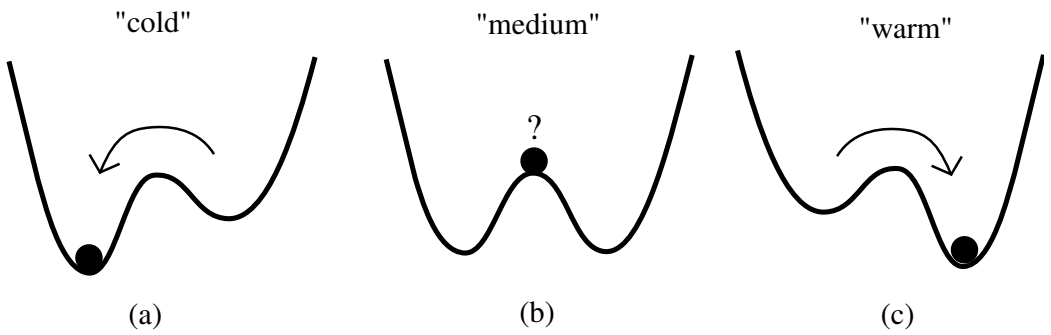

Figure 34: The one dimensional model of the climate consists of a rocked bi-stable potential. In (a) the solar energy flux is at a minimum, biasing the potential toward the "cold" state, while in (c) the flux is at a maximum, biasing the potential toward the "warm" state. In (b) the flux is normal, making either state equally probable.

many dimensions and parameters, but one can imagine projecting the dynamics onto a one-dimensional manifold describing the amount of ice coverage. The resulting one-dimensional potential should then be bi-stable – one minimum describing a cold (lots of ice) state, and the other a warm (small amounts of ice) state [23]. As the incident flux oscillates, the potential is rocked back and forth, but not to such a degree as to eliminate either of the two stable states (see Figure 34).

Notice that the model described above must be incomplete, because as stated, once the climate was in a particular state it would never leave that state. There must also be another mechanism that allows the state to jump from one state to the other. Benzi et al. proposed that this mechanism was noise. The actual source of the noise is not necessarily important, for it could be a number of things including fluctuations of the solar flux *not* due to eccentricity changes, atmospheric conditions such as global cloud coverage, or even the density of land vegetation. It is well known that a particle under the influence of noise can escape from a local minimum [44, 60], and Benzi et al. realized that these escapes would be more likely to occur when the potential was biased in the proper direction.

It is still debatable whether this description has any relevance to to the periodicity of the Earth's ice ages, but stochastic resonance is now also being used as one possible explanation for a similar phenomenon, Dansgaard-Oeschger events [58]. These events, which occur roughly every $1,500$ years, involve the sudden rise in temperatures in the North Atlantic.

Ganopolski and Rahmstorf have postulated that Atlantic currents can exist in two states, differing in the amount of fresh water that flows into the North Atlantic [33]. The changes in fresh water flux are enough to cause global temperature variations, and thereby explain Dansgaard-Oeschger events. The periodicity of the events is thought to have its roots in stochastic resonance [1, 34]. The currents are modulated at a period of roughly $1,500$ years, and are helped along by climatic noise.

The type of stochastic resonance described above is commonly referred to as two state stochastic resonance. The system can reside in either of two states. For the climate model these two states correspond to low and high levels of global ice coverage. This two state model has been studied to great extent, but it is only one form of stochastic resonance. Another type of stochastic resonance, typically called excitable SR or "stochastic resonance on a circle"[102], involves a slightly different system.

Excitable SR is similar to two state SR in that the potential landscape of the system has a minimum. Unlike two state stochastic resonance, however, excitable SR has just one minimum, called the ground state. Once the system is kicked out of the ground state it quickly, and deterministically, returns to the ground state. The time it takes to return to the ground state is called the refractory time, and is generally smaller than other time scales in the problem [102]. The result is that the output signal of the system becomes a spike train, instead of a telegraph-like signal characteristic of two state SR. The difference between the two is demonstrated in Figure 35. Figure 35(a) shows the output signal of an excitable system. Whenever the system is kicked out of the stable state it quickly returns, resulting in an output signal that is called a spike train. In contrast, Figure 35(b) shows the output signal of a two state system. Here, when the system is kicked out of one stable state it enters the other, where it remains until it is kicked out again. Excitable stochastic resonance has been used to model the reaction of periodically and noisily driven systems such as under-biased Josephson junctions, the Fitzhugh-Nagumo neuron models, semiconductor p-n junctions, and voltage dependent ion channels [9, 102].

The first experimental realization of SR was reported in 1983 by Fauve and Heslot [24]. They used a nonlinear circuit device called a Schmitt trigger that acts as a two state device.

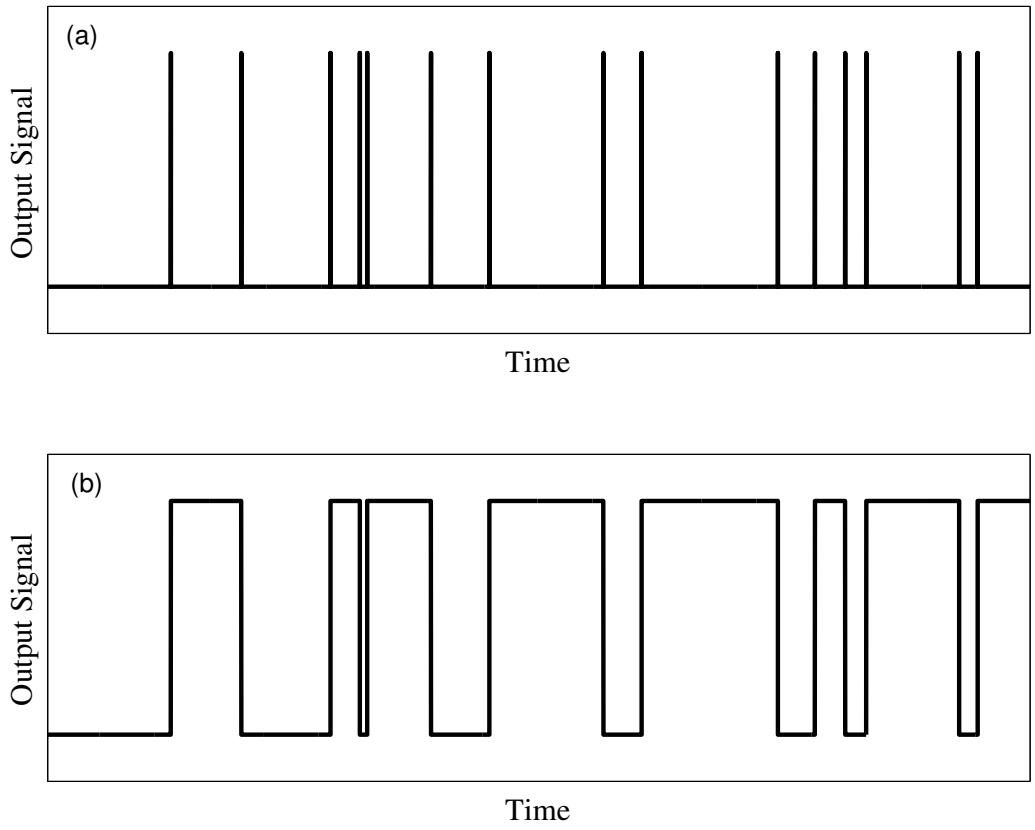

Figure 35: A comparison of idealized output signals from (a) an excitable system and (b) a two state system.

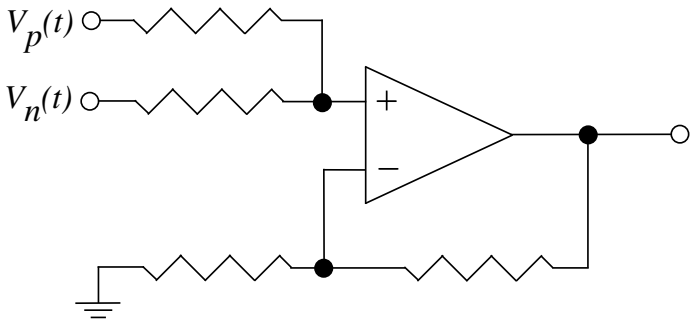

Figure 36: A schematic of a Schmitt trigger. The operational amplifier has a periodic input, $V_p(t)$, a noisy input, $V_n(t)$ and a feedback loop.

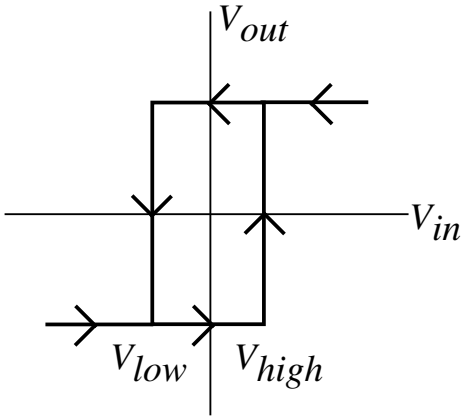

Figure 37: An idealized response diagram of a Schmitt trigger.

A schematic of a Schmitt trigger is shown in Figure 36. When in the low state, if the input voltage becomes higher than a threshold voltage, V_{high}, the trigger will switch to the high state. Once in the the high state, the input voltage must go lower than another threshold voltage, $V_{low} < V_{high}$, in order to go back to the low state. As a result, the corresponding response diagram shows a familiar loop characteristic of hysteresis (see Figure 37).

Fauve and Heslot prepared the Schmitt trigger so that the input voltage was a combination of a periodic and a noisy source. Without the noise the amplitude of the periodic voltage was too small to make the trigger switch from one state to the other. With the addition of the noisy voltage, however, the trigger did switch occasionally. They found that there existed a finite noise amplitude which maximized the output signal to noise ratio (SNR). This maximization of the SNR is now the characteristic most associated with

stochastic resonance.

Several years after the discovery of Fauve and Heslot stochastic resonance was also observed in a bistable ring laser system [71, 95], and in SQUIDS [48, 49]. Simulations [31] and theoretical work soon followed. In July of 1988 Fox submitted a paper containing an analysis combining time dependent perturbation theory with eigenfunction expansion of the underlying Fokker-Planck equation that described stochastic resonance in double well potentials [29]. Three months later McNamara and Wiesenfeld submitted their paper which described the double well system using a modulated rate theory approach [70]. Wiesenfeld et al. were later able to give a theoretical explanation of excitable stochastic resonance [102, 100] that used a rate theory technique similar to that used by Rice in his explanation of the "shot effect" [81].

One of the more intriguing aspects of stochastic resonance is its possible role in biological systems. The first suggestions of biological SR were made by Bulsara et al. in 1991 [14, 68], with their work on sensory neuron models. Several years later Douglass et al. published experimental evidence of SR in the mechanoreceptor hair cells of crayfish [22, 101, 102]. Subsequent work has shown SR to exist in a myriad of biological systems, including ion channels [8], cercal systems of crickets [63], and in mammalian cutaneous tissue [19]. Moss et al. have found that electrical noise improves the ability of paddlefish to find food [30, 83], and the search for SR in higher order functions has led to studies in vision [73], balance [80], respiration [50], and hearing [74].

In the following chapters we will examine stochastic resonance in several forms. First, we will attempt to derive a theory that can explain both two-state and excitable SR. The two different theories currently used to explain the two types of SR yield strikingly similar results. In one limit the predictions made by the two theories are identical. This begs the question of whether or not the two types of SR have a deeper connection, and we will examine this possibility.

In the last chapter we will look at SR with multiple sources of noise. In particular, we wish to investigate the properties of two state systems when a second, correlated noise source is added to a white noise source. We have found that this type of system can be

used to model signal transduction in the saccular hair cells of frogs [67]. We will show numerically that, as a function of the correlated noise strength, SR exists in such systems provided that the correlation time of the secondary noise is small enough. Two theories will be examined in an attempt to explain this phenomenon.

CHAPTER 5

A UNIFIED THEORY OF STOCHASTIC RESONANCE

The theory of McNamara and Wiesenfeld [70] which describes two state stochastic resonance uses a rate theory approach to explain the dynamics of the problem. The key to their model was in making a connection between the underlying continuous dynamics of a double well Langevin system to the discrete dynamics of a state model. This requires the probability distribution of the position variable to be sharply peaked near the minima of the double well. Additionally, all transitions between minima need to be relatively quick, so that once over the potential barrier the system quickly relaxes to a nearly stationary distribution around the new minimum. These assumptions led them to use two rates, corresponding to transitions back and forth between the two states. The sinusoidal drive of the signal modulates the two rates and if the drive is small enough, McNamara and Wiesenfeld showed that the rates are well approximated by

$$W_{\pm}(t) = \alpha \pm \epsilon \cos(\omega_s t + \phi), \tag{110}$$

where α and ϵ are constants and ω_s and ϕ are the frequency and initial phase of the drive. The $\pm$ refers to the present state of the system, either the "low" $(-)$ state or the "high" $(+)$, so that $W_{\pm}(t)$ is the rate *out* of the $\pm$ state.

Using Equation 110 McNamara and Wiesenfeld calculated that the signal to noise ratio, R, of the system is

$$R = \frac{\pi\epsilon^2}{2\alpha}\left\{1 - \frac{2\epsilon^2}{4\alpha^2 + \omega_s^2}\right\}^{-1}. \tag{111}$$

Now if we assume that the term in brackets is near unity (which can happen in either the high frequency or small signal limits) then Equation (111) reduces to

$$R \approx \frac{\pi\epsilon^2}{2\alpha}. \tag{112}$$

Equation (112) also happens to be the signal to noise ratio found by Wiesenfeld et al. in

their analysis of the excitable system [102][1]. In that system they assumed that the firing rate had the form

$$W_e = \alpha + \epsilon \cos(\omega_s t + \phi), \tag{113}$$

where, again, α and ϵ are constants and ω_s and ϕ are the frequency and initial phase of the sinusoidal drive, respectively. The constant α now represents the average rate at which the system fires, and the time dependent part is the correction to α due to the (adiabatic) sinusoidal drive. Just as in the two state system, the time scale of the drive must be slow compared to the average time between firings (i.e. $\alpha \gg \omega_s$).

In their derivation, Wiesenfeld et al. used a technique similar to that used by Rice in his analysis of the shot effect [81]. They assumed that the output current was zero everywhere except when the system fires, at which point there is a spike modelled by a Dirac delta function. Using just the statistics of this modulated Poisson process (as governed by Equation (113)) they were able to directly calculate the autocorrelation function without the use of a rate equation. This is in contrast to the theory of McNamara and Wiesenfeld for the two state system which relies on the solution of just such an ODE. Nevertheless, Wiesenfeld et al. were able to derive the SNR for the excitable system, $R_{e,W}$, with result

$$R_{e,W} = \frac{\pi \epsilon^2}{2\alpha}. \tag{114}$$

Both Equations (111) and (114) do well in predicting the SNR curves of their respective systems. This is shown in Figures 38 and 39. In these plots the rates α and ϵ are taken to be related to the escape rates out of a potential well, such that

$$\alpha = r_0 \exp\left[\frac{-\Delta U}{D}\right] \tag{115}$$

and

$$\epsilon = \frac{\eta r_0}{D} \exp\left[\frac{-\Delta U}{D}\right], \tag{116}$$

where r_0 and η are constants, ΔU is the barrier height, and D is the noise strength [70, 102]. The maxima in the SNR curves characteristic of stochastic resonance is clearly seen in both

[1] Actually, the result of Wiesenfeld et al. differs from our result by a factor of $\pi/2$ due to their choice of normalization of the Fourier transform of the cosine function. Also note that Equation (7) in their paper (Reference [102]) has an inadvertent factor 1/2 in it that is corrected later in the paper.

the two state (Figure 38) and one state (Figure 39) systems. For both low and high levels of the noise strength, D, the SNR is low. When the noise strength is is near $D \approx 130$ the SNR is maximized for both the one state and two state systems.

Some correspondence between the two systems could be expected given that they both rely on rate pictures of activated escape to cause an event (either a state switch or an excitation). But this begs the question of whether or not a single theory could encompass both phenomena.

In the present chapter we will provide a unified theory that is capable of describing both two state and excitable stochastic resonance. The method is similar to the rate theory used by McNamara and Wiesenfeld to describe two state stochastic resonance, but modified to work in two limits. In the first, the symmetric limit, the model will reduce to the two state theory of McNamara and Wiesenfeld, while in the second it models the excitable system studied by Wiesenfeld et al. This models does well in predicting the SNR curves of the symmetric limit and correctly predicts the behavior of intermediate regimes. In the excitable limit, however, the theory is off by a factor of two. We will examine this discrepancy in an effort to resolve the issue.

5.1 The Constrained Asymmetric Rate Model

One way of looking at the excitable limit is to imagine a two state process that has a finite rate of escape from one state and an infinite rate of escape from the other. In other words, once the system is kicked out of the $-$ state into the $+$ state it will immediately get kicked back into the $-$ state. This leads us to an asymmetric rate model of a two state system. Such a system has been studied before, in the context of asymmetric double well potentials. In looking at this model, Li [64] was led to a rate picture with rates of the form

$$W_{\pm}(t) = \alpha_{\pm} \pm \epsilon_{\pm} \cos(\omega_s t + \phi). \tag{117}$$

The asymmetry of the double well potential is evident in the constants $\alpha_{\pm}$ and $\epsilon_{\pm}$. Unfortunately the rate equation corresponding to the above rates is prohibitively difficult to solve. Li was able to get around this difficulty by assuming that $\epsilon_+ - \epsilon_-$ was small, corresponding to a slight asymmetry.

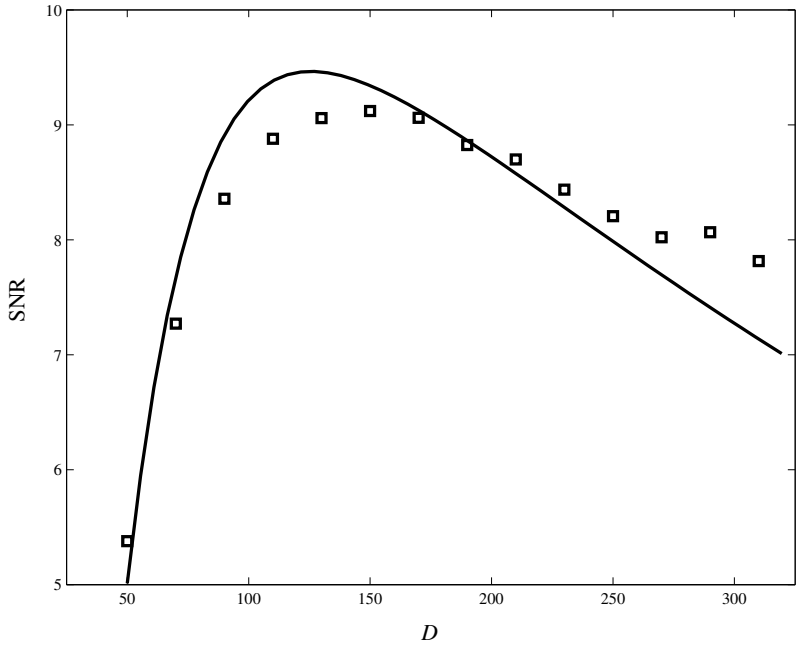

Figure 38: A plot of the SNR of a two state system. The solid line is the theoretical prediction of Equation (111) while the boxes are data taken from our numerical simulations of the two state process with $r_0 \approx 7.2$, $\eta \approx 45.2$ and $\Delta U = 256$.

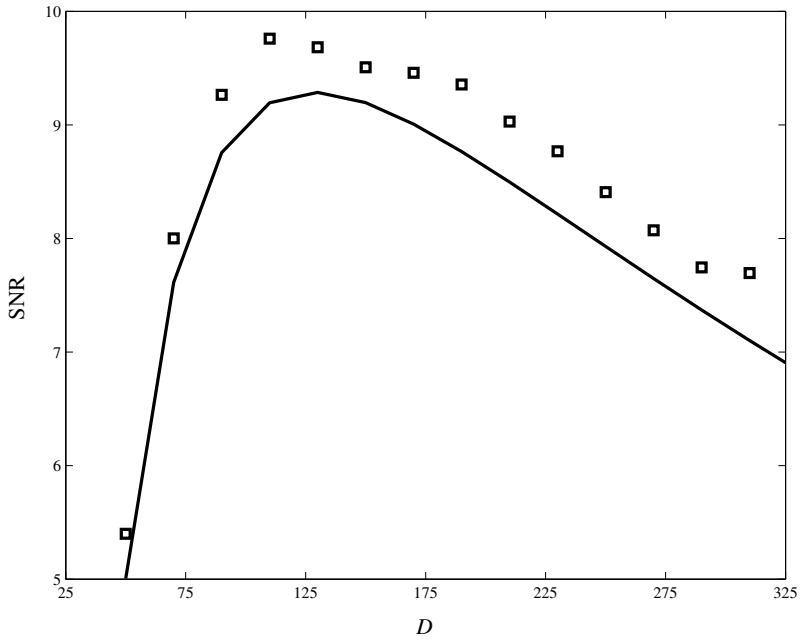

Figure 39: A plot of the SNR of a one state system. The solid line is the theoretical prediction of Equation (114) while the boxes are data taken from our numerical simulations of the one state process with $r_0 \approx 7.2$, $\eta \approx 45.2$ and $\Delta U = 256$.

If we are to use a two state picture to model the excitable system, however, the asymmetry will be infinitely large. The rate out of the lower state will remain finite, but the rate out of the high state will go to infinity (i.e. both α_+ and ϵ_+ will go to infinity, but α_- and ϵ_- will remain finite). The fact that $\alpha_+ - \alpha_- \to \infty$ poses no problem for the analysis, but the rate equation will be severely complicated since $\epsilon_+ - \epsilon_- \to \infty$.

Recall, though, that Equation (117) was the result of an examination of an underlying Langevin process within an asymmetric double well potential. If we wish to model an excitable system with a two state process, however, it would be wrong to constrain ourselves to an underlying double well potential. In particular, we note that when the system is in the + state we always want it to immediately relax back into the − state, no matter what the phase or amplitude of the drive is. This is accomplished simply by allowing α_+ to go to infinity while constraining ϵ_+/α_+ to be less than unity. In the excitable limit it does not matter what ϵ_+ is, since it will not affect the dynamics.

With this in mind, we begin our derivation by considering a modulated two state Markov process with states s_- and s_+. Instead of the rates given in Equation (117) we choose rates of the form

$$W_\pm(t) = \alpha_\pm \pm \epsilon \cos(\omega_s t + \phi), \tag{118}$$

where $\alpha_\pm$ are the bare (unmodulated) rates out of the states $s_\pm$, and ϵ, ω_s and ϕ are the amplitude, frequency and initial phase of the periodic signal, respectively. Notice that the amplitude of the drive is the same for both the s_- and s_+ states. This simple constraint will make the resulting rate equation solvable. This model, with the symmetric signal amplitudes, we call the "Constrained Asymmetric Rate Model" (CARM).

The probability of being in the state s_+ is governed by the ODE

$$\begin{aligned} \dot{P}_+ &= -W_+ P_+ + W_- P_- \\ &= -\sigma P_+ + \alpha_- - \epsilon \cos(\omega_s t + \phi), \end{aligned} \tag{119}$$

where $P_\pm$ is the probability of being in the $\pm$ state, $\sigma = \alpha_+ + \alpha_-$, and the second line follows from the fact that $P_- = 1 - P_+$. This has as its solution

$$P_+(t|s_0,t_0) = \exp\left[-\sigma|t-t_0|\right]\left\{\delta_{s_0,s_+} - \frac{\alpha_-}{\sigma} + \frac{\epsilon}{\sqrt{\sigma^2+\omega_s^2}}\sin(\omega_s t_0+\theta)\right\} + \frac{\alpha_-}{\sigma} - \frac{\epsilon}{\sqrt{\sigma^2+\omega_s^2}}\sin(\omega_s t+\theta), \quad (120)$$

where $P_+(t|s_0,t_0)$ is the probability of being in the state s_+ at time t given that the system was in state $s_0 \in \{s_+, s_-\}$ at time t_0, $\theta = \phi + \tan^{-1}(\sigma/\omega_s)$, and $\delta_{i,j}$ is the Kronecker delta function.

We define the output current of the system to be

$$I(t) = \begin{cases} A & \text{if in the } s_+ \text{ state} \\ 0 & \text{if in the } s_- \text{ state.} \end{cases} \quad (121)$$

The amplitude of the current, A, is arbitrary and carries the required units of the problem. It will set the strength of both the signal and noise of the output current, but will not appear in the signal to noise ratio. Even so, the current amplitude will become important when we make a detailed analysis of our theory in the excitable limit. For this reason, we will keep A as a free parameter until the need arises for us to specify it.

Equation (121) allows us to compute the autocorrelation function of the current,

$$\begin{aligned} \psi(\tau) &= \lim_{t_0\to\infty}\langle I(t+\tau)I(t)|s_0,t_0\rangle \\ &= \lim_{t_0\to\infty}\frac{A^2}{2\pi}\int_0^{2\pi} \mathrm{d}\phi\ P_+(t+\tau|s_+,t)P_+(t|s_0,t_0), \end{aligned} \quad (122)$$

where the brackets indicate averaging over both the probability distribution and the initial phase of the drive. Plugging in Equation (120) gives us

$$\psi(\tau) = \frac{A^2\alpha_-}{\sigma}\left[1-\frac{\alpha_-}{\sigma}\right]\exp\left(-\sigma|\tau|\right) - \frac{A^2\epsilon^2}{2(\sigma^2+\omega_s^2)}\exp\left(-\sigma|\tau|\right) + \frac{A^2\alpha_-^2}{\sigma^2} + \frac{A^2\epsilon^2}{2(\sigma^2+\omega_s^2)}\cos(\omega_s\tau). \quad (123)$$

The power spectrum can now be obtained by using the Wiener-Khinchin theorem [81]. Because the autocorrelation function is real and is an even function of τ, we may use the one-sided cosine transform. The result will be a combination of a Lorentzian due to the exponential and two Dirac delta functions. One of these delta functions is due to the cosine drive term, and the other is due to the constant term $A^2\alpha_-^2/\sigma^2$. This second delta function

represents dc power from the non zero average of the current, and is uninteresting. Ignoring this term the power spectrum is

$$\begin{aligned} S(\omega > 0) &= 4\int_0^\infty \mathrm{d}\tau\ \psi(\tau)\cos(\omega\tau) \\ &= \frac{4A^2\alpha_-}{\sigma^2+\omega^2}\left[1-\frac{\alpha_-}{\sigma}\right] - \frac{2A^2\epsilon^2\sigma}{(\sigma^2+\omega_s^2)(\sigma^2+\omega^2)} + \frac{\pi A^2\epsilon^2}{\sigma^2+\omega_s^2}\delta(\omega-\omega_s). \end{aligned} \quad (124)$$

Notice that the power spectrum is of the form

$$S(\omega) = N(\omega) + C\delta(\omega-\omega_s), \quad (125)$$

where $N(\omega)$ represents the broad band noise associated with the system, and $C\delta(\omega-\omega_s)$ is the power directly attributable to the coherent signal. The signal to noise ratio is defined to be ratio of the signal power to the noise power at the signal frequency

$$R = \frac{C}{N(\omega_s)}. \quad (126)$$

Reading these terms off from Equation (124) gives us

$$R = \pi\epsilon^2\left[4\alpha_-\left(1-\frac{\alpha_-}{\sigma}\right) - \frac{2\epsilon^2\sigma}{\sigma^2+\omega_s^2}\right]^{-1}. \quad (127)$$

We are now ready to take the two limits associated with the symmetric and excitable systems. In the symmetric limit both of the bare rates are equal, so that $\alpha_+ = \alpha_- = \alpha$ and $\sigma = 2\alpha$. In this limit the signal to noise ratio reduces to

$$R_s = \frac{\pi\epsilon^2}{2\alpha}\left\{1-\frac{2\epsilon^2}{4\alpha^2+\omega_s^2}\right\}^{-1}, \quad (128)$$

which is precisely the signal to noise ration given by McNamara and Wiesenfeld for the symmetric two-state case [70].

In the excitable limit we need the system to remain in the excited (s_+) state only instantaneously. This means that the rate out of the excited state should go to infinity. The result is a system that resides in the ground state (s_-) until being excited out. At that time the system immediately returns to the ground state. The current of such a system will be constant (at $I = 0$) except at a discrete number of points at which there is a spike. We obtain this limit by taking $\alpha_+ \to \infty$, meaning that once in the excited state the time

to relax back into the ground state will go to zero. In this limit the signal to noise ratio reduces to

$$R_e = \lim_{\alpha_+ \to \infty} R = \frac{\pi \epsilon^2}{4\alpha}, \tag{129}$$

where we have made the substitution $\alpha_- = \alpha$.

Equation 129 differs from the correct result given by Wiesenfeld et al. by a factor of 1/2 [102]. Their result, when suitably normalized, is given by

$$R_{e,W} = \frac{\pi \epsilon^2}{2\alpha}. \tag{130}$$

We will devote the next section to the examination of the connection between the excitable limit of the CARM and the "true" excitable system.

5.2 An Examination of the Excitable Limit Discrepancy

The first step in examining the discrepancy in the excitable limit of the Constrained Asymmetric Rate model involves specifying the amplitude of the output current. In the symmetric limit this amplitude is arbitrary, because it sets the strengths of both the noise and the signal components of the power spectrum. No matter what the value of the current amplitude, the signal to noise ratio of the symmetric limit will be unchanged. For physically plausible two state systems the current amplitude should remain finite. However, just the opposite is true for excitable systems. Because the system only spends an infinitesimal time in the excited state the current amplitude needs to be infinite for there to be a nonzero autocorrelation. In other words, given the discrete set of times $\{t_i\}$ for $i = -\infty, \ldots, -1, 0, 1, \ldots, \infty$ representing the times at which the system becomes excited, the current is

$$I_e(t) = \begin{cases} H\delta(t - t_i) & \text{if } t = t_i \ \ \forall\ i \\ 0 & \text{otherwise.} \end{cases} \tag{131}$$

The strength of the delta function, H, is now the arbitrary constant that sets the strengths of the noise and signal in the power spectrum, analogous to A in the symmetric limit.

Our task is to find the proper value of A such that in the limit $\alpha_+ \to \infty$ Equation (121) becomes Equation (131). In other words, as the rate out of the excited state goes to infinity the square waves of the current must become delta functions. This necessitates an infinite

value of A, with appropriate behavior as α_+ gets large. To this end, let us make use of the rectangular function defined by

$$\text{rect}(t) = \begin{cases} 0 & \text{if } |t| > 1/2 \\ 1/2 & \text{if } |t| = 1/2 \\ 1 & \text{if } |t| < 1/2. \end{cases} \tag{132}$$

The rectangular function has zero value outside of a region of length 1 centered about the origin in which it has unit value. Also, any integral spanning the support ($[-1/2, 1/2]$) of rect(t) has unit value (i.e. the area under the curve is one). These features lead to the relation

$$\lim_{a\to\infty} a \cdot \text{rect}(at) = \delta(t). \tag{133}$$

Without loss of generality, assume that the set $\{t_i\}$ of excitation times also represents the times of the midpoints of the square wave excitations. As depicted in Figure 40, the height of each square wave is A while the *average* width is $1/\alpha_+$. Therefore we may write the i^{th} square wave of the current as

$$I_i(t) = A \cdot \text{rect}\left[\alpha_+(t - t_i)\right]. \tag{134}$$

Furthermore, assume that the current amplitude increases linearly with α_+, so that $A = C\alpha_+$. Then

$$\lim_{\alpha_+\to\infty} I_i(t) = \lim_{\alpha_+\to\infty} C\alpha_+ \cdot \text{rect}\left[\alpha_+(t - t_i)\right] = C\delta(t - t_i). \tag{135}$$

Comparing Equation (135) to Equation (131) we see that $C = H$, meaning that the correct current amplitude to use is $A = H\alpha_+$.

We can now plug the new current amplitude into the result for the autocorrelation of the CARM, Equation (123), giving us

$$\begin{aligned} \psi(\tau) &= \frac{H^2\alpha_+^2\alpha_-}{\sigma}\left[1 - \frac{\alpha_-}{\sigma}\right]\exp\left(-\sigma|\tau|\right) - \frac{H^2\alpha_+^2\epsilon^2}{2(\sigma^2 + \omega_s^2)}\exp\left(-\sigma|\tau|\right) \\ &\quad + \frac{H^2\alpha_+^2\alpha_-^2}{\sigma^2} + \frac{H^2\alpha_+^2\epsilon^2}{2(\sigma^2 + \omega_s^2)}\cos(\omega_s\tau). \end{aligned} \tag{136}$$

Recall that $\sigma = \alpha_- + \alpha_+$, so that when we take the limit $\alpha_+ \to \infty$ we must take this into account. Also note that for finite x

$$\lim_{\alpha_+\to\infty} \frac{\alpha_+^2}{\alpha_+^2 + x} = 1, \tag{137}$$

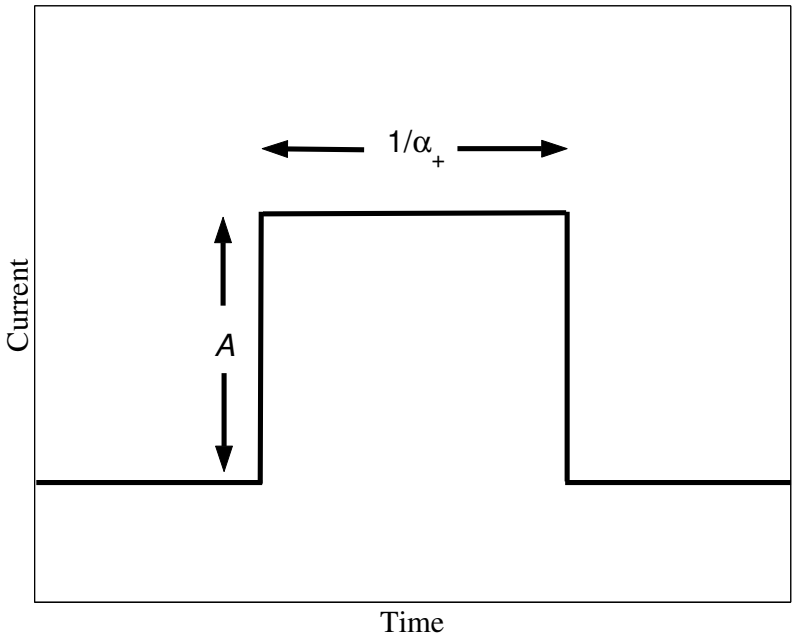

Figure 40: One excitation pulse of the current given in Equation (121). The pulse has an average width $1/\alpha_+$ and a height A.

and

$$\lim_{\alpha_+\to\infty} \exp\left[-\sigma|\tau|\right] = 0, \tag{138}$$

meaning that all terms of the form $[\alpha_+^2/(\alpha_+^2 + x)]\exp\left[-\sigma|\tau|\right]$ vanish in the limit $\alpha_+ \to \infty$. This leaves us with

$$\lim_{\alpha_+\to\infty} \psi(\tau) = \lim_{\alpha_+\to\infty} \frac{H^2\alpha_+^2\alpha_-}{\sigma} \exp\left(-\sigma|\tau|\right) + H^2\alpha_-^2 + \frac{1}{2}H^2\epsilon^2\cos(\omega_s\tau). \tag{139}$$

The remaining limit can be evaluated by noticing

$$\begin{aligned}
\lim_{a\to\infty} \frac{a^2}{a+c} \exp\left[-(a+c)|\tau|\right] &= \lim_{a\to\infty} \left[\frac{(a+c)^2}{a+c} - \frac{2ac+c^2}{a+c}\right] \exp\left[-(a+c)|\tau|\right] && (140)\\
&= \lim_{a\to\infty} (a+c) \exp\left[-(a+c)|\tau|\right] && (141)\\
&= \lim_{b\to\infty} b \exp\left[-b|\tau|\right] && (142)\\
&= 2\delta(\tau). && (143)
\end{aligned}$$

This means that, in the excitable limit, the autocorrelation function for the CARM is

$$\psi_e(\tau) = 2H^2\alpha_-\delta(\tau) + H^2\alpha_-^2 + \frac{1}{2}H^2\epsilon^2\cos(\omega_s\tau). \tag{144}$$

Equation (144) is nearly identical to the autocorrelation function given by Wiesenfeld et al. in their derivation of the true excitable system. That autocorrelation is

$$\psi_{e,W}(\tau) = H^2\alpha_-\delta(\tau) + H^2\alpha_-^2 + \frac{1}{2}H^2\epsilon^2\cos(\omega_s\tau). \tag{145}$$

Now we can see exactly where the problem lies. The coefficient of the $\delta(\tau)$ term in the CARM autocorrelation has an extra factor of two. This term is directly responsible for the broadband background noise of the system, since the power spectrum is given by

$$\begin{aligned} S_e(\omega > 0) &= 4\int_0^\infty \mathrm{d}\tau\ \psi_e(\tau)\cos(\omega\tau) && (146)\\ &= 4H^2\alpha_- + \pi H^2\epsilon^2\delta(\omega-\omega_s), && (147)\end{aligned}$$

where the dc component of the noise resulting from the constant term in Equation (144) has been ignored. The first term in Equation (147) is the noise attributable to the $\delta(\tau)$ term in Equation (144) while the $\delta(\omega-\omega_s)$ term represents the coherent power in the sinusoidal signal. Again, Equation (147) differs from the result of Wiesenfeld et al. by a factor of two in the background noise. The correct power spectrum for their result is

$$S_{e,W}(\omega > 0) = 2H^2\alpha_- + \pi H^2\epsilon^2\delta(\omega-\omega_s). \tag{148}$$

Apparently the CARM gets the coherent signal term correct, but overestimates the noise.

We have numerically checked both theories, and both do well in describing their respective systems. Figures 41-43 illustrate this point. In Figures 41 and 42 we have let $\alpha_+ = n\alpha_-$ and $A = \alpha_+$. In the truly symmetric case ($n = 1$) we recover the result of McNamara and Wiesenfeld (Figure 41). If we turn on the asymmetry by allowing $n > 1$ the predictions made by the CARM are still excellent, even when $n = 1000$ (Figure 42). Note that when $n = 1000$, however, there seems to be a systematic error of about 10%. It is yet unknown if this error is a true difference, or whether it is due to the numerical difficulties of integrating a system with such a discrepancy in time scales. In the truly excitable limit, the theory of Wiesenfeld et al. does a near perfect job (Figure 43).

Notice that as the asymmetry is turned on in the CARM, the power spectrum begins to flatten out to a constant value. This happens because the corner frequency of the

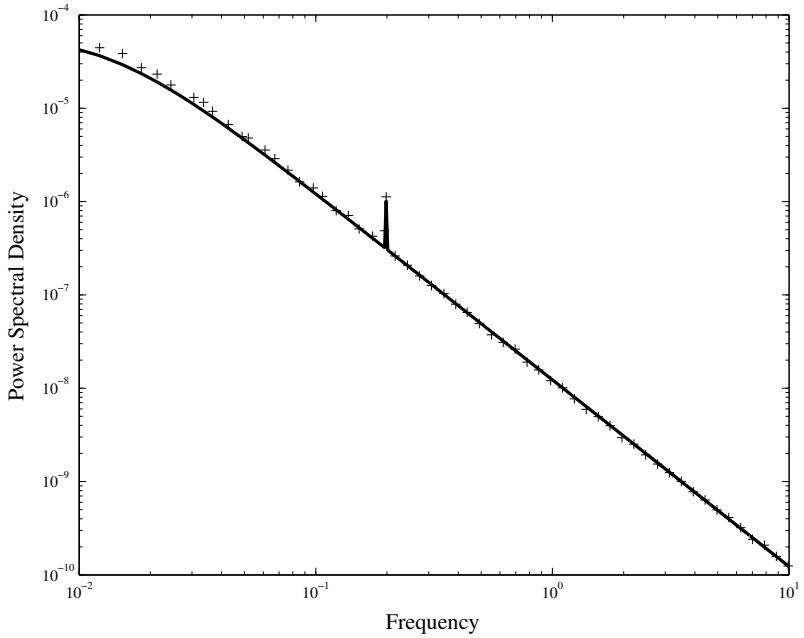

Figure 41: The power spectrum of the symmetric two state model. The solid line is the theoretical prediction of the CARM, while the crosses are numerical data taken from simulation of the two state process. Here $\alpha_- \approx 0.043$, $\epsilon \approx 0.039$, $\omega_s \approx 1.23$ and $n = 1$.

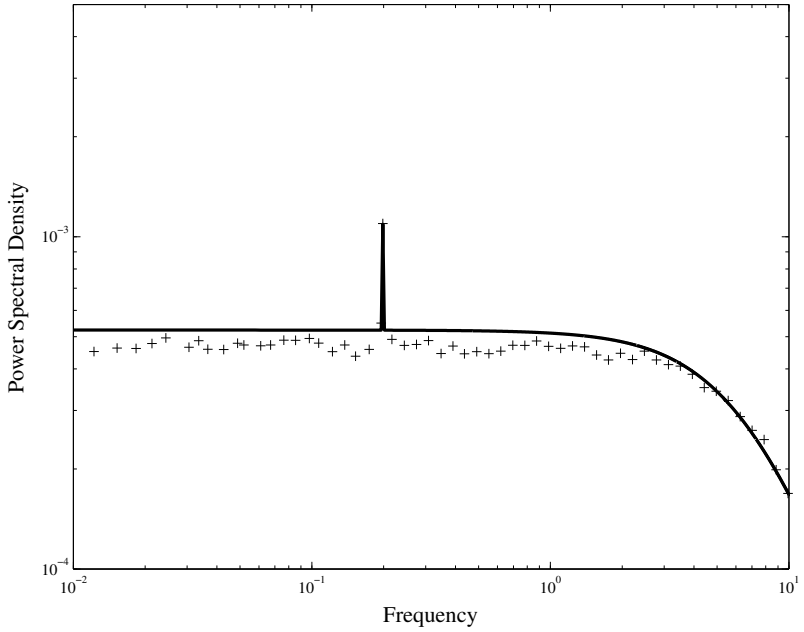

Figure 42: The power spectrum of an asymmetric two state model. The solid line is the theoretical prediction of the CARM, while the crosses are numerical data taken from simulation of the two state process. Here $\alpha_- \approx 0.043$, $\epsilon \approx 0.039$, $\omega_s \approx 1.23$ and $n = 1000$.

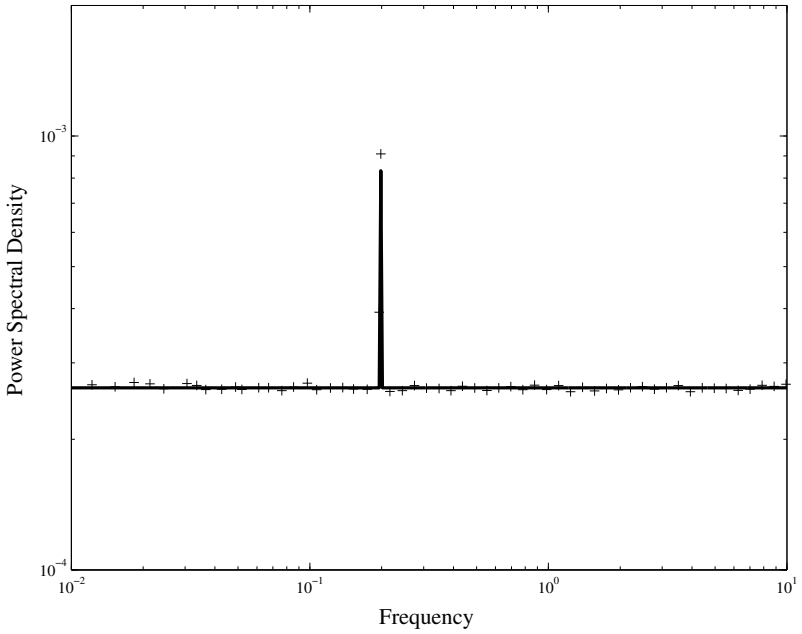

Figure 43: The power spectrum of the one state model. The solid line is the theoretical prediction of the Wiesenfeld et al., while the crosses are numerical data taken from simulation of the one state process. Here $\alpha_- \approx 0.043$, $\epsilon \approx 0.039$, $\omega_s \approx 1.23$.

Lorentzian shaped spectrum of the noise moves to higher frequencies as the system becomes more asymmetric. However, in the limit $n \to \infty$ the CARM converges to a value of the background noise that is twice as large as the true excitable limit. This is illustrated in Figure 44.

The CARM does an excellent job in describing two state systems with finite asymmetries in the base rates, and correctly predicts the SNR of the symmetric system. It was our hope, however, that this model would allow for a limit capable of correctly describing excitable systems. Unfortunately this is not the case, and the reasons for it are still unknown to us. The result the CARM gives for the SNR of the excitable limit does have the same functional form as that given by Wiesenfeld et al. (differing only by a factor of 2) and this is tantalizing evidence that gives us hope that a two state model of excitable systems can still be found.

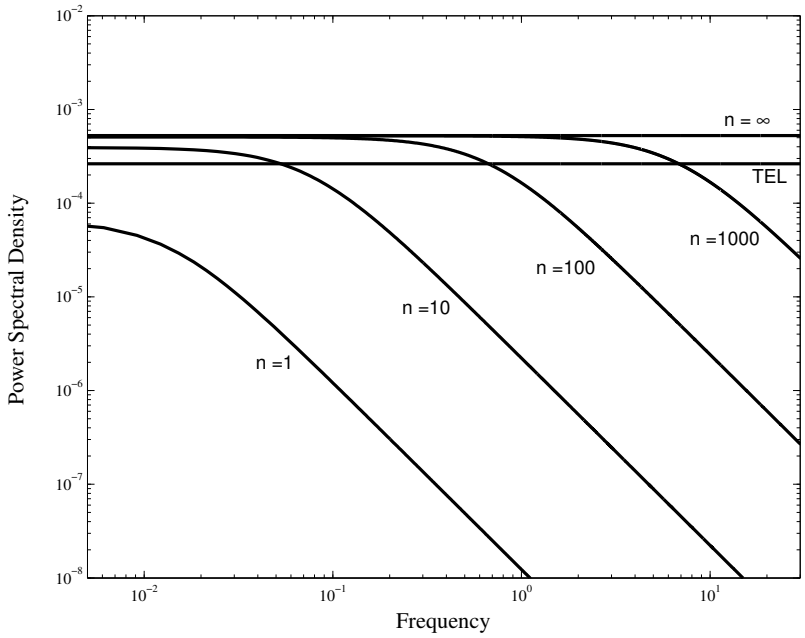

Figure 44: The theoretical noise power spectra predicted by the CARM for $n = 1, 10, 100, 1000$ and ∞. Also plotted is the correct prediction of Wiesenfeld et al. for the true excitable limit (TEL).

CHAPTER 6

STOCHASTIC RESONANCE WITH WHITE AND COLORED NOISE

One of the main features common to most work on stochastic resonance is the "whiteness" of the noise term. In other words, the autocorrelation function of the noise is generally a Dirac delta function, giving the noise infinite variance but zero correlation time. Certain theoretical considerations make this approximation attractive, since analytic progress in systems containing correlated noise sources is considerably more difficult than in those with uncorrelated sources. Real world noise sources are not purely uncorrelated, but the argument can often be made that the correlation time of the noise source is much smaller than all other time scales in the problem, rendering the noise effectively white.

There are times when the finite correlation time of the noise source must be taken into account. One can then ask: how does colored noise affect stochastic resonance? This question was taken up first numerically by Gammaitoni et al. who found that the effectiveness of SR *decreased* with increasing correlation time [32]. This finding was backed up theoretically by Hänggi et al. [43]. They predicted that the effectiveness of SR should decrease with increasing correlation time for over-damped bistable systems, but also that it can increase for systems with non-negligible inertia. Experimental work has also been done on an optical bistable system that shows a clear decrease in the peak SNR values for increasing correlation times [72].

Various forms of noise sources have now been studied in the context of stochastic resonance. For instance the noise need not be purely additive [7, 56, 105], nor does it need to be Gaussian [36, 59, 82]. In the present chapter we will explore stochastic resonance in bistable systems in the presence of two independent additive noise sources. One place where we have encountered this situation is in the hair cells of vertebrates [67]. Hair cells play a major role in the auditory system in that they convert mechanical energy into the

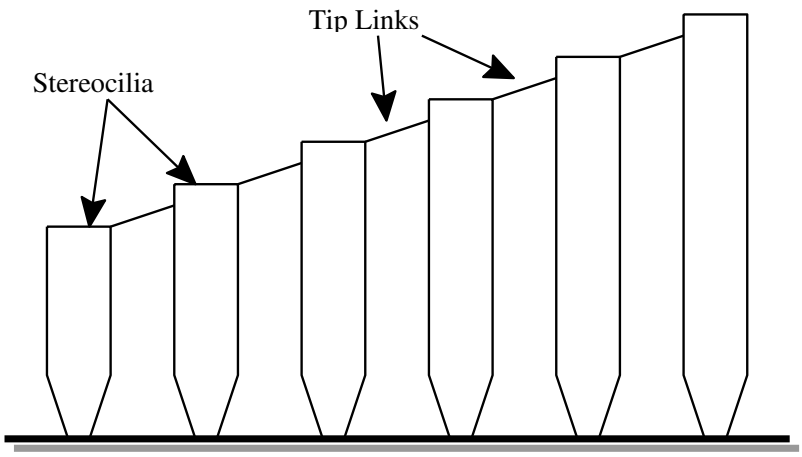

Figure 45: A single row of stereocilia ("rods"). The rods increase in height along the row and are connected by an elastic tip link.

electrical impulses that are sent to the brain. Experiments have now shown that vertebrate hair cells exhibit stochastic resonance [47, 52, 54, 55]. Very little theoretical work has been done on this type of system, however, and in the present chapter we begin to explore one aspect of such a system, namely the effect of multiple noise sources.

Mammalian auditory hair cells reside in the organ of Corti [66] beneath the tectorial membrane. There are two types of hair cells, inner hair cells and outer hair cells. The motile outer hair cells appear to be attached to the tectorial membrane and are thought to actively amplify and refine the local motion of the organ of Corti. In contrast, the inner hair cells are detached from the tectorial membrane. Their motion is directly attributable to the ambient fluid, and therefore they could undergo significant Brownian motion [51, 54, 55, 66].

At the top of each hair cell resides a hair bundle comprised of stereocilia. The hair bundle reacts to the motion of the ambient fluid by tilting in one direction or another. This tilting forces open gates near the tops of the stereocilia that allow ions in the fluid to flow into ion channels that lead to the neural auditory system. The ions are generally small monovalent cations (Li^+, Na^+, K^+, Rb^+, Cs^+ and NH_4^+ are the most common) but larger ions such as choline, tetramethylammonium and tetraethylammonium can also pass through the gates [51].

The hair bundles themselves usually contain tens of stereocilia arranged into a two

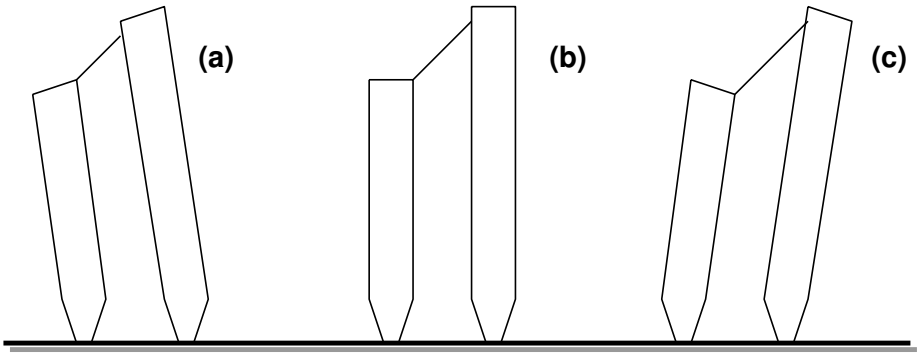

Figure 46: A schematic of two rods and their associated tip link as they are (a) closed-biased, (b) unbiased and (c) open-biased.

dimensional array. Along the rows of the array the tops of each stereocilium (sometimes called a "rod") are connected by an elastic tip link (see Figure 45). When stretched, this tip link pulls on the ion channel gate, biasing it either to the open or closed position (see Figure 46). Once the gate is open, ions in the surrounding fluid pass through the gate and down the neural pathways, as shown in Figure 47.

Our recent work [67] has modelled hair cells as a coupled system of bistable potentials driven by a sinusoidal drive (the signal) and two sources of noise, one white and the other colored. The bistable potential corresponds to the gate dynamics, since each gate can stably reside in either the open or closed states. The white noise source is due to impacts sustained by the gate directly from the ambient Brownian fluid, while the colored noise and sinusoidal drive are attributable to the motion of the rod. The secondary noise is colored because its affects on the gates are indirect, since they are filtered through the other degrees of freedom. Though the noise on the rods is initially white, the filtering process takes out the high frequency content, so that each gate feels a colored noise source. In the uncoupled limit, we model the gate dynamics (in the over damped limit) with a symmetric quartic bistable potential with a sinusoidal drive and two sources of additive noise, resulting in an equation of the form

$$\dot{x} = ax - bx^3 + A\cos(\omega_s t + \phi) + \xi_w(t) + \xi_c(t), \tag{149}$$

where A, ω_s and ϕ are the amplitude, frequency and initial phase of the drive, respectively;

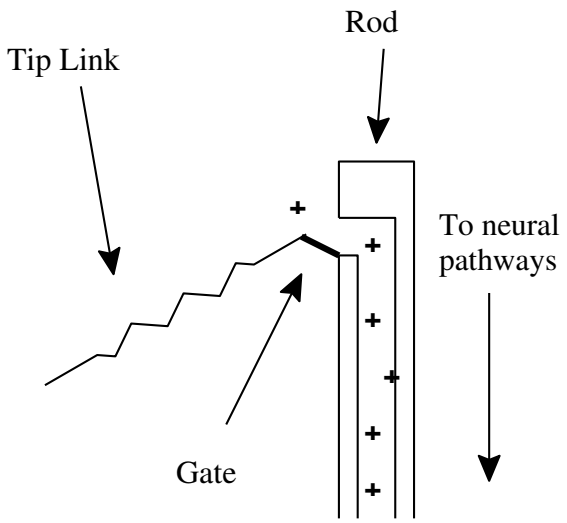

Figure 47: A close-up view of the gate mechanism at the top of a rod. When the gate is open (as shown) ions are allowed to flow into the ion channel and down into the neural pathways.

a and b are constants; and $\xi_w(t)$ and $\xi_c(t)$ are the white and colored noise sources, with the correlations

$$\langle \xi_w(t) \rangle = \langle \xi_c(t) \rangle = 0, \tag{150}$$

$$\left\langle \xi_w(t)\xi_w(t') \right\rangle = 2D_w\delta(t-t'), \tag{151}$$

$$\left\langle \xi_c(t)\xi_c(t') \right\rangle = \frac{D_c}{\tau_c} \exp\left[-\frac{|t-t'|}{\tau_c} \right], \tag{152}$$

and

$$\left\langle \xi_w(t)\xi_c(t') \right\rangle = 0, \tag{153}$$

where D_w and D_c are the white and colored noise strengths, respectively, and τ_c is the correlation time of the colored noise.

For the remainder of this chapter we will examine Equation (149). Without the colored noise term it is identical to the system studied by, for example, McNamara and Wiesenfeld in their study of stochastic resonance in bistable systems [70] and by Fox [29]. The addition of the colored noise term is a complication, and we specifically wish to investigate the effect the correlation time has on stochastic resonance in this system (as a function of the colored noise strength).

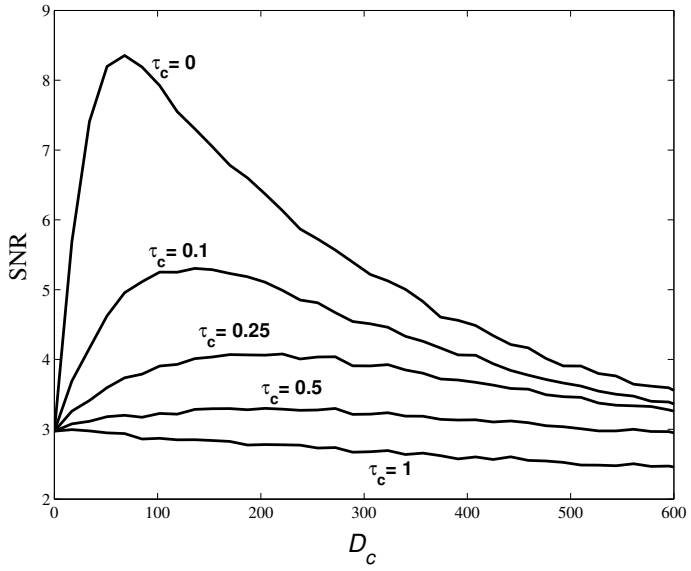

Figure 48: A plot of the numerically calculated signal to noise ratios versus colored noise intensity for various values of the correlation time. Notice that the peak of the SNR curve moves toward lower values of SNR and higher values of noise intensity as the correlation time is increased. The peak disappears for correlation times near unity. Here $a = 32$, $b = 1$, $A = 8$, $\omega_s = .031$ and $D_w = 75$. The data are interpolated with straight lines for ease of viewing.

Figure 48 shows the results of direct Monte Carlo integration of Equation (149). Six curves are shown, each representing the SNR of the system versus D_c for different values of τ_c. Notice that the stochastic resonance peak in each SNR curve changes as the correlation time is increased. Specifically, as τ_c increases, the peak shifts to *lower* values of SNR while simultaneously requiring a *higher* value of D_c to achieve the maximum. Also, note that the peak disappears altogether for larger values of τ_c.

We wish to explain this behavior theoretically, and to this end we will explore two different theories. The first theory is based on the work of Bezrukov [9, 10]. He postulates that if the correlation time of the colored noise is large, then it can be treated adiabatically. This led Bezrukov to model an excitable system with a stochastic rate – i.e. one in which the colored noise term is treated the same as the periodic signal. Bezrukov found that stochastic resonance still occurs in such system, and calculated sufficient conditions for its presence. We will attempt to use this "stochastic rate" theory approach for our two state (bistable) system. The second theory is a rate theory based on work by Fox [27, 28], who

was able to calculate the mean first passage times for systems with a single source of colored noise in the small τ_c limit. By extending that work to systems with both white and colored noises, a new mean first passage time (and hence rate) can be calculated.

We will show that stochastic rate theory does a poor job in describing stochastic resonance in a two state system with white and colored noise sources. Numerical integration of this model will show little in common with its Langevin equivalent. The match is bad enough that the overall validity of stochastic rates is questionable, and we will explore that aspect in more detail. The small τ_c rate theory does predict stochastic resonance, but the dependence on the correlation time is incorrect. As it turns out, the value of τ_c above which stochastic resonance "turns off" is in an intermediate regime inaccessible to either theory. Stochastic rate theory only works in the high τ_c limit, while small τ_c theory is only valid for extremely small values of τ_c.

6.1 Stochastic Rate Theory

We first turn to the problem of escape from a potential well in the presence of both white and colored noise sources. In particular we are interested in the stochastic differential equation

$$\dot{x} = A(x) + \xi_w(t) + \xi_c(t), \tag{154}$$

where $A(x)$ is the force on the particle due to the deterministic double well potential, and $\xi_w(t)$ and $\xi_c(t)$ are, again, the white and colored noise sources, respectively, with

$$\langle \xi_w(t) \rangle = \langle \xi_c(t) \rangle = 0, \tag{155}$$

$$\left\langle \xi_w(t)\xi_w(t') \right\rangle = 2D_w\delta(t-t'), \tag{156}$$

$$\left\langle \xi_c(t)\xi_c(t') \right\rangle = \frac{D_c}{\tau_c} \exp\left[-\frac{|t-t'|}{\tau_c} \right], \tag{157}$$

and

$$\left\langle \xi_w(t)\xi_c(t') \right\rangle = 0. \tag{158}$$

The correlation time, τ_c, sets the time scale over which the colored noise changes in time. In this section we will assume that τ_c is much larger than any other time scale in the problem.

Equation (154) can be rewritten to get rid of the colored noise term at the expense of adding another spatial dimension [27]. Specifically, we can rewrite Equation (154) as

$$\dot{x} = A(x) + \xi_w(t) + y \tag{159}$$

$$\dot{y} = -\frac{1}{\tau_c} y + \frac{D_c}{\tau_c} \zeta(t), \tag{160}$$

where $\zeta(t)$ is unit variance Gaussian white noise. Note that the correlations for the y variable (i.e. Equations (155) and (157), corresponding to the colored noise term) will only be correct provided one also averages the initial values of y over their stationary distribution [26]. Numerically this can be done by integrating the system until all transients in the y variable die out.

By examining the SDE for the y variable it becomes easy to see what happens in the limit $\tau_c \to \infty$. In that limit (provided D_c is finite) the right hand side of Equation (160) becomes zero. This means

$$\lim_{\tau_c \to \infty} y(t) = C, \tag{161}$$

for some arbitrary constant, C. In this case we can rewrite Equation (160) as

$$\dot{x} = A(x) + C + \xi_w(t). \tag{162}$$

Notice we have essentially reduced the dimension of the problem from two to one. The corresponding Fokker-Planck equation subsequently becomes

$$\frac{\partial P}{\partial t} = -\frac{\partial}{\partial x} \left[(A(x) + C) P \right] + D_w \frac{\partial^2 P}{\partial x^2}, \tag{163}$$

where $P = P(x, t | x_0, t_0)$ is the conditional probability density function.

While the limit of infinite correlation time is not very useful, it makes a good starting point for the relaxation of that limit. Imagine that instead of an infinite correlation time we now have a correlation time that is very large (many orders of magnitude larger than any other time scale in the problem), but still finite. It is not hard to imagine that during intervals of time much smaller than the correlation time the colored noise will appear constant. During those intervals a FPE much like Equation (163) should still be valid. The

FPE is then well approximated by

$$\frac{\partial P}{\partial t} = -\frac{\partial}{\partial x}\left[\left(A(x) + \xi_c(t)\right) P\right] + D_w \frac{\partial^2 P}{\partial x^2}. \tag{164}$$

In other words, we are assuming that the colored noise acts adiabatically on the system.

In one sense, this is not much different than the adiabatic approximation used by McNamara and Wiesenfeld in their derivation of the rate theory approach to classic stochastic resonance [70]. In that approximation the frequency of the drive is assumed to be very small, so that the period of oscillation is much larger than all other time scales. For systems with just white noise the SDE is

$$\dot{x} = A(x) + \epsilon \cos(\omega_s t + \phi) + \xi_w(t), \tag{165}$$

where ϵ, ω_s and ϕ are the amplitude, frequency and initial phase of the drive, respectively. Because the frequency is small, McNamara and Wiesenfeld assumed that the well known Kramers formula for the MFPT for this system could be used, provided the modulation of the barrier height due to the drive was taken into account. For

$$A(x) = ax - bx^3 \tag{166}$$

they found that the appropriate rates to use were

$$W_{\pm}(t) = \frac{a}{\sqrt{2}\pi} \exp\left[-\frac{1}{D_w}\left(\Delta U \pm \epsilon x_m \cos(\omega_s t + \phi)\right)\right], \tag{167}$$

where $\Delta U = a^2/4b$ and $x_m = \sqrt{a/b}$.

If Equation (167) is to be valid the period of the drive must be much larger than all other time scales. This is just the case that we want for the colored noise, where the correlation time is very large. By analogy, the escape rates out of the two wells (for the same $A(x)$) of Equation (154) should be

$$W_{\pm}(t) = \frac{a}{\sqrt{2}\pi} \exp\left[-\frac{1}{D_w}\left(\Delta U \pm x_m \xi_c(t)\right)\right], \tag{168}$$

provided that not only is the correlation time large enough, but also that D_c is small enough. (Recall that Equation (167) also requires the drive amplitude to be small.)

Our goal is to explain *stochastic resonance* in systems that contain both white and colored noise, and this means the sinusoidal drive term should be added to the argument of the exponent in Equation (168). In other words, for the SDE

$$\dot{x} = ax - bx^3 + \xi_w + \xi_c + \epsilon\cos(\omega_s t + \phi) \tag{169}$$

the subsequent rate is given by

$$W_{\pm}(t) = \frac{a}{\sqrt{2}\pi}\exp\left[-\frac{1}{D_w}\left(\Delta U \pm x_m\xi_c(t) \pm \epsilon x_m\cos(\omega_s t + \phi)\right)\right]. \tag{170}$$

The validity of Equation (170), which we call a *stochastic* rate, is what we wish to examine in this section.

Before we continue with the analysis we should pause to reflect on the meaning of Equation (170). Mathematically it is well defined – it is simply a time dependent rate in which some of the time dependence is stochastic. A rate is usually simply related to the inverse of the mean first passage time. Here, that definition has little meaning, since the inverse of this rate is definitely not simply related to the MFPT. In deriving it we assumed that $W_{\pm}^{-1}$ does represent the *time local* MFPT, but not the overall *global* MFPT.

Though there is some question as to what they represent, stochastic rates have previously been used in stochastic resonance studies. Bezrukov studied an excitable system in which the firing rates were stochastic [9, 10], and Ginzburg et al. [36] also used stochastic rates in their study of SR in voltage-gated ion channels in biological membranes. In neither study, however, is there an attempt to connect the stochastic rates to an underlying Langevin model. In fact, Bezrukov and Vodyanoy found that in order to see stochastic resonance the colored noise must be fast enough [9]. This is very similar to what we have found numerically for the two state system. This brings up an interesting conundrum, however. If, in order to exhibit SR, the correlation time of the colored noise must be small enough can the stochastic rate picture still be valid when it requires the correlation time to be very large? In other words, does the range of validity of the stochastic rate model (if it exists at all) extend to small enough τ_c so that SR can still be accurately modelled?

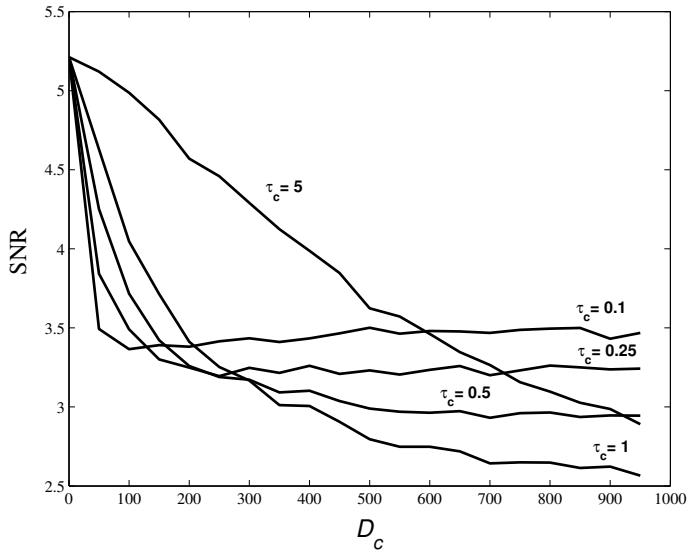

Figure 49: A plot of the numerically calculated signal to noise ratios versus colored noise intensity for various values of the correlation time in the stochastic rate model. Here $a = 32$, $b = 1$, $\epsilon = 8$, $\omega_s = 0.031$ and $D_w = 75$. The data are interpolated with straight lines for ease of viewing.

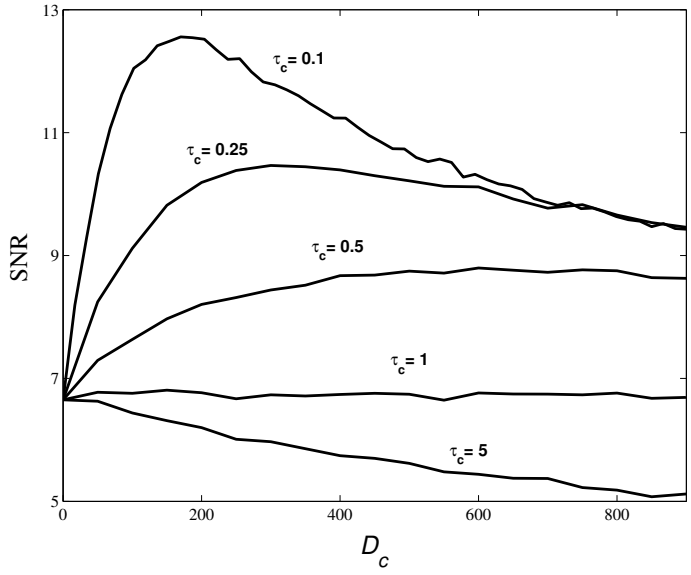

Figure 50: A plot of the numerically calculated signal to noise ratios versus colored noise intensity for various values of the correlation time in the Langevin model. Here $a = 32$, $b = 1$, $\epsilon = 8$, $\omega_s = 0.031$ and $D_w = 75$. The data are interpolated with straight lines for ease of viewing.

6.1.1 Comparing Stochastic Rate Theory to a Langevin Model

In order to test the validity of the stochastic rate model we integrate the stochastic rates and check if the resulting signal to noise ratios correspond to those of the integrated Langevin model. This is done by relating the time dependent rates given in Equation (170) to a two state Markov process. In other words, if the system is in state $s_{\pm}$, then the probability that the system switches to the other state at time t_i is given by

$$P(\pm \rightarrow \mp, t_i) = \Delta t W_{\pm}(t_i), \tag{171}$$

where Δt is the (small) integration time step. The results of such an integration are given in Figure 49, while the SNR curves for the corresponding Langevin model are shown in Figure 50.

It is obvious from Figures 49 and 50 that stochastic rate theory cannot explain the stochastic resonance of the Langevin model. The comparison is bad enough that it calls into question the validity of the stochastic rate model. The idea that the dynamics of a stochastic rate model can ever closely resemble those of a Langevin model needs to be explored. To this end let us strip away the sinusoidal drive needed for stochastic resonance. In other words, we wish to compare the stochastic differential equation

$$\dot{x} = ax - bx^3 + \xi_w(t) + \xi_c(t) \tag{172}$$

to the dynamics of a two state Markov process defined by the rates

$$W_{\pm}(t) = \frac{a}{\sqrt{2\pi}} \exp\left[-\frac{1}{D_w}\left(\Delta U \pm x_m \xi_c(t)\right)\right]. \tag{173}$$

The question then becomes: is there a limit in which stochastic rate theory works?

Because there is no sinusoidal drive in Equation (172), the signal to noise ratio is no longer a good measure of the accuracy of stochastic rate theory. Instead, let us look at the resulting power spectra from the two systems. First examine Figure 51. Here we see the power spectra from both the stochastic rate model (circles) and the Langevin process (crosses) for a small value of the correlation time ($\tau_c = 0.1$). Note that the power spectrum from the Langevin process shows a Lorentzian shape typical of a system that switches

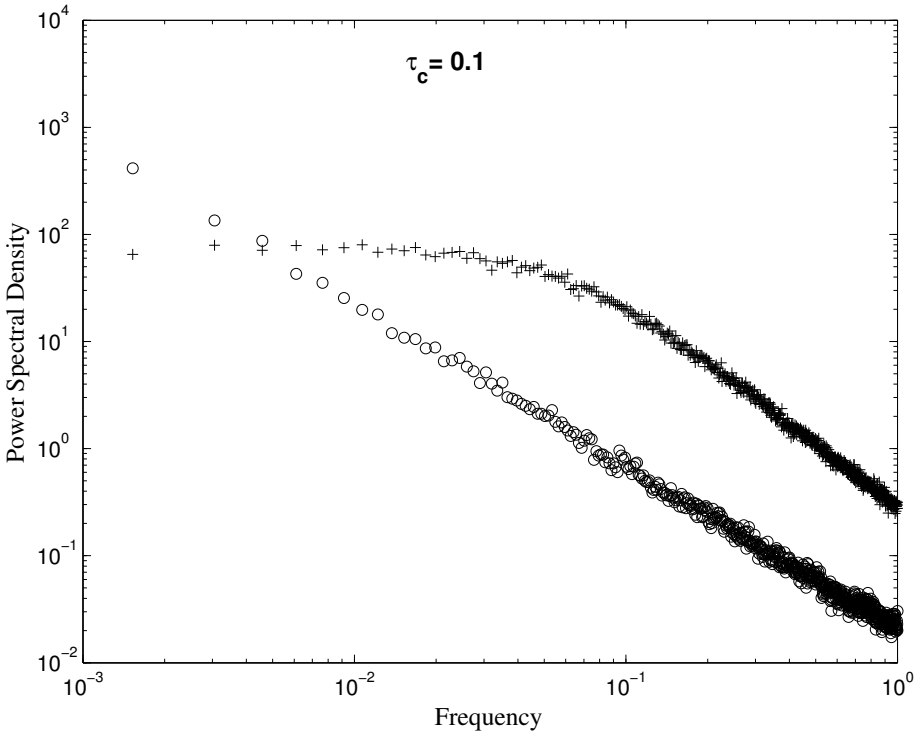

Figure 51: A comparison of the power spectral densities of the stochastic rate model (circles) and the Langevin model (crosses). Here $\tau_c = 0.1$, $a = 32$, $b = 1$, $D_w = 55$ and $D_c = 50$.

randomly between two states [81]. The Lorentzian has a corner frequency (the frequency at which the curve starts to decay with a power law) near $f = 0.07$ which is very near the pure white noise rate of the system,

$$W_0 = \frac{a}{\sqrt{2\pi}} \exp\left[-\frac{\Delta U}{D_w}\right], \tag{174}$$

which for the parameters used in the simulation is $W_0 \approx 0.069$.

The power spectrum of the stochastic rate model has a decidedly non-Lorentzian shape. It appears that its power spectrum decays with a power law throughout all frequencies. Indeed, the power spectrum of the stochastic rate model is so different from that of the Langevin process that we should not expect the stochastic rate model to be able to predict anything about the Langevin process for such a small correlation time. But from our numerical experiments on stochastic resonance, we were not expecting good agreement between the two in this parameter regime.

Figure 52 shows a comparison between the two models for a higher value of the correlation time ($\tau_c = 10$). Here we still see a non-Lorentzian shape for the power spectrum of the stochastic rate model, though it has moved closer to the power spectrum of the Langevin system. The situation improves drastically if the correlation time is increased even further. Figure 53 shows a comparison when $\tau_c = 20$, Figure 54 when $\tau_c = 30$, and Figure 55 when $\tau_c = 100$. When $\tau_c = 20$ the power spectrum of the stochastic rate model begins to conform its shape to the Lorentzian, and when $\tau_c = 30$ its shape is very nearly Lorentzian with the same corner frequency as the Langevin power spectrum. When $\tau_c = 100$ the stochastic rate model does an excellent job in replicating the power spectrum of the Langevin system.

It appears, then, that stochastic rate theories *can* model Langevin processes, but only for correlation times that are very large. However, because the stochastic resonance that we are interested in happens at smaller values of the correlation time, stochastic rate theory cannot help us in explaining SR with white and colored noise. Subsequently, we turn next to a theory that is aimed at the opposite end of the τ_c scale. Whereas stochastic rate theory is valid for large values of τ_c, small τ_c rate theory is, as the name implies, an approach that is valid for very small values of τ_c.

6.2 A Small τ_c Rate Theory

Another possible way to analyze SR in systems with both white and colored noise is to use the theory of McNamara and Wiesenfeld [70], the result of which is identical to our derivation of the symmetric two state SR in Chapter 5. Recall that the signal to noise ratio was derived without knowledge of the explicit form of the rates. In Reference [70] a connection is made between the MFPT of a system and the escape rates and the theory then predicts stochastic resonance. This means that in our attempt to predict SR in our system, containing both white and colored noise, we must find the corresponding rates and plug them into Equation (128), which is the signal to noise ratio in the symmetric limit.

Unfortunately no theory exists which can find the MFPTs for any value of the correlation time. Perturbative approaches exist, however, that allow one to estimate the MFPTs for bistable systems in the presence of a single colored noise source with a small correlation

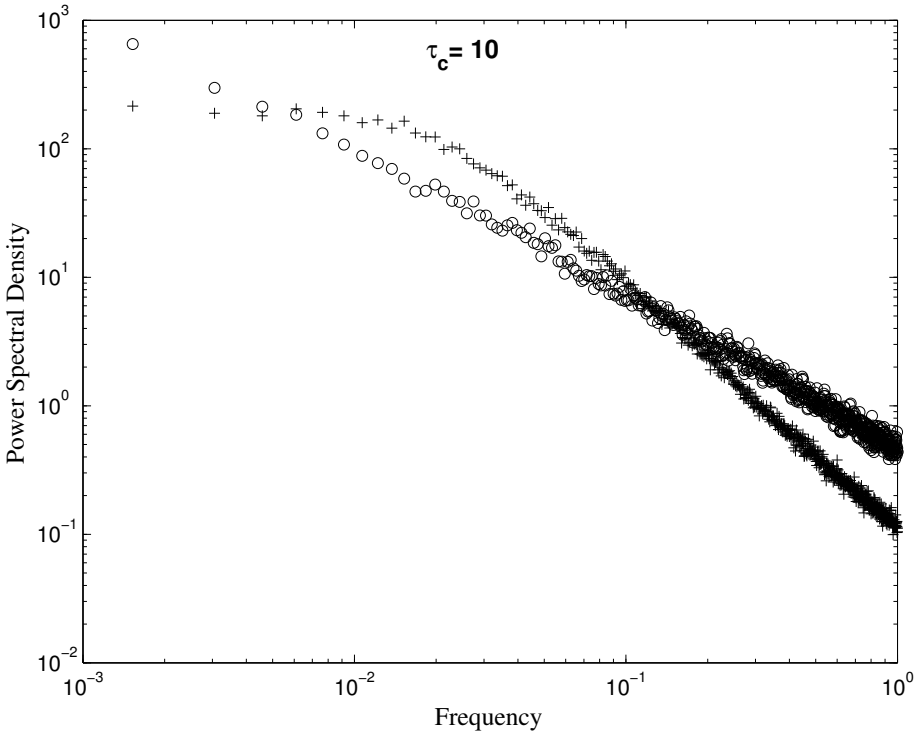

Figure 52: A comparison of the power spectral densities of the stochastic rate model (circles) and the Langevin model (crosses). Here $\tau_c = 10$, $a = 32$, $b = 1$, $D_w = 55$ and $D_c = 50$.

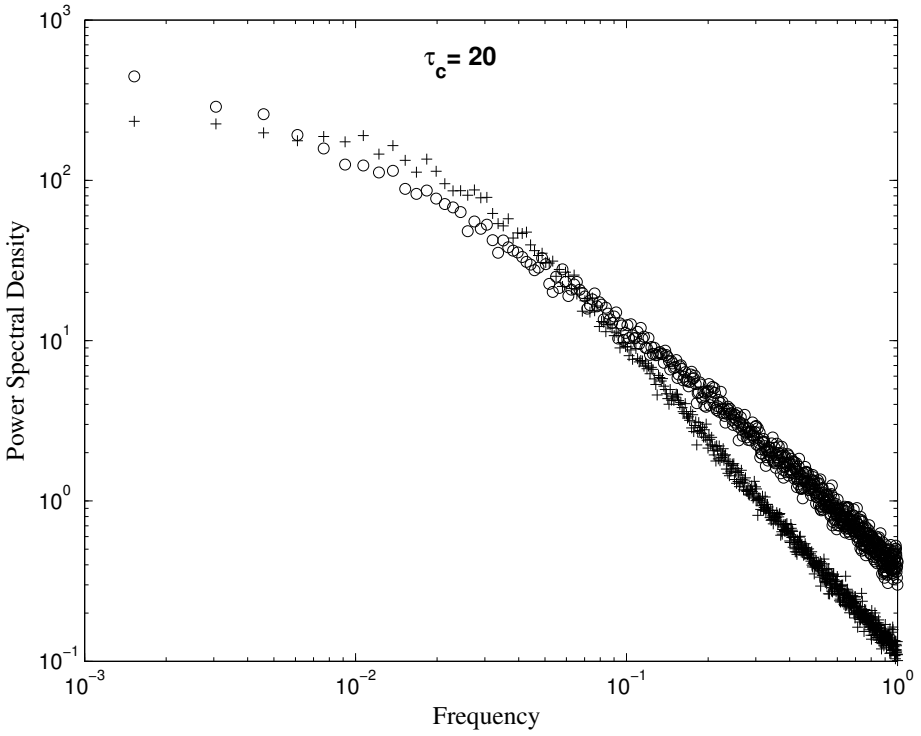

Figure 53: A comparison of the power spectral densities of the stochastic rate model (circles) and the Langevin model (crosses). Here $\tau_c = 20$, $a = 32$, $b = 1$, $D_w = 55$ and $D_c = 50$.

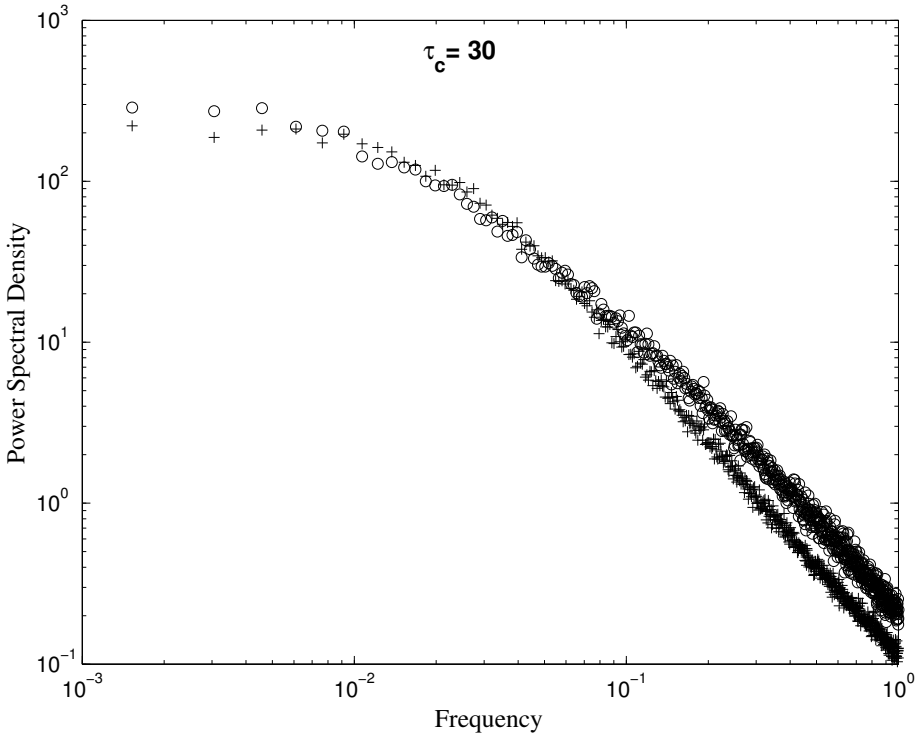

Figure 54: A comparison of the power spectral densities of the stochastic rate model (circles) and the Langevin model (crosses). Here $\tau_c = 30$, $a = 32$, $b = 1$, $D_w = 55$ and $D_c = 50$.

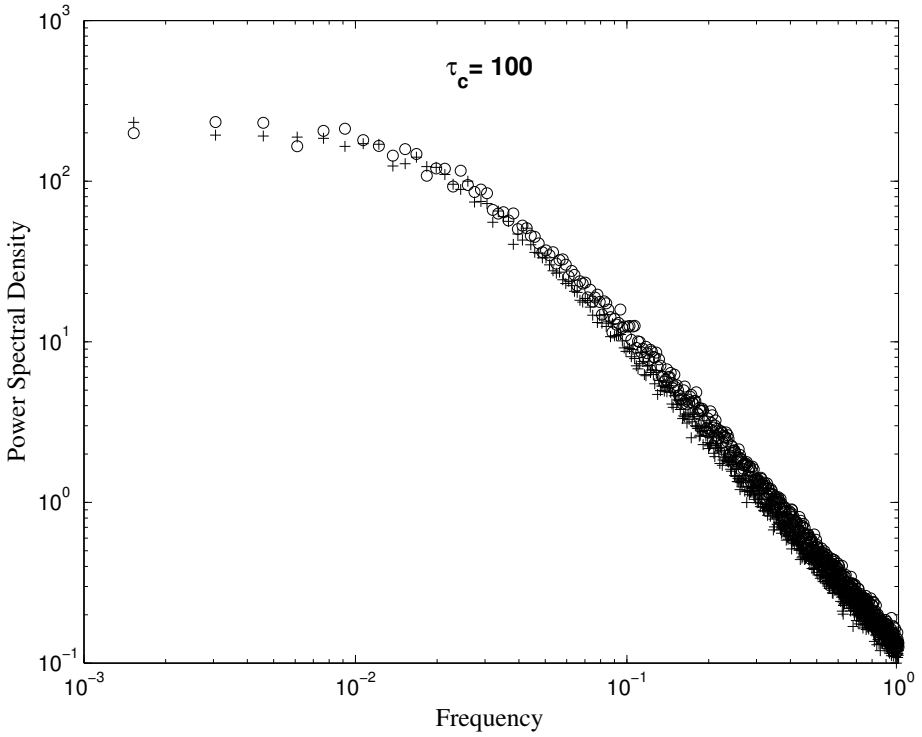

Figure 55: A comparison of the power spectral densities of the stochastic rate model (circles) and the Langevin model (crosses). Here $\tau_c = 100$, $a = 32$, $b = 1$, $D_w = 55$ and $D_c = 50$.

time. In what follows, we will extend Fox's functional calculus approach [27, 28] that allowed him to calculate an effective Fokker-Planck equation (EFPE) describing the probability distribution, and subsequently estimate the MFPT for systems with a single source of correlated noise. This extension allows us to write down a MFPT for a system containing many noise sources with multiple correlation times. We will then compare the resulting predictions for the SNR of the system to simulations.

6.2.1 The Effective Fokker-Planck Equation

For stochastic differential equations (SDEs) containing Gaussian white noise, we can write down the corresponding Fokker-Planck equation (FPE) which governs the probability distribution [35]. For instance, in one dimension, the SDE

$$\dot{x} = A(x) + \sqrt{B(x)}\xi_w(t), \tag{175}$$

where

$$\langle \xi_w(t) \rangle = 0 \tag{176}$$

and

$$\left\langle \xi_w(t)\xi_w(t') \right\rangle = \delta(t - t'), \tag{177}$$

leads to the FPE

$$\frac{\partial}{\partial t}P = -\frac{\partial}{\partial x}\left[A(x)P\right] + \frac{1}{2}\frac{\partial^2}{\partial x^2}\left[B(x)P\right], \tag{178}$$

where

$$P = P(x, t; x_0, t_0) \tag{179}$$

and P has the initial condition

$$P(x, t_0; x_0, t_0) = \delta(x - x_0). \tag{180}$$

Given the functions $A(x)$ and $B(x)$ one may then calculate MFPTs from the FPE [35].

Unfortunately no method exists for writing down a FPE for colored noise that has just one spatial dimension. This is due to the non-Markovian nature of colored noise, and FPEs are only valid for Markov processes (i.e. for SDEs that contain only white noise). If the

noise is such that the correlation is given by Equation (152) then it is possible to write the one dimensional SDE

$$\dot{x} = A(x) + \xi_c(t) \tag{181}$$

as the two dimensional system

$$\dot{x} = A(x) + y \tag{182}$$

$$\dot{y} = -\frac{1}{\tau_c} y + \frac{1}{\tau_c} \xi_y(t), \tag{183}$$

where

$$\langle \xi_y(t) \rangle = 0 \tag{184}$$

and

$$\left\langle \xi_y(t) \xi_y(t') \right\rangle = 2D_c \delta(t - t'), \tag{185}$$

provided that one, again, also averages the initial values of y over their stationary distribution [26].

Notice that in this two dimensional form the noise term, $\xi_y(t)$, is now Gaussian white noise. This has changed the nature of the problem from that of a non-Markovian process to one that is Markovian, at the expense of adding a spatial dimension. This trade off allows us to write down a two dimensional FPE [35] of the form

$$\frac{\partial}{\partial t} P = -\frac{\partial}{\partial x} \left[(A(x) + y) \, P \right] + \frac{\partial}{\partial y} \left[\left(\frac{y}{\tau_c} + \frac{D_c}{\tau_c^2} \frac{\partial}{\partial y} \right) P \right]. \tag{186}$$

Unlike its one dimensional analogue, an analytic expression for the MFPT derived from Equation (186) has yet to be calculated [28]. What is needed, then, is an approximate *one* dimensional FPE that can be used when the correlation time of the colored noise is small. Fox [27] was able to use a functional calculus approach that allowed him to calculate the effective Fokker-Planck equation (EFPE) for systems such as Equation (181) that is valid for small τ_c. He found the EFPE has the form

$$\frac{\partial}{\partial t} P = -\frac{\partial}{\partial x} \left[A(x) P \right] + D_c \frac{\partial^2}{\partial x^2} \left[\frac{1}{1 - \tau_c A'(x)} P \right], \tag{187}$$

where the prime indicates differentiation with respect to x. Because the EFPE is one dimensional it is possible to calculate MFPTs from it.

We can extend this result to a system that has N sources of noise which are uncorrelated with each other, but not necessarily uncorrelated in time. In particular, we examine the equation

$$\dot{x} = A(x) + \sum_{i=1}^{N} \xi_i(t), \tag{188}$$

where

$$\langle \xi_i(t) \rangle = 0 \tag{189}$$

and

$$\left\langle \xi_i(t)\xi_j(t') \right\rangle = \frac{\delta_{ij} D_i}{\tau_i} \exp\left[-\frac{|t-t'|}{\tau_i} \right], \tag{190}$$

where D_i and τ_i are noise strength the correlation time of time of the i^{th} noise source, respectively, and δ_{ij} is the Kronecker delta function. Since each noise source is uncorrelated with the others, each source adds its own diffusion term to the EFPE similar to that in Equation (187). The resulting EFPE for Equation (188) then becomes

$$\frac{\partial}{\partial t} P = -\frac{\partial}{\partial x} \left[A(x) P \right] + \frac{\partial^2}{\partial x^2} \left[\sum_{i=1}^{N} \frac{D_i}{1 - \tau_i A'(x)} P \right]. \tag{191}$$

For the system we are interested in, Equation (149), there only two noise sources, one white and one colored. The white noise source can be obtained from Equation (190) in the limit $\tau_i \to 0$. The resulting EFPE for Equation (149) is then given by

$$\frac{\partial P}{\partial t} = -\frac{\partial}{\partial y} \left[W(y) P \right] + \frac{\partial^2}{\partial y^2} \left\{ \left[D_w + \frac{D_c}{1 - \tau_c W'(y)} \right] P \right\}. \tag{192}$$

Equation (192) will allow us to calculate the mean first passage time that is needed to create a new rate theory for the two-state system with both white and colored noise.

6.2.2 The Mean First Passage Time for Systems with White and Colored Noise

Given a bistable system and its corresponding Fokker Planck equation of the form

$$\frac{\partial P}{\partial t} = -\frac{\partial}{\partial y} \left\{ W(y) P \right\} + \frac{\partial^2}{\partial y^2} \left\{ D(y) P \right\} \tag{193}$$

it is possible to derive a formula for the average time it takes for the particle to escape from one of the wells, the MFPT [28, 35]. For the quadratic double-well system given in Equation (149), where

$$W(x) = ax - bx^3, \tag{194}$$

this is tantamount to finding the average time, $T_{fp}(x_i)$, it takes for the particle, starting at position $x_i = -\sqrt{a/b}$ (the position of the left minimum), to reach the point $x_f = 0$ (the local maximum). This time is given explicitly by [28]

$$T_{fp}(-\sqrt{a/b}) = \int_{-\sqrt{a/b}}^{0} \mathrm{d}y \int_{-\infty}^{y} \mathrm{d}z \; \frac{\psi(z)}{\psi(y)} \frac{1}{D(z)}, \tag{195}$$

where

$$\psi(x) = \exp\left[\int_{-\infty}^{x} \mathrm{d}x' \; \frac{W(x')}{D(x')}\right]. \tag{196}$$

For systems with both white and colored noise the function $D(x)$ can be obtained directly from Equation (192):

$$D(x) = D_w + \frac{D_c}{1 - \tau_c W'(x)}. \tag{197}$$

The evaluation of the integrals in the expression for the MFPT, Equation (195), is our next task, and we will follow the technique of Fox [28], only modified to fit our problem. We begin by realizing that $1/\psi(y)$ is sharply peaked near $y = 0$. Also, since $D(z)$ is a slowly varying function of z, we can safely evaluate it near the peak of $\psi(z)$, namely $z = -\sqrt{a/b}$. These approximations yield

$$T_{fp}(-\sqrt{a/b}) \approx \left[\frac{\pi D(0)}{2a}\right]^{1/2} \frac{1}{D(-\sqrt{a/b})} \int_{-\infty}^{0} \mathrm{d}z \; \exp\left[\int_{0}^{z} \mathrm{d}x \; \frac{W(x)}{D(x)}\right]. \tag{198}$$

For small τ_c we can approximate $1/D(x)$, to first order in τ_c, as

$$\frac{1}{D(x)} \approx \frac{1}{\sigma}\left[1 - \frac{D_c W'(x)}{\sigma}\tau_c\right], \tag{199}$$

where $\sigma = D_w + D_c$. Plugging this in, and evaluating the resulting integral over x yields

$$T_{fp}(-\sqrt{a/b}) \approx \left[\frac{\pi D(0)}{2a}\right]^{1/2} \frac{1}{D(-\sqrt{a/b})} \int_{-\infty}^{0} \mathrm{d}z \; \exp\left[\alpha z^2 - \beta z^4 - \gamma z^6\right], \tag{200}$$

where

$$\alpha \equiv \frac{a}{2\sigma}\left(1 - \frac{D_c a \tau_c}{\sigma}\right), \tag{201}$$

$$\beta \equiv \frac{b}{4\sigma}\left(1 - \frac{4 D_c a \tau_c}{\sigma}\right) \tag{202}$$

and

$$\gamma \equiv \frac{D_c b^2 \tau_c}{2\sigma^2}. \tag{203}$$

Using the method of steepest descent on the remaining integral yields,

$$T_{fp}(-\sqrt{a/b}) \approx \left[\frac{\pi D(0)}{2a}\right]^{1/2} \frac{1}{D(-\sqrt{a/b})} \left[\frac{\pi\sigma}{a\left(1+\frac{2D_c a\tau_c}{\sigma}\right)}\right]^{1/2} \exp\left[\frac{a^2}{4b\sigma}\right]. \tag{204}$$

Plugging in the appropriate expressions for $D(0)$ and $D(-\sqrt{a/b})$ gives us our final result,

$$T_{fp}(-\sqrt{a/b}) \approx \frac{\pi}{\sqrt{2}a} \left[\frac{\sigma + 2D_c a\tau_c}{\sigma - D_c a\tau_c}\right]^{1/2} \exp\left[\frac{a^2}{4b\sigma}\right]. \tag{205}$$

Because of the τ_c dependence in the denominator if Equation (197) there is a limit to the range validity of both Equations (200) and (205). In particular, in order for them to be valid, the inequality

$$\tau_c < \frac{1}{W'(0)} = \frac{1}{a} \tag{206}$$

must hold. When this inequality does hold, Equation (205) does a decent job of approximating Equation (200), as is demonstrated in Figure 56.

Recall that Equation (205) is based upon the EFPE, Equation (192), which is itself a small τ_c approximation of the true probability evolution equation for the underlying SDE, Equation (149). This means that while Inequality (206) sets a limit on the possible range of validity for τ_c, it is only an upper bound. The true upper limit for τ_c may be lower than $1/a$. Due to differences in time scales that arise for such small values of τ_c, numerical simulations of Equation (149) take prohibitively long to compute. Additionally, as we will see in the next section, signal to noise ratios calculated using rates derived from Equation (205) compare poorly with those obtained from direct simulation of Equation (149). For these reasons, direct comparisons of Equation (205) to MFPTs obtained from simulation of Equation (149) have not been done.

Though direct comparison to simulation is difficult, three important limits exist that can give us confidence that Equation (205) is the correct formula for small values of τ_c. First, in the absence of the colored noise, the mean first passage time should limit to the well known Kramers formula, which it does:

$$\lim_{D_c \to 0} T_{fp} = \frac{\pi}{\sqrt{2}a} \exp\left[\frac{\Delta U}{D_w}\right], \tag{207}$$

where $\Delta U = a^2/4b$ is the barrier height. Second, if the correlation time of the colored noise goes to zero, the colored noise becomes white. In that limit the MFPT should be the

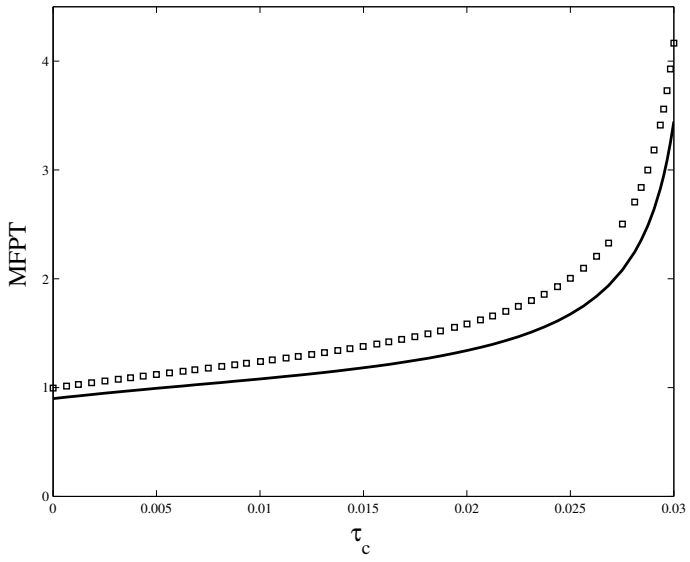

Figure 56: A comparison of the MFPT approximated by the method of steepest descent, Equation (205) (solid line), and numerically calculated values of Equation (200) (squares). Here $D_w = D_c = 50$, $a = 32$ and $b = 1$. Both approximations are valid only when $\tau_c < 1/a \approx 0.03$.

Kramers formula, but the noise intensity should be the sum of both the noise terms. Again, this is the case:

$$\lim_{\tau_c \to 0} T_{fp} = \frac{\pi}{\sqrt{2}a} \exp\left[\frac{\Delta U}{D_w + D_c}\right]. \tag{208}$$

Finally, if the intensity of the white noise goes to zero, the system is then driven by just the colored noise. This limit was first calculated by Hänggi et al. [42], and later verified by Fox [28]. Our expression for the MFPT does indeed have this limit, with result

$$\lim_{D_w \to 0} T_{fp} = \frac{\pi}{\sqrt{2}a} \left[\frac{1 + 2a\tau_c}{1 - a\tau_c}\right]^{1/2} \exp\left[\frac{\Delta U}{D_c}\right]. \tag{209}$$

6.2.3 SR Using Small τ_c Rate Theory

Recall that in Chapter 5 we used the rates

$$W_\pm = \alpha \pm \epsilon \cos(\omega_s t + \phi) \tag{210}$$

to derive the signal to noise ratio for a symmetric system, with result,

$$R_s = \frac{\pi \epsilon^2}{2\alpha} \left\{1 - \frac{2\epsilon^2}{4\alpha^2 + \omega_s^2}\right\}^{-1}. \tag{211}$$

McNamara and Wiesenfeld were able to show that the continuous dynamics of a symmetric double well system are well approximated by a two state rate model provided that the rates out of the left (-) and right (+) wells are given by [70]

$$W_{\pm}(t) = \frac{1}{2T_{fp,\pm}(t)}. \tag{212}$$

If we use the MFPT for our system (Equation (205)), calculated in the previous section, we see that the corresponding rates are

$$W_{\pm}(t) = \frac{a}{\sqrt{2}\pi}\sqrt{\frac{\sigma - D_c a\tau_c}{\sigma + 2D_c a\tau_c}}\exp\left[-\frac{\Delta U_{\pm}(t)}{\sigma}\right], \tag{213}$$

where $\Delta U_{\pm}(t)$ is the time dependent barrier height of the left or right well, given by

$$\Delta U_{\pm}(t) = \frac{a^2}{4b} \pm \sqrt{\frac{a}{b}}A\cos(\omega_s t + \phi). \tag{214}$$

For small driving amplitudes, A, we can Taylor expand Equation (213) to get, to first order in A,

$$W_{\pm}(t) \approx \frac{a}{\sqrt{2}\pi}\sqrt{\frac{\sigma - D_c a\tau_c}{\sigma + 2D_c a\tau_c}}\exp\left[-\frac{a^2}{4b\sigma}\right]\left\{1 \mp \sqrt{\frac{a}{b}}\frac{A}{\sigma}\cos(\omega_s t + \phi)\right\}. \tag{215}$$

Writing Equation (215) as

$$W_{\pm}(t) \approx \alpha \mp \epsilon\cos(\omega_s t + \phi) \tag{216}$$

we see that

$$\alpha = \frac{a}{\sqrt{2}\pi}\sqrt{\frac{\sigma - D_c a\tau_c}{\sigma + 2D_c a\tau_c}}\exp\left[-\frac{a^2}{4b\sigma}\right] \tag{217}$$

and

$$\epsilon = \frac{\alpha A}{\sigma}\sqrt{\frac{a}{b}}. \tag{218}$$

Plugging these rates into the Equation (211) allows us to find the signal to noise ratio for the system. Plots of the SNR for various values of the correlation time are shown in Figure 57, using the same parameters as those used in Figure 48. Notice that as the correlation time increases the peak of the SNR curve occurs at lower values of D_c and decreases in height. For large enough τ_c the peak vanishes altogether.

If we compare the analytic prediction, Figure 57, to the numerical results, Figure 48, we notice several things. We first note that for both the rate theory and the numerical

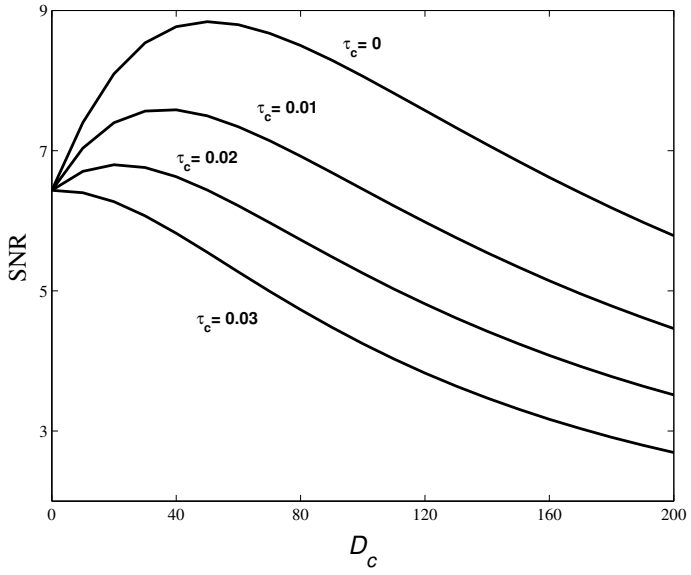

Figure 57: A plot of the theoretically calculated signal to noise ratios versus colored noise intensity for various values of the correlation time. Here $a = 32$, $b = 1$, $A = 8$, $\omega_s = .031$ and $D_w = 75$.

results, the peak value of the SNR decreases with increasing τ_c, and that the peak vanishes for high values of τ_c. This is where the similarity ends, however. Numerically we find that as τ_c increases, the peak of the SNR curve occurs at *higher* values of D_c, whereas just the opposite occurs in the theoretical model. Additionally, the values of τ_c for which the peak disappears altogether differs between the numerical and theoretical models. In the numerical model the peak disappears at $\tau_c \approx 1$, while in the theoretical model it disappears at some point when $0.02 < \tau_c < 0.03$, which is a difference of two orders of magnitude.

The failure of the small τ_c rate theory to predict the point at which SR no longer occurs in the system is not surprising. For the parameters used in the example, that point occurs when $\tau_c \approx 1$. As we explained earlier, small τ_c rate theory is only valid for values of τ_c that are at most $1/a$, which is roughly 0.03 here. Therefore, small τ_c rate theory could never have correctly predicted the turnover point in the SNR curves.

It should be noted that small τ_c rate theory converges to the correct value of the SNR in the white noise limit. Whether or not our theory is correct for extremely small values of τ_c (i.e. $\tau_c \ll 1/a$) is still undetermined. Unfortunately, verifying this is difficult for two reasons. First, the numerical model takes prohibitively long to integrate for very small τ_c.

This is due to the extremely small time step needed to accurately model noise with such a small correlation time. Second, it is unlikely that in regions where our theory is correct that it differs greatly from a McNamara model of the same system, treating the colored noise as purely white. In this case the differences are likely to be smaller than the intrinsic error of the McNamara theory.

What we are left with, then, is a theoretical model that is possibly correct in some limit, but that fails in parameter regimes of interest (namely those values of τ_c for which the peak in the SNR curve disappears). It may be possible to modify the derivation of the rates to include higher order terms of τ_c, but it is highly unlikely the realm of validity would increase by several orders of magnitude. Furthermore, to the best of our knowledge, no theory exists that can correctly predict the MFPTs of systems in which the correlation time is of order $1/a$ or greater.

6.3 Discussion

Though both small τ_c rate theory and stochastic rate theory have limits in which they are accurate, it would seem that neither is valid in the parameter regime we want. Small τ_c rate theory, which is accurate in the limit $\tau_c \to 0$, does indeed predict stochastic resonance, but cannot predict the value of τ_c for which SR no longer occurs. Stochastic rate theory, on the other hand, does predict the absence of SR at extremely large values of τ_c but likewise cannot predict the value of τ_c at which SR begins to occur.

The critical value of τ_c, below which SR occurs, lies directly in between the regimes of validity of the two theories. What is really needed is a theory that is valid for moderate values of τ_c. Unfortunately no such theory exists. The problem of moderate values of τ_c has historically been very stubborn, and the value of the critical correlation time, unluckily, falls within this moderate regime.

It is interesting to note that Bezrukov, in his study of an excitable system containing both white and colored noise does predict the critical value of the correlation time [9, 10]. He found that in order for stochastic resonance to occur, the correlation time of the colored

noise must be smaller than the bare transition time, i.e.

$$\tau_c < T_0. \tag{219}$$

The bare transition time corresponds to the inverse of the escape rate in the absence of the colored noise and sinusoidal drive. In our notation this would be

$$T_0 = W_0^{-1} = \frac{\sqrt{2}\pi}{a} \exp\left[\frac{\Delta U}{D_w}\right]. \tag{220}$$

The Bezrukov result does mirror our results for the two state system in that the correlation time must be fast enough in order to see stochastic resonance. In our two state system, however, a relation similar to Equation (219) could be found neither numerically nor analytically. However, Bezrukov takes as his starting point the stochastic rate model, with no mention of an underlying Langevin system. The question remains, then, whether or not the Bezrukov theory could be used to explain SR in excitable system described by SDEs.

If we look back to Figures 51–55 we can see that stochastic rate theory does not do a good job until the correlation time is greater than the bare transition time of the Langevin process. For those plots the bare transition time is $W_0^{-1} \approx 15$. A case could even be made that stochastic rate theory is not valid until τ_c is greater than the true transition time of the Langevin process. The true transition time, which is the inverse of the corner frequency, represents that actual time of transitions in the presence of both the white and the colored noise. As we can see from Figures 51–55 the corner frequency of the Langevin process decreases from roughly 0.07 to 0.02 as the correlation time increases. This means the true transition time increases from roughly 15 to 50 over that same span. Since the accuracy of the stochastic rate process does not occur until $\tau_c \gtrsim 30$, the true transition time might represent a more accurate boundary for the validity of stochastic rate theory.

Whatever the true boundary is for the accuracy of stochastic rate theory, the bare transition time seems to be a good lower bound. This means that in order for stochastic rate theory to be accurate we must have

$$\tau_c > T_0. \tag{221}$$

Compare this to Equation (219) and we see that there is a problem. Whereas Bezrukov requires $\tau_c < T_0$ in order to see stochastic resonance, we predict that $\tau_c > T_0$ needs to hold in order for stochastic rate theory to accurately model a Langevin process.

To be fair to Bezrukov, he never tries to make a connection between his theory and an underlying Langevin process. Treated mathematically, stochastic rates are well defined and Bezrukov's predictions about them are accurate. However, it is hard to read his papers and not come away with the impression that his stochastic rates are intended to model an underlying physical process, and hence a Langevin process.

It remains an open question, then, whether or not stochastic rate theory can accurately describe SR in excitable systems described by an SDE. Though theory seems to fail in the case of SR in a two state system, it would be wrong to extrapolate the results to an excitable system. However, the failure of the theory in the two state case brings their use in excitable systems into serious question. More work needs to be done to figure out exactly when stochastic rate theory can and cannot be used.

REFERENCES

[1] Alley, R. B., Anandakrishnan, S., and Jung, P., "Stochastic resonance in the North Atlantic," *Paleoceanography*, vol. 16, no. 2, pp. 190–198, 2001.

[2] Almaas, E. and Stroud, D., "Dynamics of a Josephson array in a resonant cavity," *Physical Review B*, vol. 65, no. 13, pp. 134502/1–14, 2002.

[3] Benzi, R., Pandolfo, J. P., and Sutera, A., "Further application of the theory of stochastic perturbation of deterministic systems to simple climate models," *Quarterly Journal of the Royal Meteorological Society*, vol. 107, no. 453, pp. 549–559, 1981.

[4] Benzi, R., Parisi, G., Sutera, A., and Vulpiani, A., "Stochastic resonance in climatic change," *Tellus*, vol. 34, no. 1, pp. 10–16, 1982.

[5] Benzi, R., Parisi, G., Sutera, A., and Vulpiani, A., "A theory of stochastic resonance in climatic change," *SIAM Journal on Applied Maathematics*, vol. 43, no. 3, pp. 565–78, 1983.

[6] Benzi, R., Sutera, A., and Vulpiani, A., "The mechanism of stochastic resonance," *Journal of Physics A*, vol. 14, no. 11, pp. L453–L457, 1981.

[7] Berdichevsky, V. and Gitterman, M., "Stochastic resonance in linear systems subject to multiplicative and additive noise," *Physical Review E*, vol. 60, no. 2, pp. 1494–1499, 1999.

[8] Bezrukov, S. M. and Vodyanoy, I., "Noise-induced enhancement of signal transduction across voltage-dependent ion channels," *Nature*, vol. 378, no. 6555, pp. 362–364, 1995.

[9] Bezrukov, S. M. and Vodyanoy, I., "Stochastic resonance in non–dynamical systems without response thresholds," *Nature*, vol. 385, no. 6614, pp. 319–321, 1997.

[10] Bezrukov, S. M., "Stochastic resonance as an inherent property of rate–modulated random series of events," *Physics Letters A*, vol. 248, no. 1, pp. 29–36, 1998.

[11] Bi, B., Han, S., Lukens, J. E., and Wan, K., "Distributed Josephson junction arrays as local oscillators," *IEEE Transactions on Applied Superconductivity*, vol. 3, no. 1, pp. 2303–2306, 1993.

[12] Booi, P. A. A. and Benz, S. P., "Emission linewidth measurements of two-dimensional array Josephson oscillators," *Applied Physics Letters*, vol. 64, no. 16, pp. 2163–2165, 1994.

[13] Booi, P. A. A. and Benz, S. P., "High power generation with distributed Josephson-junction arrays," *Applied Physics Letters*, vol. 68, no. 26, pp. 3799–3801, 1996.

[14] Bulsara, A., Jacobs, E. W., Zhou, T., Moss, F., and Kiss, L., "Stochastic resonance in a single neuron model: Theory and analog simulation," *Journal of Theoretical Biology*, vol. 152, pp. 531–556, 1991.

[15] Burhkhardt, H., Brugmann, O., Rauther, A., Schnell, F., and Schilling, M., "Very large $YBa_2Cu_3O_7$-Jospehson-junction arrays," *IEEE Transactions on Applied Superconductivity*, vol. 9, no. 2, pp. 3153–3156, 1999.

[16] Cawthorne, A. B., Barbara, P., Shitov, S. V., Lobb, C. J., Wiesenfeld, K., and Zangwill, A., "Synchronized oscillations in Josephson junction arrays: The role of distributed coupling," *Physical Review B*, vol. 60, no. 10, pp. 7575–7578, 1999.

[17] Cawthorne, A. B., *Dynamics of Josephson Junctions and Josephson Junction Arrays*. PhD thesis, University of Maryland at College Park, 1998.

[18] Clark, T. D., "Experiments on coupled Josephson junctions," *Physics Letters*, vol. 27A, no. 9, pp. 585–586, 1968.

[19] Collins, J. J., Imhoff, T. T., and Grigg, P., "Noise-enhanced information transmission in rat SA1 cutaneous mechanoreceptors via aperiodic stochastic resonance," *Journal of Neurophysiology*, vol. 76, no. 1, pp. 642–645, 1996.

[20] deGennes, P. G., *Supeconductivity of Metals and Alloys*. Reading, Massachusetts: Addison Wesley, 1989.

[21] Dhamala, M. and Wiesenfeld, K., "Generalized stability law for Josephson series arrays," *Physics Letters A*, vol. 292, no. 4–5, pp. 269–274, 2002.

[22] Douglass, J. K., Wilkens, L., Pantazelou, E., and Moss, F., "Noise enhancement of information transfer in crayfish mechanoreceptors by stochastic resonance," *Nature*, vol. 365, no. 6444, pp. 337–340, 1993.

[23] Dykman, M. I., Luchinsky, D. G., Mannella, R., McClintock, P. V. E., Stein, N. D., and Stocks, N. G., "Stochastic resonance in perspective," *Il Nuovo Cimento*, vol. 17D, no. 7–8, pp. 661–683, 1995.

[24] Fauve, S. and Heslot, F., "Stochastic resonance in a bistable system," *Physics Letters A*, vol. 97A, no. 1–2, pp. 5–7, 1983.

[25] Feynman, R. P., Leighton, R. B., and Sands, M., *The Feynman Lectures on Physics*, vol. III. Reading, Massachusetts: Addison-Wesley, 1965.

[26] Fox, R. F., "Numerical simulations of stochastic differential equations," *Journal of Statistical Physics*, vol. 54, no. 5/6, pp. 1353–1366, 1989.

[27] Fox, R. F., "Functional-calculus approach to stochastic differential equations," *Physical Review A*, vol. 33, no. 1, pp. 467–476, 1986.

[28] Fox, R. F., "Mean first-passage times and colored noise," *Physical Review A*, vol. 37, no. 3, pp. 911–917, 1988.

[29] Fox, R. F., "Stochastic resonance in a double well," *Physical Review A*, vol. 39, no. 8, pp. 4148–4153, 1989.

[30] Freund, J. A., Schimansky-Geier, L., Beisner, B., Neiman, A., Russell, D. F., Yakusheva, T., and Moss, F., "Behavioral stochastic resonance: How the noise from a *Daphnia* swarm enhances individual pray capture by juvenile paddlefish," *Journal of Theoretical Biology*, vol. 214, no. 1, pp. 71–83, 2002.

[31] Gammaitoni, L., Marchesoni, F., Menichella-Saetta, E., and Santucci, S., "Stochastic resonance in bistable systems," *Physical Review Letters*, vol. 62, no. 4, pp. 349–352, 1989.

[32] Gammaitoni, L., Menichella-Saetta, E., Santucci, S., Marchesoni, F., and Presilla, C., "Periodically time-modulated bistable systems: Stochastic resonance," *Physical Review A*, vol. 40, no. 4, pp. 2114–2119, 1989.

[33] Ganopolski, A. and Rahmstorf, S., "Rapid changes of glacial climate simulated in a coupled climate model," *Nature*, vol. 409, no. 6817, pp. 153–158, 2001.

[34] Ganopolski, A. and Rahmstorf, S., "Abrupt glacial climate changes due to stochastic resonance," *Physical Review Letters*, vol. 88, no. 3, pp. 038501/1–4, 2002.

[35] Gardiner, C. W., *Handbook of Stochastic Methods for Physics, Chemistry and the Natural Sciences*. New York, New York: Spring-Verlag, 1983.

[36] Ginzburg, S. L. and Pustovoit, M. A., "Stochastic resoance in two-state model of membrane channel with comparable opening and closing rates," *Physical Review E*, vol. 66, no. 2, pp. 1–9, 2002.

[37] Hadley, P., *Dynamics of Josephson junction arrays*. PhD thesis, Stanford University, 1989.

[38] Hadley, P. and Beasley, M. R., "Dynamical states and stability of linear arrays of Josephson junctions," *Applied Physics Letters*, vol. 50, no. 10, pp. 621–623, 1987.

[39] Halliday, D., Resnick, R., and Walker, J., *Fundamentals of Physics Extended*. New York, New York: Wiley, 2003.

[40] Hamilton, C. A., Burroughs, C. J., and Benz, S. P., "Josephson voltage standard - a review," *IEEE Transactions on Applied Superconductivity*, vol. 7, no. 2, pp. 3756–3761, 1997.

[41] Han, S., Bi, B., Zhang, W., and Lukens, J. E., "Demonstration of Josephson effect submillimeter wave sources with incresed power," *Applied Physics Letters*, vol. 64, no. 11, pp. 1424–1426, 1994.

[42] Hänggi, P., Marchesoni, F., and Grigolini, P., "Bistable flow driven by coloured Gaussian noise: a critical study," *Zeitschrift für Physik B*, vol. 56, no. 4, pp. 333–339, 1984.

[43] Hänggi, P., Jung, P., Zerbe, C., and Moss, F., "Can colored noise improve stochastic resonance?," *Journal of Statistical Physics*, vol. 70, no. 1–2, pp. 25–47, 1993.

[44] Hänggi, P., Talkner, P., and Borkovec, M., "Reaction-rate theory: fifty years after Kramers," *Reviews of Modern Physics*, vol. 62, no. 2, pp. 251–341, 1990.

[45] Harbaugh, J. K. and Stroud, D., "Model for a Josephson junction array coupled to a resonant cavity," *Physical Review B*, vol. 61, no. 21, pp. 14765–14772, 2000.

[46] Heath, T., *Synchronization and phase dynamics of coupled oscillators*. PhD thesis, Georgia Institute of Technology, 1999.

[47] Henry, K. R., "Noise improves transfer of near-threshold, phase-locked activity of the cochlear nerve: evidence for stochastic resonance?," *Journal of Comparative Physiology A*, vol. 184, no. 6, pp. 577–584, 1999.

[48] Hibbs, A., Jacobs, E. W., Bekkedahl, J., Bulsara, A., and Moss, F., "Stochastic resonance in a bistable SQUID loop," *AIP Conference Proceedings*, no. 285, pp. 720–723, 1993.

[49] Hibbs, A. D., Singsaas, A. L., Jacobs, E. W., Bulsara, A. R., and Bekkedahl, J. J., "Stochastic resonance in a superconducting loop with a Josephson junction," *Journal of Applied Physics*, vol. 77, no. 6, pp. 2582–2590, 1995.

[50] Hidaka, I., Nozaki, D., and Yamamoto, Y., "Functional stochastic resonance in the human brain: noise induced sensitization of baroreflex system," *Physical Review Letters*, vol. 85, no. 17, pp. 3740–3743, 2000.

[51] Howard, J., Roberts, W. M., and Hudspeth, A. J., "Mechanoelectrical transduction by hair cells," *Annual Review of Biophysicsand Biophysical Chemistry*, vol. 17, pp. 99–124, 1988.

[52] Indresano, A. A., Frank, J. E., Middleton, P., and Jaramillo, F., "Mechanical noise enhances signal transmission in the bullfrog sacculus," *Journal of the Association for Research in Otolaryngology*, vol. 4, no. 3, pp. 363–370, 2003.

[53] Jain, A. K., Likharev, K., Lukens, J. E., and Sauvageau, J. E., "Mutual phase-locking in Josephson junction arrays," *Physics Reports*, vol. 109, no. 6, pp. 309–426, 1984.

[54] Jaramillo, F. and Wiesenfeld, K., "Mechanoelectrical transduction assisted by Brownian motion: a role for noise in the auditory system," *Nature Neuroscience*, vol. 1, no. 5, pp. 389–394, 1998.

[55] Jaramillo, F. and Wiesenfeld, K., "Physiological noise level enhances mechanoelectrical transduction in hair cells," *Chaos, Solitons and Fractals*, vol. 11, no. 12, pp. 1869–1874, 2000.

[56] Jia, Y., Yu, S., and Li, J., "Stochastic resonance in a bistable system subject to multiplicative and additive noise," *Physical Review E*, vol. 62, no. 2, pp. 1869–1878, 2000.

[57] Josephson, B. D., "Possible new effects in superconductive tunnelling," *Physics Letters*, vol. 1, no. 7, pp. 251–253, 1962.

[58] Kerr, R. A., "Does climate clock get a noisy boost?," *Science*, vol. 290, no. 5492, pp. 697–698, 2000.

[59] Kosinska, I., "Stochastic resonance in discrete kinetics with delay," *Physica A*, vol. 325, no. 1–2, pp. 116–123, 2003.

[60] Kramers, H. A., "Brownian motion in a field of force and the diffusion model of chemical reactions," *Physica*, vol. VII, no. 4, pp. 284–304, 1940.

[61] Kuramoto, Y., "Cooperative dynamics of oscillator community. A study based on lattice rings," *Progress of Theoretical Physics Supplement*, no. 79, pp. 191–122, 1984.

[62] Kuramoto, Y., *Chemical Oscillations, Waves, and Turbulence*. Mineola, New York: Dover, 2003.

[63] Levin, J. and Miller, J., "Broadband neural encoding in the cricket cercal sensory system enhanced by stochastic resonance," *Nature*, vol. 380, no. 6570, pp. 165–168, 1996.

[64] Li, J., "Effect of asymmetry on stochastic resonance and stochastic resonance induced by multiplicative noise and by mean-field coupling," *Physical Review E*, vol. 66, no. 3, pp. 031104/1–7, 2002.

[65] Likharev, K. K., *Dynamics of Josephson Junctions and Circuits*. New York, New York: Gordon and Breach, 1986.

[66] Lim, D. J., "Functional structure of the organ of Corti: a review," *Hearing Research*, vol. 22, no. 1–3, pp. 117–146, 1986.

[67] Linder, J. F., Bennett, M., and Wiesenfeld, K., "Stochastic resonance in the mechanoelectrical transduction of hair cells," *Physical Review E*, vol. 72, no. 5, pp. 051911/1–4, 2005.

[68] Longtin, A., Bulsara, A., and Moss, F., "Time-interval sequences in bistable systems and the noise-induced transmission of information by sensory neurons," *Physical Review Letters*, vol. 67, no. 5, pp. 656–659, 1991.

[69] McCumber, D. E., "Effect of ac impedance on dc voltage-current characteristics of superconductor weak-link junctions," *Journal of Applied Physics*, vol. 39, no. 7, pp. 3113–3118, 1968.

[70] McNamara, B. and Wiesenfeld, K., "Theory of stochastic resonance," *Physical Review A*, vol. 39, pp. 4854–4869, May 1989.

[71] McNamara, B., Wiesenfeld, K., and Roy, R., "Observation of stochastic resonance in a ring laser," *Physical Review Letters*, vol. 60, no. 25, pp. 2626–2629, 1988.

[72] Misono, M., Kohmoto, T., Fukuda, Y., and Kunitomo, M., "Stochastic resonance in an optical bistable system driven by colored noise," *Optics Communicaations*, vol. 152, no. 4–6, pp. 255–258, 1998.

[73] Mori, T. and Kai, S., "Noise-induced entrainment and stochastic resonance in human brain waves," *Physical Review Letters*, vol. 88, pp. 218101/1–4, May 2002.

[74] Morse, R. P. and Roper, P., "Enhanced coding in a cochlear-implant model using additive noise: Aperiodic stochastic resonance with tuning," *Physical Review E*, vol. 61, pp. 5683–5692, May 2000.

[75] Nichols, S. and Wiesenfeld, K., "Ubiquitous neutral stability of splay-phase states," *Physical Review A*, vol. 45, no. 12, pp. 8430–8435, 1992.

[76] Nicolis, C., "Solar variability and the stochastic effects on climate," *Solar Physics*, vol. 74, no. 2, pp. 473–478, 1981.

[77] Nicolis, C., "Stochastic aspects of climatic transitions-repsonse to periodic forcing," *Tellus*, vol. 34, no. 1, pp. 1–9, 1982.

[78] Ovsyannikov, G. A., Ivanov, Z. G., Mygind, J., and Pederson, N. F., "Microwave radiation from 2-D arrays of high-T_c Josephson junctions," *Physica B*, vol. 194–196, pp. 107–108, 1994.

[79] Pogorzelski, R. J., "A two-dimensional coupled oscillator array," *IEEE Microwave and Guided Wave Letters*, vol. 10, no. 11, pp. 478–480, 2000.

[80] Priplata, A., Niemi, J., Salen, M., Harry, J., Lipsitz, L. A., and Collins, J. J., "Noise-enhanced human balance control," *Physical Review Letters*, vol. 89, no. 23, pp. 238101/1–4, 2002.

[81] Rice, S. O., "Mathematical analysis of random noise," in *Selected Papers on Noise and Stochastic Processes* (Wax, N., ed.), New York, New York: Dover, 1954.

[82] Rozenfeld, R., Neiman, A., and Schimansky-Geier, L., "Stochastic resonance enhanced by dichotomic noise in a bistable system," *Physical Review E*, vol. 62, no. 3, pp. R3031–R3034, 2000.

[83] Russell, D. F., Wilkens, L. A., and Moss, F., "Use of behavioural stochastic resonance by paddlefish for feeding," *Nature*, vol. 402, no. 6759, pp. 291–294, 1999.

[84] Savageau, J. E., *Phase-locking in distributed arrays of Josephson junctions.* PhD thesis, State University of New York, Stony Brook, 1987.

[85] Schwartz, I. B. and Tsang, K. Y., "Antiphase switching in Josephson junction arrays," *Physical Review Letters*, vol. 73, no. 21, pp. 2797–2800, 1994.

[86] Strogatz, S. H., "From Kuramoto to Crawford: exploring the onset of synchronization in populations of coupled oscillators," *Physica D*, vol. 143, no. 1–4, pp. 1–20, 2000.

[87] Strogatz, S. H., *Sync.* New York, New York: Hyperion, 2003.

[88] Strogatz, S. H. and Stewart, I., "Coupled oscillators and biological synchronization," *Scientific American*, vol. 269, no. 6, pp. 102–109, 1993.

[89] Swift, J. W., Strogatz, S. H., and Wiesenfeld, K., "Averaging of globally coupled oscillators," *Physica D*, vol. 55, pp. 239–250, 1992.

[90] Tilley, D. R., "Superradiance in arrays of superconducting weak links," *Physics Letters*, vol. 33A, no. 4, pp. 205–206, 1970.

[91] Tinkham, M., *Introduction to Superconductivity.* New York, New York: McGraw-Hill, second ed., 1996.

[92] Tsygankov, D. and Wiesenfeld, K., "Spontaneous synchronization in a Josephson transmission line," *Physical Review E*, vol. 66, no. 3, pp. 36215/1–9, 2002.

[93] Tsygankov, D. and Wiesenfeld, K., "Spontaneous formation of inert oscillator pairs," *Physics Letters A*, vol. 325, pp. 51–56, May 2004.

[94] Vasilić, B., Shitov, S. V., Lobb, C. J., and Barbara, P., "Josephson-junction arrays as high-efficiency sources of coherent millimeter-wave radiation," *Applied Physics Letters*, vol. 78, no. 8, pp. 1137–1139, 2001.

[95] Vemuri, G. and Roy, R., "Stochastic resonance in a bistable ring laser," *Physical Review A*, vol. 39, pp. 4668–4674, May 1989.

[96] Wan, K., Jain, A. K., and Lukens, J. E., "Submillimeter wave generation using Josephson junction arrays," *Applied Physics Letters*, vol. 54, pp. 1805–1807, May 1989.

[97] Watanabe, S. and Strogatz, S. H., "Constants of motion for superconducting Josephson arrays," *Physica D*, vol. 74, pp. 197–253, 1994.

[98] Wiesenfeld, K., Colet, P., and Strogatz, S. H., "Synchronization transitions in a disordered Josephson series array," *Physical Review Letters*, vol. 76, no. 3, pp. 404–407, 1996.

[99] Wiesenfeld, K., Colet, P., and Strogatz, S. H., "Frequency locking in Josephson arrays: connection with the Kuramoto model," *Physical Review E*, vol. 57, no. 2, pp. 1563–1569, 1998.

[100] Wiesenfeld, K. and DeMino, K., "Single-trigger stochastic resonance," *Nuovo Cimento D*, vol. 17D, no. 7–8, pp. 977–981, 1995.

[101] Wiesenfeld, K. and Moss, F., "Stochastic resonance and the benefits of noise: from ice ages to crayfish and SQUIDs," *Nature*, vol. 373, no. 6509, pp. 33–36, 1995.

[102] Wiesenfeld, K., Pierson, D., Pantazelou, E., Dames, C., and Moss, F., "Stochastic resonance on a circle," *Physical Review Letters*, vol. 72, no. 14, pp. 2125–2129, 1994.

[103] Wiesenfeld, K. and Swift, J. W., "Averaged equations for Josephson junction series arrays," *Physical Review E*, vol. 51, no. 2, pp. 1020–1025, 1995.

[104] York, R. and Popovic, Z., eds., *Active and Quasi-optical Arrays for Solid State Power Combining*. New York, New York: Wiley, 1997.

[105] Zaikin, A. A., Kurths, J., and Schimansky-Geier, L., "Doubly stochastic resonance," *Physical Review Letters*, vol. 85, no. 2, pp. 227–231, 2000.

VITA

Matthew Bennett was born on February 12th, 1974 in Kirksville Missouri. He originally attended the University of Michigan where he briefly studied linguistics and music composition. After a brief stint as a computer programmer Matthew decided that was to be his profession and tried to enroll at Georgia Tech with the intention of studying computer science. Unfortunately for Matthew, Georgia Tech cared little for his liberal arts background, and required him to take some science classes at a local community college before they would admit him. While at Georgia Perimeter College (then DeKalb College) Matthew uncovered in himself a deep love of mathematics, and quickly changed his major. Finally allowed into Georgia Tech, Matthew excitedly went to his orientation where he was accidentally taken to the Physics building, and not the Math building. After trying physics on for size, he finally decided that physics was the subject for him and again changed his major. A couple of years later Matthew emerged with his B.S. in physics in 2000. But Matthew had not had enough of Georgia Tech, and decided to stay for his graduate studies, where he obtained his Ph.D. in 2006.